AFRL-RY-WP-TR-2012-0210

RF METAMATERIALS FOR FOLIAGE PENETRATION (FOPEN) APPLICATION

Nelson Poon

Lockheed Martin Corporation

FEBRUARY 2013
Final Report

AIR FORCE RESEARCH LABORATORY
SENSORS DIRECTORATE
WRIGHT-PATTERSON AIR FORCE BASE, OH 45433-7320
AIR FORCE MATERIEL COMMAND
UNITED STATES AIR FORCE

NOTICE AND SIGNATURE PAGE

Using Government drawings, specifications, or other data included in this document for any purpose other than Government procurement does not in any way obligate the U.S. Government. The fact that the Government formulated or supplied the drawings, specifications, or other data does not license the holder or any other person or corporation; or convey any rights or permission to manufacture, use, or sell any patented invention that may relate to them.

This report was cleared for public release by the USAF 88th Air Base Wing (88 ABW) Public Affairs Office (PAO) and is available to the general public, including foreign nationals. Copies may be obtained from the Defense Technical Information Center (DTIC) (http://www.dtic.mil).

AFRL-RY-WP-TR-2012-0210 HAS BEEN REVIEWED AND IS APPROVED FOR PUBLICATION IN ACCORDANCE WITH THE ASSIGNED DISTRIBUTION STATEMENT.

*//Signature//

REY REBO, Program Manager
Materials Branch
Aerospace Components Division

//Signature//

BRADLEY CHRISTIANSEN, Lt Col, USAF
Deputy Division Chief
Aerospace Components Division
Sensors Directorate

This report is published in the interest of scientific and technical information exchange, and its publication does not constitute the Government's approval or disapproval of its ideas or findings.

*Disseminated copies will show "//signature//" stamped or typed above the signature blocks.

REPORT DOCUMENTATION PAGE

Form Approved
OMB No. 0704-0188

1. REPORT DATE *(DD-MM-YY)*	2. REPORT TYPE	3. DATES COVERED *(From - To)*
February 2013	Final	01 September 2009 – 29 March 2012

4. TITLE AND SUBTITLE
RF METAMATERIALS FOR FOLIAGE PENETRATION (FOPEN) APPLICATION

5a. CONTRACT NUMBER
FA8650-09-C-1656

5b. GRANT NUMBER

5c. PROGRAM ELEMENT NUMBER
62204F

6. AUTHOR(S)
Nelson Poon (Lockheed Martin Corporation)

5d. PROJECT NUMBER
2002

5e. TASK NUMBER
11

5f. WORK UNIT NUMBER
Y050

7. PERFORMING ORGANIZATION NAME(S) AND ADDRESS(ES)

Lockheed Martin Corporation
1011 Lockheed Way
Palmdale, CA 93599

The Ohio State University
Department of Electrical and Computer Engineering
Columbus, OH 43210

8. PERFORMING ORGANIZATION REPORT NUMBER

9. SPONSORING/MONITORING AGENCY NAME(S) AND ADDRESS(ES)

Air Force Research Laboratory
Sensors Directorate
Wright-Patterson Air Force Base, OH 45433-7320
Air Force Materiel Command
United States Air Force

10. SPONSORING/MONITORING AGENCY ACRONYM(S)
AFRL/RYDM

11. SPONSORING/MONITORING AGENCY REPORT NUMBER(S)
AFRL-RY-WP-TR-2012-0210

12. DISTRIBUTION/AVAILABILITY STATEMENT
Approved for public release; distribution unlimited.

13. SUPPLEMENTARY NOTES
PAO Case Number: 88ABW-2012-4704, cleared 31 August 2012. Report contains color.

14. ABSTRACT

Foliage Penetration (FOPEN) radars are critical for detecting and identifying targets concealed by trees and forests. Typically, FOPEN transmits at high powers, making them difficult to design and operate at low frequencies where mismatches are possible. Low operating frequencies also result in large apertures that limit FOPEN systems to large platforms. Novel metamaterials have the potential to reduce the size of FOPEN antennas, but two persistent challenges remain. First, high transmit power requires a low-loss metamaterial solution. Second, the wide bandwidth required by FOPEN systems makes resonant metamaterials solutions unworkable. To shrink the volume of state-of-the-art FOPEN antennas and create a new capability for volume-limited aircraft, Lockheed Martin (LM) Corporation, in conjunction with the Ohio State University (OSU), proposes to develop a novel, metamaterial FOPEN antenna. Shadow Harvest, currently a USAF/ACC JCTD, is a sensor pod and roll-on/roll-off analyst module that adds ISR capability to any C-130 in the USAF fleet within 24 hours.

15. SUBJECT TERMS
antenna array, beam steering, foliage penetration, low frequency, UHF antenna

16. SECURITY CLASSIFICATION OF:			17. LIMITATION OF ABSTRACT:	18. NUMBER OF PAGES	19a. NAME OF RESPONSIBLE PERSON (Monitor)
a. REPORT	b. ABSTRACT	c. THIS PAGE			Rey Febo
Unclassified	Unclassified	Unclassified	SAR	76	19b. TELEPHONE NUMBER *(Include Area Code)* N/A

Standard Form 298 (Rev. 8-98)
Prescribed by ANSI Std. Z39-18

TABLE OF CONTENTS

Section **Page**

LIST OF FIGURES

Figure **Page**

LIST OF FIGURES

Figure **Page**

LIST OF FIGURES

LIST OF TABLES

FOREWORD

The Lockheed Martin Aeronautics Company (LMA) Advanced Development Program (the "Skunk Works") in Palmdale, Ca, in collaboration with Ohio State University (OSU) Department of Electrical and Computer Engineering, is developing a Tightly Coupled (TC), Metamaterial array (Meta-array) for AFRL, RF Metamaterials for foliage penetration (FOPEN) application.

FOPEN radar is a powerful tool for surveillance and reconnaissance missions, but the UHF and VHF frequency operation require a larger antenna aperture. Reducing the aperture size would permit inclusion on a wider verity of air vehicles while reducing the associated size and weight penalties.

This program is to design a metamaterial FOPEN antenna offering equivalent RF performances. This development effort is not for a new metamaterial technology. It is a fine tuning of "existing metamaterial technology" for FOPEN application.

The objective is developing a compact and lightweight meta-array allows capability to be integrated into small UASs and other size-constrained platforms for FOPEN SAR Radar aperture. This development will demonstrate the ability of metamaterials to enhance or enable antenna performance beyond current State-of-the-Art (SOA) antenna.

AFRL, RF Metamaterials for FOPEN is a three-phase effort with objectives defined and described below,

1. Phase I is a nine month theoretical simulation and prediction effort (September 2009 to May 2010) to demonstrate the metamaterial FOPEN antenna will offer equivalent pattern (gain, beam width, sidelobes, cross-polarization) and VSWR bandwidth to a SOA antenna with 2x reduction in aperture size.

2. Phase II is a one year laboratory-scale prototype effort (May 2010 to April 2011) for fabrication and testing with performances compared to the prediction in Phase I.

3. Phase III is a one year integrate, fabricate and test effort (July 20011 to June 2012) of Phase II developed FOPEN meta-array onto LMA C130 Shadow Harvest sensor pod. The measurement performances compared to the prototype developed in Phase II.

PREFACE

Metamaterial antennas are a class of antenna which use metamaterial to increase performance of miniaturized (electrically small) antenna system. Their purpose, as with any electromagnetic antenna, is to launch energy into free space. However, these incorporate metamaterials, which are materials engineered with novel, often microscopic, structures to produce unusual physical properties. Antenna designs incorporating metamaterials can step-up the radiated power of an antenna. Novel components such as compact resonators and metamaterial loaded waveguides offer the possibility of previously unavailable applications.

With conventional antennas that are very small compared to the wavelength, most of the signal is reflected back to the source. The metamaterial, on the other hand, makes the antenna behave as if it were much larger than it really is, because the novel antenna structure stores energy, and re-radiates it.

These novel antennas appear to be useful for wireless systems that continue to decrease in size, such as emergency communications devices, micro-sensors and portable ground-penetration radars to search for tunnels, caverns and other geophysical features.

Foliage Penetration SAR Collection System was developed in late-1960 to mid-1970 time frame. Two important system realities affected the growth of the FOPEN technology: (1) foliage attenuation limited the system to short-to-medium-range operation; and (2) manned aircraft could not be adequately protected at these ranges. Remotely piloted vehicles (RPV; also known as unmanned air system, or UAS, in today's vocabulary) were just starting to be developed.

By the late 1980s, the image collection community had determined that SAR could provide acceptable and useful detection and characterization of forested regions. These SAR systems required small antennas and modest power; which was acceptable for experiments and might be possible on RPV installation. In 1988, the NASA jet Propulsion Laboratory started the AIR-SAR program and flew a multiple-frequency SAR platform until 2004.

Airborne ground-moving target indication (GMTI) FOPEN Radar system was significantly more difficult to implement, especially on airborne moving platform. The size of the antenna for both detection and localization of the moving targets prohibited installation on a fixed-wing aircraft. X-band SOTAS development verified the benefit of stationary rotary wing operation for GMTI radar. But the size of the antenna at UHF and the lack of unmanned helicopter would not give rise to airborne FOPEN GMTI radar for more than 2 decades, when the FOPN reconnaissance, surveillance, tracking, and engagement Radar (FORESTER) system would not be developed for the remotely piloted A-160 Hummingbird.

With the advances in critical Radar technologies of wideband waveform generation and digital image formation, the community could start the task of understanding the capabilities and limitation of FOPEN SAR. SAR system was just starting to gain acceptance in the surveillance community, which had relied on high-resolution optical pictures for decades.

Every new FOPEN Radar system developed need to answer the question of "why VHF or UHF?" This question is easy to answer. Optical photographs and microwave Radar cannot reliably detect man-made objects that been in the dense forest cover. Two emerging technologies were being developed that could reduce the unreliable detection of targets under foliage. The first technology was UWB wave forms that could enable high-resolution SAR images at both VHF and UHF frequencies. The second technology was use of polarization of the Radar signal in the FOPEN SAR process.

High-resolution imagery serves two purposes: (1) provide a better separation of the object scattering from the background clutter; and (2) provide more detail of scattering of objects for characterization. In applications for the foliage or terrain characterization, this factor is not as strong a motivation. However, to find a small vehicle or a buried land mine, image resolution is a major consideration. Polarization diversity has been evolving as a significant capability for both target detection and characterization of terrain and man-made objects. If characterization is an important system objectives, then polarization must be factored into system waveform and processing approach from start.

FOPEN meta-array developed for AFRL, RF metamaterials program will provide the critical, acceptable and useful detection and characterization to UHF FOPEN operation. One biggest advantage to this development is achieving very small antenna aperture size in comparing with wave length. It will help for both detection and localization of moving targets installation on fixed-wing aircraft, ultra wide bandwidth, foliage attenuation, polarization diversity, attenuation and high-resolution.

1. SUMMARY

Phase I, AFRL, RF Metamaterials, FOPEN Applications program has successfully completed in May, 2010. The numerical model and simulation proves TC dipole FOPEN array meets the Classical Metamaterial Equivalent Circuit definition. The predicted RF performances (Paragraph 3.1) offer equivalent pattern (gain, beam width, sidelobes, cross-polarization) and VSWR bandwidth to a SOA antenna with 2x reduction in aperture size (24"x24"x6" height). The comparison of FOPEN meta-array aperture size (Fig. 8) to other antenna elements is shown in Table 1,

Table 1 – Compare FOPEN Meta-Array to Other Antenna Elements

Element Type	Diameter @ 200MHz	Height @ 200MHz
Archimedean Spiral	30.0" ($\lambda_L/2$)	30.0" ($\lambda_L/2$)
Equiangular Spiral	30.0" ($\lambda_L/2$)	30.0" ($\lambda_L/2$)
Sinuous	24.0" (2 $\lambda_L/5$)	24.0" (2 $\lambda_L/5$)
Vivaldi (ε = 7.0)	27.2"(1.2 $\lambda_L/\varepsilon^{1/2}$)	45.4" (1.2 $\lambda_L/\varepsilon^{1/2}$)
DARPA - FORESTER	36.0"	46.0"
SOA Antenna	27.1"	12.0"
LMA/OSU TC Dipole Array	24.0" (8x8 Array)	6.0" (Maximum)

LMCSS has also developed the FOPEN system requirements by extracting the knowledge learned from LM TRACER program. The current and future FOPEN requirements are summarized in Table 2.

Paragraph 3.2 shows the simulation processes. The predicted VSWR (< 2.5:1) is ultra board band (UWB) in the frequencies from 180-1000MHz. The predicted radiating efficiency over the frequencies (250-900MHz) is higher than 80%. The predicted realized gain is about 5-12 dBi.

Phase II is completed in June, 2011. Four laboratory-scale prototypes are developed with egg-crate construction for the purposes of cost, structural integrity and thermal heat dissipation in high power operating environments. LMA applied concurring engineering, the best value approach and the knowledge learned from LM TRACER program to develop those prototypes.

Fig. 29 is an OSU prototype (#1, 7x7 array) fabricated and tested inside the ESL compact range. Fig. 31 shows the LMA prototypes (#2, #3 and #4, 8x8 array) fabricated and tested at LM Rye Canyon Measurement Facility (Fig. 31). The results show the FOPEN meta-array is low cost, compact and lightweight with RF performances meet and exceed the FOPEN requirements. The RF performances cover equivalent pattern (gain, beam width, sidelobes, and cross-polarization) in a wider bandwidth. The FOPEN meta-array has higher RF performances better than the LM TRACER antenna.

Phase III is completed in April, 2012. The prototype #4 developed in Phase II is integrated onto a C130 Shadow Harvest sensor pod replica as shown in Fig. 1,

Figure 1 -FOPEN Meta-Array Integrated Assembly

The measured RF performances show the integrated meta-array meets and exceeds the current and future FOPEN requirements in Table 2.

The measured VSWR in Fig. 2 shows the FOPEN meta-array design is UBW (170-1000 MHz). The measured VSWR on the integrated assembly is shown below,

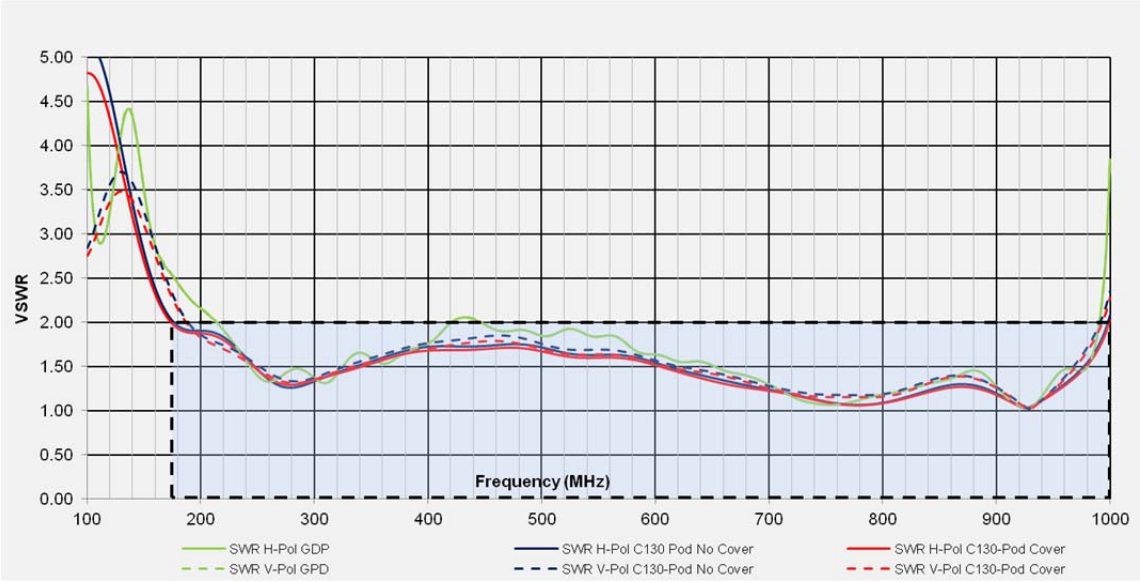

Figure 2 - Measured VSWR

The measured radiation patterns in both polarizations (V-V and H-H) are closely matching to the prediction. The results are summarized in Fig. 3 and Fig. 4.

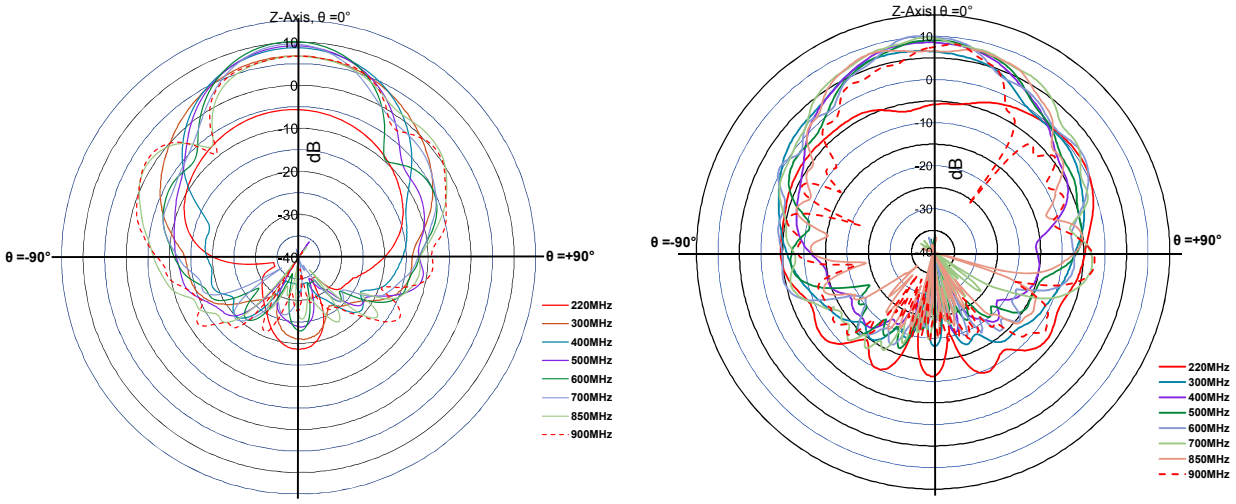

Measured Radiation Patterns (V-pol) Measured Radiation Patterns (H-pol)

Figure 3 -Measured Radiation Patterns On C-130 Sensor Pod Replica

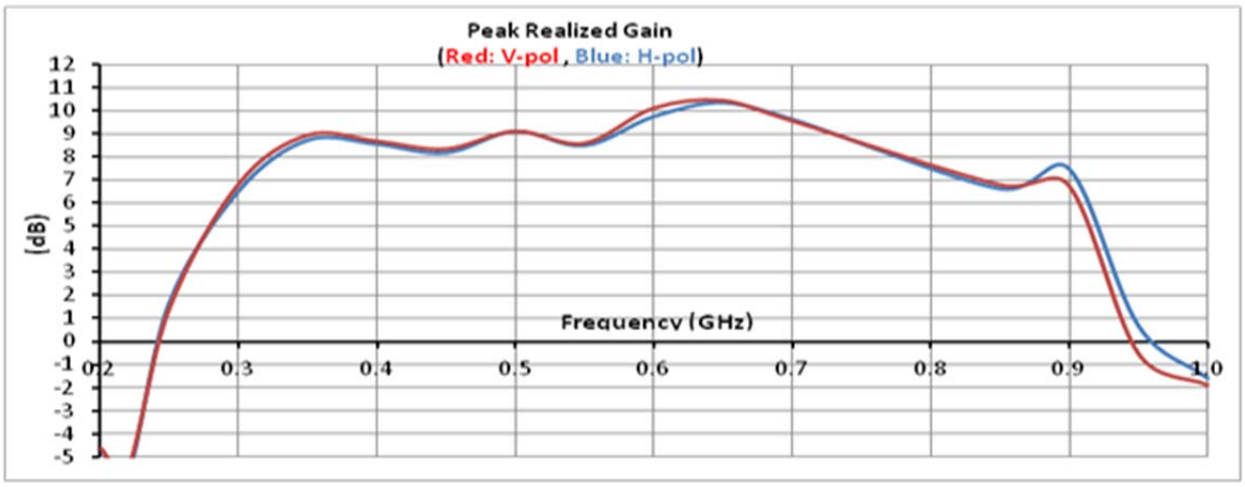

Figure 4 -Realized Peak Gain On C-130 Sensor Pod Replica

The measured beam steering patterns indicates the integrated Meta-array is capable of very wide angle beam scanning by applying proper phase distribution to the centre four rows of active ports (32 elements).

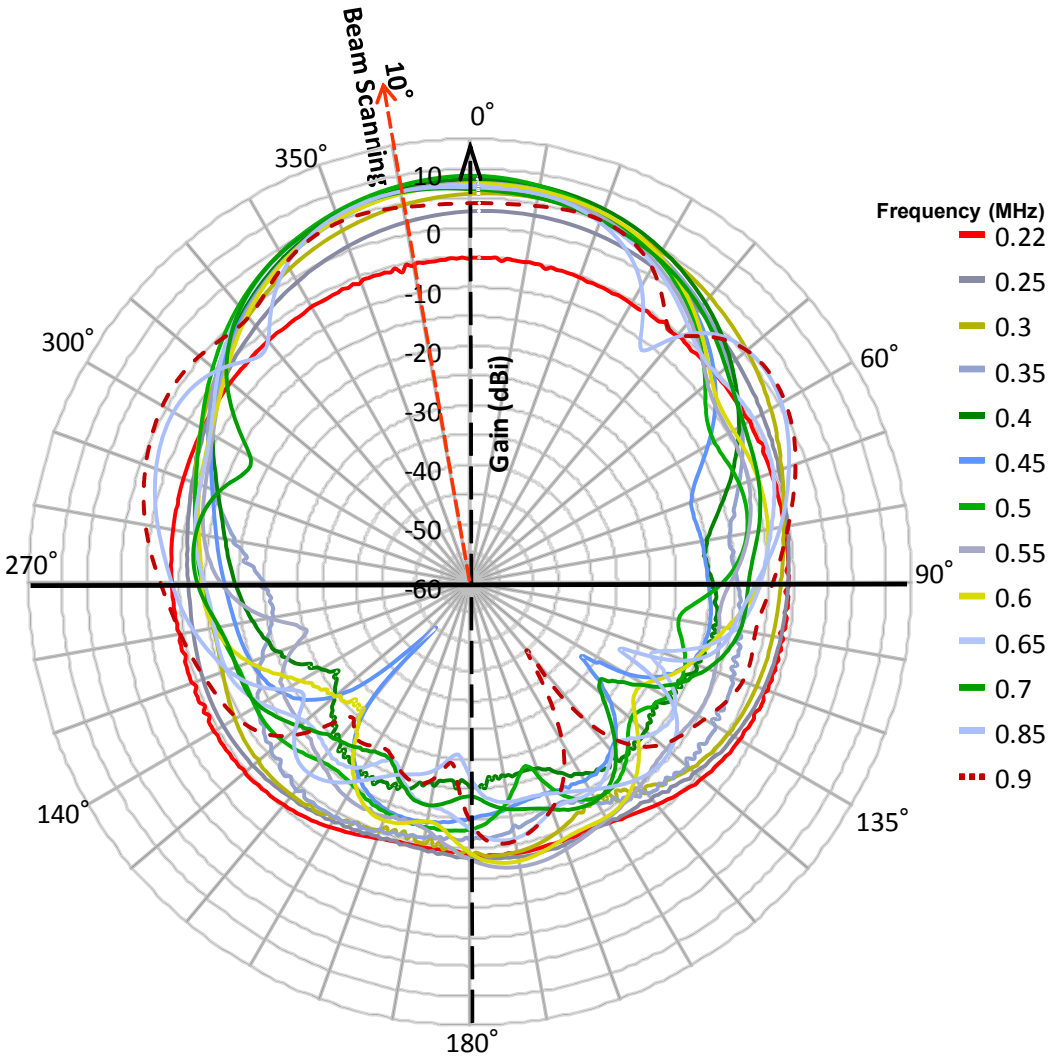

Figure 5 -Simulated Dual Pol. 8x8 Array in 0º and 10º Beam Scanning

No power break-down at pulse width (70µsec), PRF (5 kHz) and peak power (1kw), equivalent to duty-cycle 35% (~350cw). The FOPEN meta-array should be able to meet higher than average power 350cw. This power level was stopped due to the limitation of the maximum divider's average power rating (320cw).

LMA/OSU has successfully completed the AFRL, RF Metamaterials for FOPEN Application program. The developed integrated FOPEN meta-array meets and exceeds the current/future FOPEN requirements.

2. INTRODUCTION

In this program, Lockheed Martin Aeronautics Company (LMA), in collaboration with Ohio State University (OSU) team, is leveraging the TRACER FOPEN experience and the existing metamaterial technology to enhance the performances to current and future UHF FOPEN aperture design.

The objective is utilizing metamaterials to improve RF abilities in bandwidth, physical size and manufacturing cost, and improving SAR image resolution and propagation effects into foliage at the same time.

Metamaterials are typically constructed in periodic arrangements of commonly available materials (isotropic or anisotropic dielectrics, magnetic materials, conductors, etc.) and exhibit electromagnetic properties not found in natural materials. A metamaterial constructed structure can slow the wave velocity to achieve electrically smaller RF structures [12], [13], [14], [25], [26], [27], [28].

Mode diversity and higher order dispersion (K-ω) curves of periodically layered (and possibly ferromagnetic) materials have recently been proposed for high gain and miniature antenna applications [29], [30], [31]. These material arrangements result in an effective anisotropic medium.

Volumetric DBE in Fig. 6 provides a depiction of the crystal operation and its composition [29], [31]. Specifically, in contrast to the 2^{nd} order relation at the regular band edges (RBEs) of EBGs, the K-ω curve behavior of the DBE mode follows a 4^{th} order polynomial relation. Likewise, MPCs can exhibit spectral asymmetry, i.e. $\omega(K) \neq \omega(-K)$; and support 3^{rd} order stationary inflection points (SIPs) within their propagation bands[34]. Volumetric layered media exhibits higher order K-ω behaviors providing stronger slow-wave resonances to be harnessed for designing conformal high gain antennas [29], [31].

Recently, it was found that the dispersion relations exhibited by the volumetric DBE can also be realized using traditional microwave substrates (printed coupled lines) depicted in Fig. 7 [35], [36]. This practical realization provides for new design flexibility to enable miniaturization, higher gain, and higher bandwidth [37].

In this program, LMA and OSU are particularly focusing on such media referred to as degenerate band edge (DBE) [32] that split the conventional K-ω curves of otherwise isotropic EBG structures into two branches. Mode coupling between K–ω branches generates novel slow group velocity modes to be harnessed by directive and small antennas.

Layered periodic medium in Fig. 6 is consist of anisotropic crystal with property of suppressing reflections at the interface, while concurrently causing significant wave slow down in the transmitted field leading to significant field increase.

Fig. 7 is the low cost printed microstrip structures which realize the volumetric anisotropy in equivalent dual-transmission line circuits.

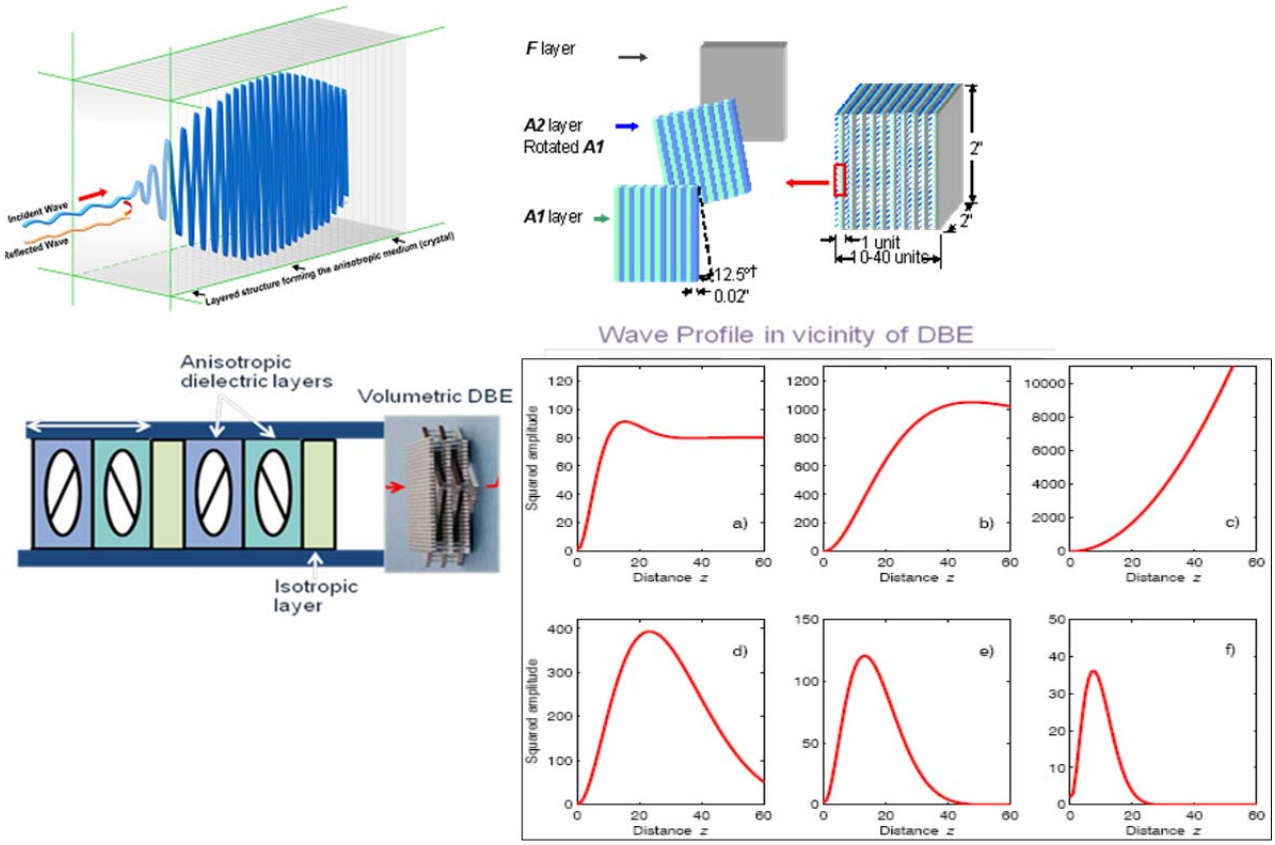

Figure 6 -Layered Periodic Medium Consisting of Volumetric Anisotropic Crystal

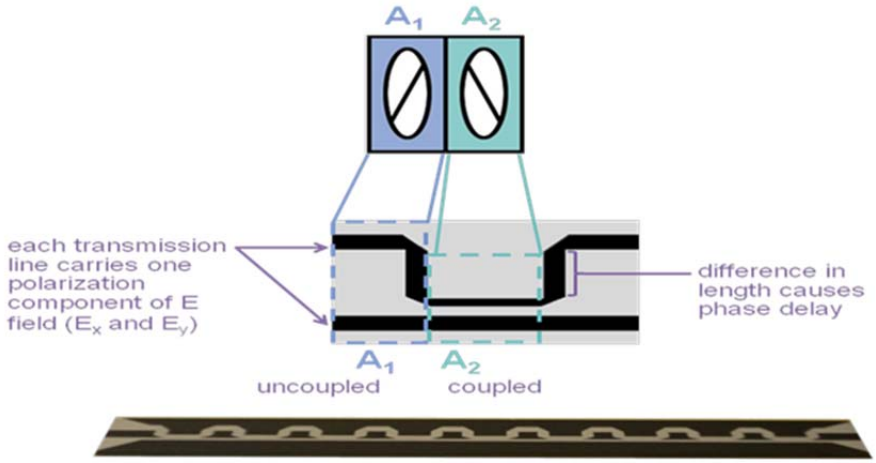

Figure 7 -Realization of Anisotropy EBG Structure

Munk demonstrated that the UWB arrays can be synthesized from narrowband dipole elements provided inter-element coupling is controlled concomitantly with the ground plane distance. Specifically, Munk showed that by enhancing the capacitive coupling between adjacent dipoles, by introducing for capacitors which could cancel out the ground plane inductance and reach a bandwidth of 4.5:1 with a conformal aperture. Munk introduced Current Sheet Antenna (CSA) with simple equivalent circuits that model the impedance of infinite arrays at low frequencies.

However, no design guidelines for choosing the excitations (amplitude and phase) and the characteristic impedances of the feeding lines or the resistive terminations of each element in the finite array.

Fig. 8 shows the relationship between DBE dual-transmission line circuits, capacitive coupled region, and equivalent circuit described in classical metamaterial TL. The challenge is addressing the metamaterial TC antenna elements and the over-all results which exhibits significant wave slow-down.

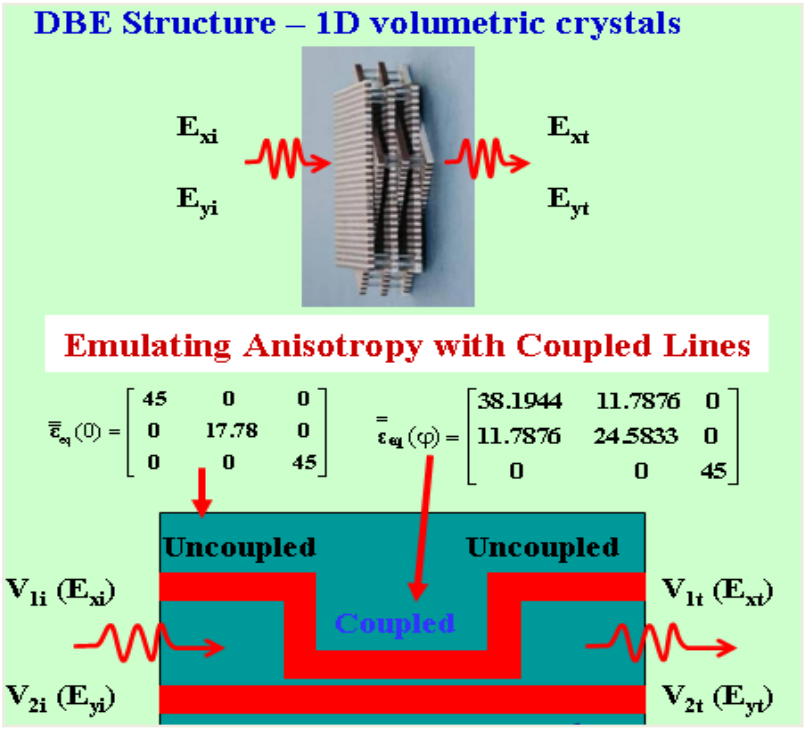

Figure 8 -DBE Transformation

UHF FOPEN SAR Radar operates on 230 to 445 MHz with image resolution is about 0.7 to 1.0 meter. The antenna gain is reduced as propagated through the foliage. SAR radar performance is affected by attenuation, backscatter, phase variation and depolarization described below,

a. **Attenuation:** Foliage attenuation increases significantly with frequency. Two-way HH polarization signal attenuation for a 30 depression angle increases from 5.5 dB at UHF to 17.0 dB at L band and to 33.6 dB at C band.
b. **Backscatter:** Foliage backscatter distributes component arising from reflections and interactions between individual leaves, branches, tree trunks and ground-bounce returns. As frequency increases, target return signals diminish until they are overwhelmed by foliage clutter, and target detection becomes impossible.
c. **Phase variation**: SAR requires coherent measurements of phase across the viewing aperture. Phase variation leads to spatially variant blurring and defocusing of the formed image.
d. **Depolarization:** Operate one polarization at a time (V or H). Receiving reflected pulses with sufficiently high pulse repetition frequencies.

Infinite Arrays - Arrays in Free Space - Wheeler's theory

Infinite Current Sheet Antenna (see Fig. 9(a)) was first introduced and studied by Wheeler back in the 1950s [38], [39]. His premise was that for a uniform current ***J*** on an infinitely large aperture, radiation occurs at all frequencies and bi-directionally (towards $+z$ and $-z$ directions). As depicted in Fig. 9(b), a practical way to implement such a structure is to arrange infinitely long wires on a plane and feed them periodically. Alternatively, one can consider straight, center-fed wire dipoles, connected at their tips. The unit cell of this "discrete" current sheet is a rectangular area (d×d) that contains a simple dipole and can be represented by an equivalent TL circuit, as depicted in Fig. 9(c). As such, the circuit consists of a source connected to two semi-infinite TLs, each having a characteristic impedance of $Z_0 = 120\pi = 377\Omega$. The top and bottom TLs represent, respectively, radiation toward the top and bottom half-spaces formed by the array plane. Thus, the total impedance seen at the source terminals is $Z_0/2 = 188\Omega$.

Although Wheeler's concept predicts a purely resistive input impedance of $Z_0 = 188\Omega$, its "discrete" representation with interconnected dipoles (as shown in Fig. 9(b)) deviates from this ideal situation when the feed separation becomes $d > \lambda/4$. The reason for this deterioration is that as the dipoles approach their resonance, the current distribution becomes non-uniform (approx. sinusoidal) and therefore their impedance starts to deviate from that of the ideal case. Nonetheless, by employing a self-complementary aperture, using for example bowtie elements, one can recover a constant, purely resistive impedance of 188Ω throughout the whole frequency band, as illustrated in Fig. 10. Evidently, grating lobes will appear when the feed spacing is $d > \lambda/2$. Notice that starting from an infinite, interconnected dipole array (i.e. 0^o flare angle) and gradually increasing the flare angle of the arms to 90^o would turn the dipoles into bowties. For the bow-tie elements, the impedance becomes purely real (188 + j0 Ω) throughout the whole frequency band. Thus, in free space, an infinite array of straight, connected dipoles can deliver unlimited low frequency bandwidth. On the other hand, the high frequency limit is constrained by the appearance of grating lobes at frequencies $f > c/2d$ for endfire radiation or at $f > c/d$ for broadside radiation, where d is the feed separation (in other words, element size) and c is the speed of light. However, when the array is placed conformably on a ground plane the bandwidth is dramatically reduced on both high and low ends

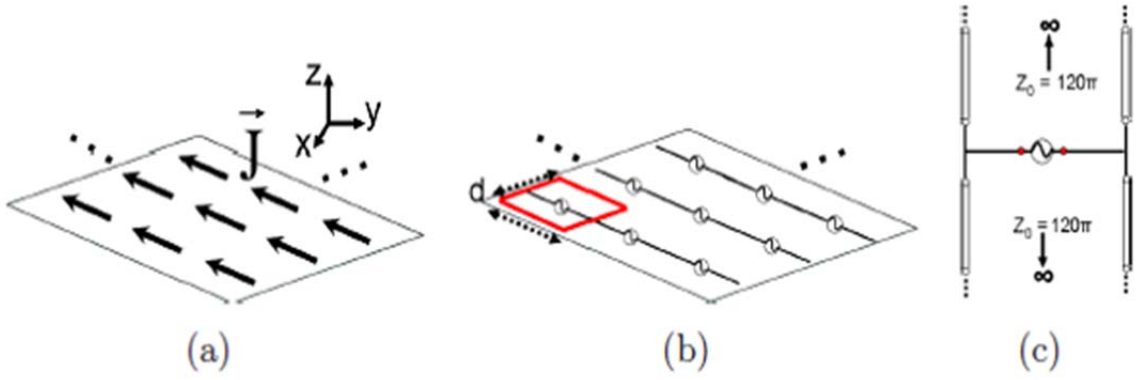

Figure 9 -(a) Wheeler's infinite current sheet; (b) Practical implementation of a current sheet with periodically fed, infinite wires; (c) Equivalent circuit model of an infinite array of interconnected dipoles in free space

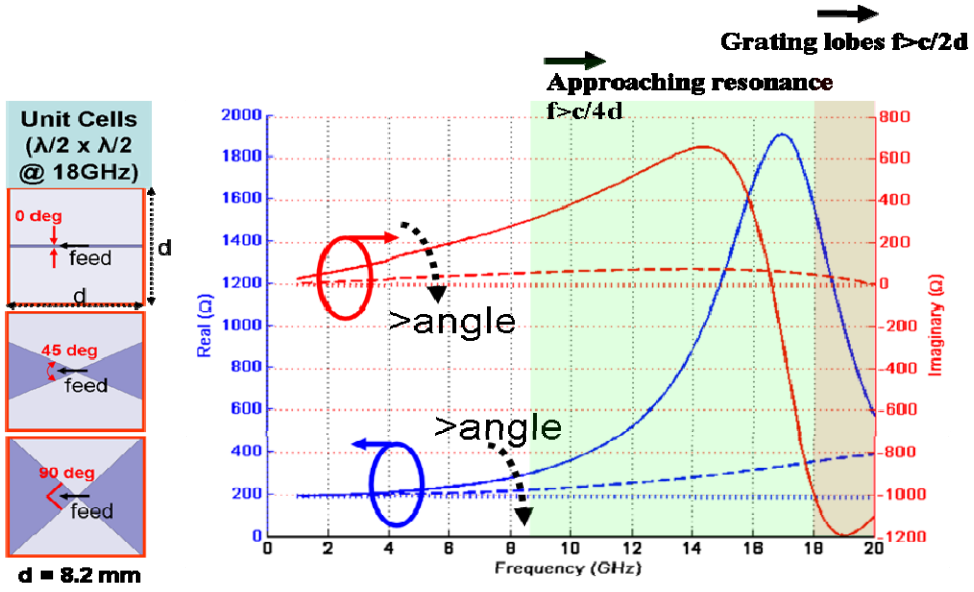

Figure 10 -Bowties - Free space impedance of an infinite dipole array and flaring out the angle from 0º-90°

Conformal Metamaterial Arrays - Munk's Theory

As mentioned above, the idealness of Wheeler's concept in free space is lost when the array is placed conformably on a ground plane (GP). As an example, Fig. 9(a) (top) shows an infinite dipole array placed conformably, at height h = 8.2mm (= d, unit cell size) over an infinite perfect electric conductor (PEC) GP. In conformal installations, there are two primary reasons for the low-frequency impedance mismatches: **1)** very low (~ 0 Ω) radiation resistance, as the array approaches the GP (compared with R = 188Ω in free space,) and **2)** an increase in the inductance proportionally to $j\eta\tan(2\pi h/\lambda)$ (compared to X = 0 in free space case). Here, η is the intrinsic impedance of free space (377Ω) and λ is the wavelength. This detrimental effect of the ground plane shorting is depicted below in Fig. 9(b). -(a) Schematic representation of an infinite, capacitive coupled dipole array over a ground plane; (b) Equivalent circuit for modelling the infinite array impedance at low frequencies; (c) Metamaterial perspective of the array in (a)

In order to circumvent the performance degradation due to ground plane inductance, Munk [40] inserted interdigital capacitors at the tips of the dipoles (see Fig. 11(a) bottom). These capacitors connected in series with the dipoles cancelled the inductance of the ground plane at low frequencies. The corresponding VSWR bandwidth of the dipole arrays in free space and over the GP (with and without capacitors), are shown in Fig. 11(c). As seen, Munk's CSA antenna achieves ~ 4.5:1 (VSWR< 2) bandwidth due to the cancellation of the GP inductance with series capacitors between the array elements. However, evident from Fig 11(b), this technique does not significantly enhance the radiation resistance of the array.

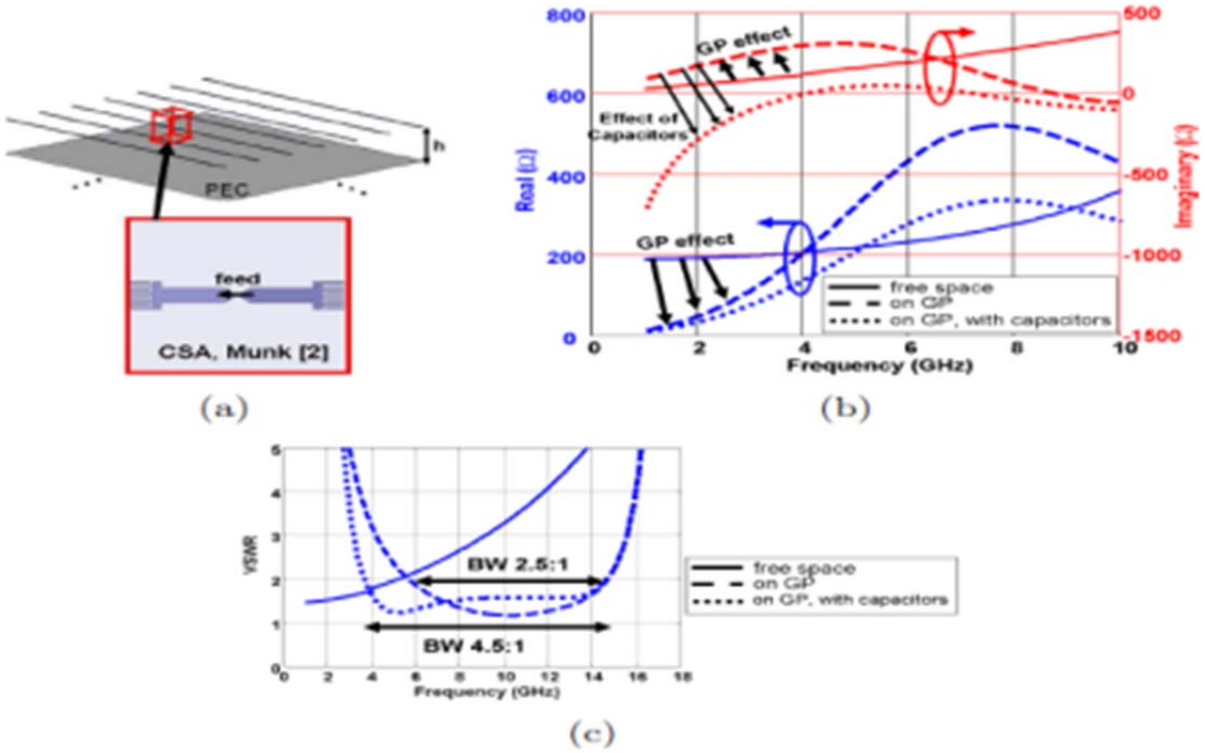

Figure 11 -Conformal Metamaterial Arrays

To provide more physical insight on how the CSA antenna works, Munk also constructed the equivalent circuit model of the unit cell of the infinite array shown in Fig. 12(a) which is depicted in Fig. 12(b). Here, R_{A0} and X_A are the radiation resistance and reactance of the array in free-space, respectively. Subsequently, the ground plane is modeled as a short circuit, at distance h from the array plane. As a result, the ground plane exhibits an inductive impedance Z_{1+} = j$2R_{A0}$tan $(2\pi h/\lambda)$. We also note that X_A is dominated by the mutual coupling between adjacent elements.

Thus, the basic mechanism of operation for the CSA is the following: The impedance seen at the terminals of each element is found as a parallel combination of impedances looking up and down from the array plane, viz. $Z_{1+}//Z_{1-}$ + jX_A, where $Z_{1-} = 2R_{A0}$ and Z_{1+} is the impedance of a short-circuited Transmission Line (TL) of length l. At low frequencies ($<\lambda/4$) that impedance $Z_{1+}//Z_{1-}$ becomes inductive due to the GP. And therefore a capacitive reactance is needed for cancellation. This negative reactance is provided by the interdigital capacitors, shown in Fig. 12(c), through X_A. As such, the antenna feeds see mostly resistive impedance leading to a 4:1 bandwidth.

At this point, it is imperative to note that the introduction of series capacitors for coupling the array elements as well as the presence of the shunt, ground plane inductance in the CSA geometry bears striking resemblance to the negative index of refraction metamaterial elements. This aspect is further elucidated in Fig. 12(c) as well as in the following section below. In this circuit, the dipole inductance (due to the length of its arms) and the dipole-to-dipole mutual inductance from the neighboring dipoles are accounted for by the series inductor L_1. Likewise,

the self and dipole-to-dipole coupling (mutual) capacitance are represented by the series capacitor C_1. The inductance introduced by the GP (modeled in Fig. 12(b) as Z_{1+}) is taken into account by the parallel inductor $L_2 \approx \text{Im}\{Z_{1+}/\omega\}$. Also, any possible capacitance due to the GP (due to image currents) is represented by C_2. More importantly, and differently from the typical negative index TRL unit cells, the radiation resistance of each unit cell is modeled by resistor R while the dipole source is depicted to the right of the circuit. As such, this unit cell can be considered as a generalization of the ordinary NRI unit cells as it also incorporates the losses and possible active components within the periodic structure.

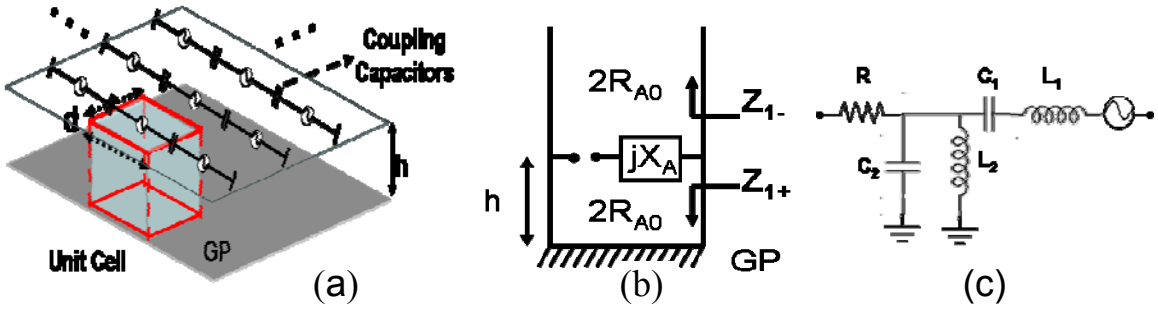

Figure 12 -(a) Schematic representation of an infinite, capacitive coupled dipole array over a ground plane; (b) Equivalent circuit for modeling the infinite array impedance at low frequencies; (c) Metamaterial perspective of the array in (a)

It is therefore straightforward to assert that the classic CSA can be classified as a metamaterial array. The circuit model of Fig. 12(c) can also be used to extract the dispersion (k-ω) diagram of propagating modes between the array plane and the GP, provided the radiation losses and excited sources are removed. On the other hand, the TL circuit model of Fig.12 (b) is useful in understanding the impedance behavior of the array when radiating modes are considered. Based on the above concepts, below we introduce new antenna elements that exhibit further wave slow down, hence allow for further miniaturization and improved low-frequency performance. We term these general antenna arrays as tightly-coupled dipole arrays (TCDAs) and illustrate their equivalence to typical metamaterial unit cells.

Equivalence of TCDAs with Coupled Metamaterial TLs

Equivalently, the overlapping dipole arrays both are periodic repetitions of a unit cell that consists of a coupled and an uncoupled DBE sections.

Fig. 13 depicts the equivalence of an "overlapping" dipole element as a unit cell in the coupled metamaterial TLs. A pair of "overlapping" dipole element is also a pair of coupled TCDAs, which can be used to model propagation through an anisotropic medium, such as a DBE TL. It behaves likes metamaterials DBE having significant wave slow-down results in wave amplitude-increase due to their unique dispersion characteristics.

TC dipole array concept has the equivalence of DBE TL array. It meets the definition of Classical Metamaterial Equivalent Circuit in Fig. 13. LMA/OSU uses the TC dipole meta-array to demonstrate the enhanced RF performance in FOPEN application.

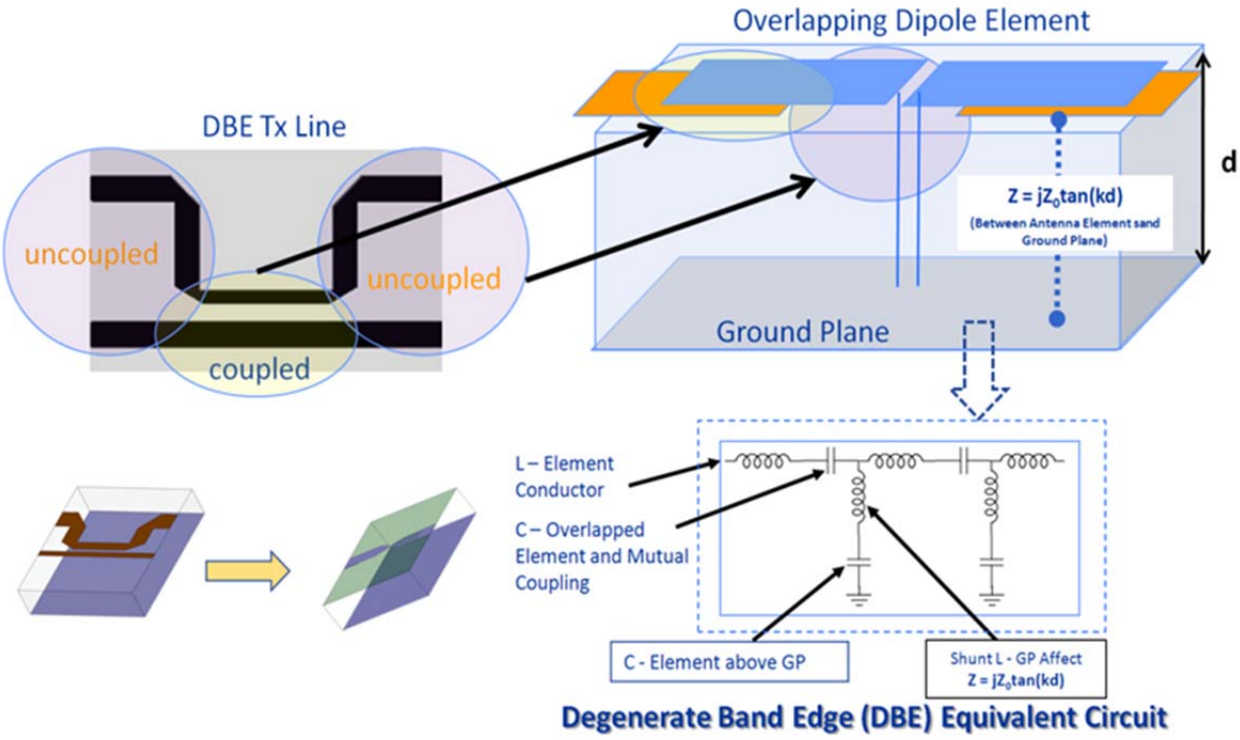

Figure 13 -Conceptual Equivalent of Metamaterial Coupled Lines Emulating Propagation in Anisotropic Media with Overlapping Dipole Array.

2.1 Subject

The subject of this report is applying the "existing metamaterial technology" to develop meta-array used for FOPEN application.

2.2 Purpose

The purpose is to demonstrate the metamaterials in TC DBE TL antenna will enhance or enable antenna performance beyond SOA antenna.

2.3 Scope

AFRL RF Metamaterials for FOPEN Applications program has three phases over a period of 36 months. The scope of this program is outlined in following,

4. Phase I is for theoretical simulation and prediction to demonstrate the metamaterial FOPEN antenna will offer equivalent pattern (gain, beam width, sidelobes, cross-polarization) and VSWR bandwidth to a SOA antenna with 2x reduction in aperture size.

5. Phase II is to develop a laboratory-scale prototype which will be fabricated and tested with performances compared to the prediction in Phase I.

6. Phase III is to integrate, fabricate and test of Phase II developed FOPEN meta-array onto LMA C130 Shadow Harvest sensor pod. The measurement performances compared to the prototype developed in Phase II.

2.4 Report Development

Paragraph 3 of this report is divided into three (3) distinguish sections. In each section outlines the development within each phase of the AFRL RF Metamaterials for FOPEN Applications program in the following,

Section I (Para. 3.1) is the report for Phase I to document the development of theoretical and analytical development.

Section II (Para. 3.2) is the report for Phase II to document the development of laboratory-scale prototype, testing and RF performance evaluation.

Section III (Para 3.3) is the report for Phase III to document the development of integration process, testing and overall RF performance evaluation.

2.5 Applicable Documents

The following documents are referenced herein and are applicable to the extent shown in Paragraph 6. All documents have been provided as part of this Final Report.

3. DEVELOPMENT

3.1 Phase I -Analytical Meta-array Development

3.1.1 Analytical methods, assumptions and procedures

Two main issues associated with the performance degradation of conformal arrays at low frequencies are the vanishing radiation resistance and the increased inductance coming from the ground plane. The latter can be compensated by introducing capacitive coupling between the elements, as shown in Fig. 13; however, this does not have a significant effect of the radiation resistance. One way to increase the radiation resistance is to increase the distance of the array to the GP. However, one should note that the ground inductance ($j\eta\tan(2\pi \boldsymbol{h}/\lambda)$) also increases proportionally. To counter the increased inductance we need even larger values of capacitance. We found that the interdigital capacitors (used in CSA) cannot provide enough capacitance with a reasonable number of fingers. Instead overlapping dipoles or interweaved dipoles were found to be more suitable for that purpose.

Unit cell of the "overlapping" dipole arrays is presented in below. Our initial designs are based on an infinite periodic structure to facilitate fast analysis using periodic boundary conditions (PBCs). At first glance, the overlapping dipole array is a simpler geometry and therefore easier to analyze and study. The coupling capacitance can be tuned very easily by simply changing the length, the width or the thickness of the overlapping section (see Fig. 14).

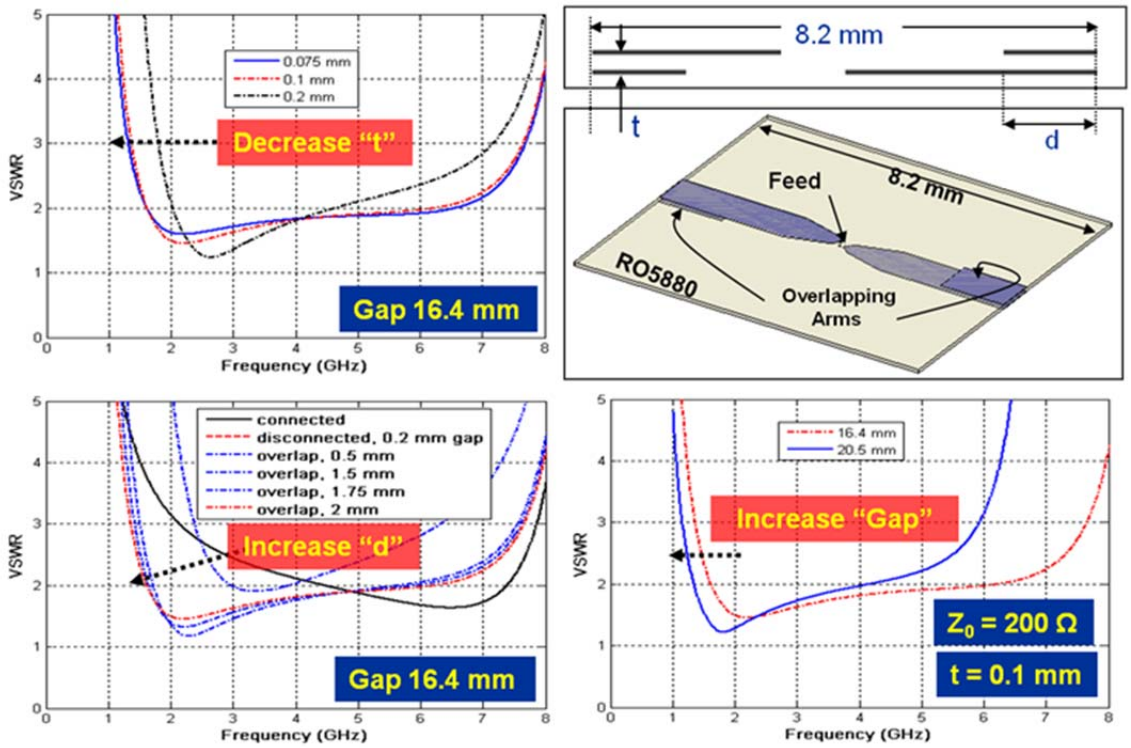

Figure 14 -Overlapping Dipole Array (Evaluation of VSWR Bandwidth as a Function of Ground Plane Distance, Thickness, and Overlapping Length)

Fig. 14 shows the overlapping dipole elements can achieve a bandwidth of ~3:1 (200 – 600 MHz). The unit cell dimensions are very small, λ/28 x λ/28, at the lowest frequency while the thickness of the array is λ/10, which corresponds to ~5.2'' at the FOPEN band. We also note that the overlapping dipoles can achieve ~20 times more capacitance than the interdigital capacitors of the CSA.

We note that the ultra wide band (UWB) antenna element described above, the overlapping dipoles, is balanced antennas presiding over a GP. Moreover, their extremely small size (~λ/28 at the lowest frequency) presents another significant challenge, that of the feeding network. Since typically 50Ω coaxial lines are used to feed each element of the array, it is imperative to have a UWB impedance transformer from 50Ω to 200Ω as well as a balun to feed each dipole element with a coaxial line. The pressing challenge here is the extremely limited real estate with an area of λ/28 x λ/28 under each array element. We address this challenge by the following UWB balun design.

3.1.2 VSWR Performance and Trade off

The UWB feed shown above is combined with the overlapping and interweaved dipole arrays. Initial calculations are carried out using the infinite array analysis via employing PBCs. Thus, each unit cell model contains a dipole element with its feeding network. Fig. 15 shows the performance of the overlapping and interweaved dipole arrays combined.

Next, we carried out trade studies regarding the GP height for both overlapping and interweaved dipole elements. Figure 10 compares the calculated VSWR for different heights from the ground plane. The general trend is that the closer we get to the ground plane, the higher the low frequency cut-off shifts. Note that as the distance from the ground plane was varied, the dipoles were kept the same and were not returned to obtain better matching.

With this baseline design at hand, we next consider the gain and aperture efficiency estimates for a final design assessment.

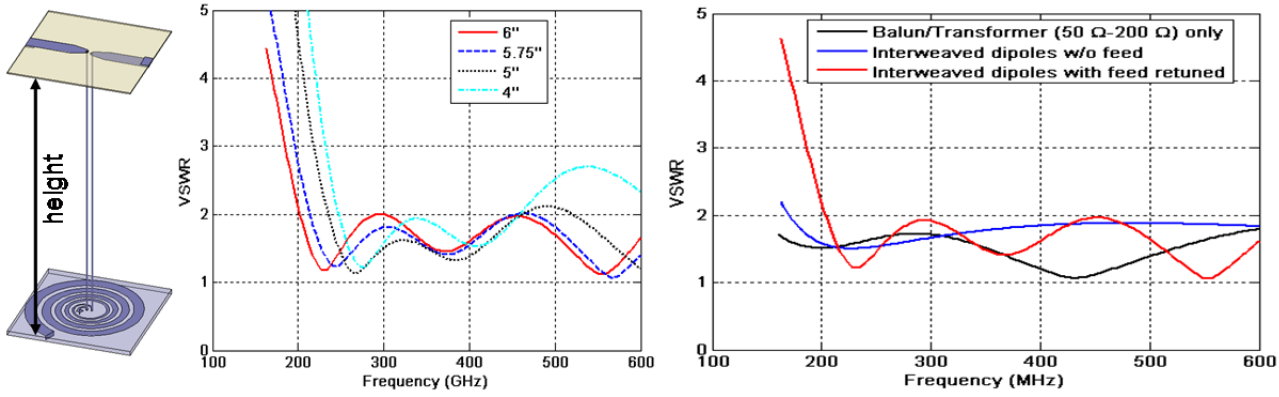

Figure 15 -Combined Impedance Transformer/Balun with Overlapping Dipoles

3.1.3 Estimating Directivity

A first order approximation is using the well known formula [42] for a uniformly excited rectangular aperture of area A, on an infinite PEC ground plane. By using equivalence principles and image theory, the equivalent magnetic current right at the opening and from that, the radiated fields and radiation intensity can be calculated. Then the average power density is computed using the fields at the aperture and then integrated over the physical bounds of the opening. The result for maximum directivity ($D_{max} = 4\pi A/\lambda^2$). This is plotted as a function of frequency in Fig. 16. The above formula underestimates maximum achievable directivity for small aperture sizes when $A < \lambda^2$. Instead, if the radiated power is obtained by integrating the radiation intensity over a half-sphere, one can obtain more reasonable results for small apertures. In fact, the new calculation predicts that when the aperture size becomes infinitesimal, the maximum directivity is exactly 3 (~5dBi) which is the anticipated directivity for an infinitesimal magnetic dipole on an infinite PEC ground plane. Using this new estimate for a 2' x 2' aperture, at 200 MHz we estimate a directivity of 5dBi.

However, this number is underestimating the real situation. The underlying assumption here is that the equivalent magnetic current was calculated from the E-fields that existed solely on the aperture opening and were zero everywhere else. In reality, the fields of a finite aperture extend well beyond the aperture's limits and thus the effective aperture is much larger than the physical. Thus the 5dBi directivity is underestimating the aperture's capabilities. Nevertheless, we use that number in conjunction with the calculated gain (-20 dBi) for a single unit cell (in an infinite aperture).

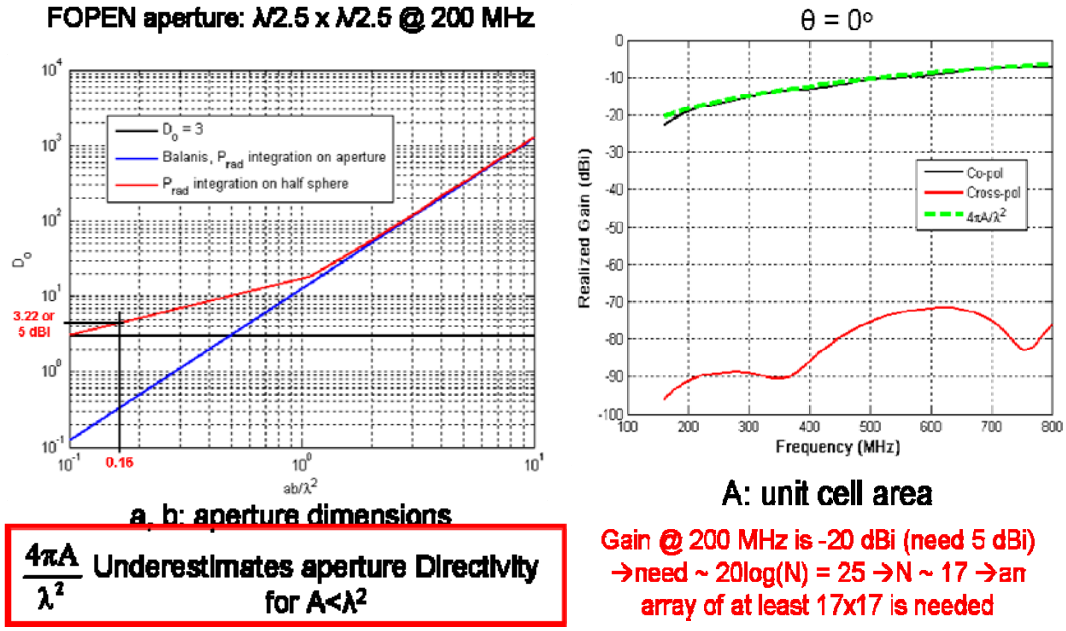

Figure 16 -Estimated Gain, "normal" Directivity and Number of Elements in a Finite Aperture

3.1.4 Analytical Approach to Finite Array Design

When considering tightly coupled arrays, the summary of contributions so far has as follows: Wheeler's Current Sheet in free space, which radiates well independent of frequency. His analysis focused more on studying the scanning properties of such an aperture. More recently, Munk proposed a practical implementation of such a sheet by using an array of dipole elements. He then demonstrated that one can partially overcome the ground's negative effects on the array bandwidth by capacitive coupling the elements, as was shown in Fig. 11.

However, to our knowledge, there is no design methodology for when it comes to realizing a finite array. This statement can be understood by a simple example. Consider the N x N array of tightly coupled elements (any type of elements) shown in Fig. 17. A ground plane, finite or infinite can also be considered behind the array. By using modern numerical techniques, such as domain decomposition methods [44] one can predict the impedance bandwidth, the gain and radiation patterns of a structure like that. However, those antenna parameters will strongly depend on the amplitudes (N^2), phases (N^2) and line or termination impedances (N^2) for each element in the array. Even with a given array shape, this equals to $3N^2$ unknowns. In other words, to evaluate the array's performance one would have to execute a significant number of computational runs and use complicated goal functions and algorithms in order to design the array.

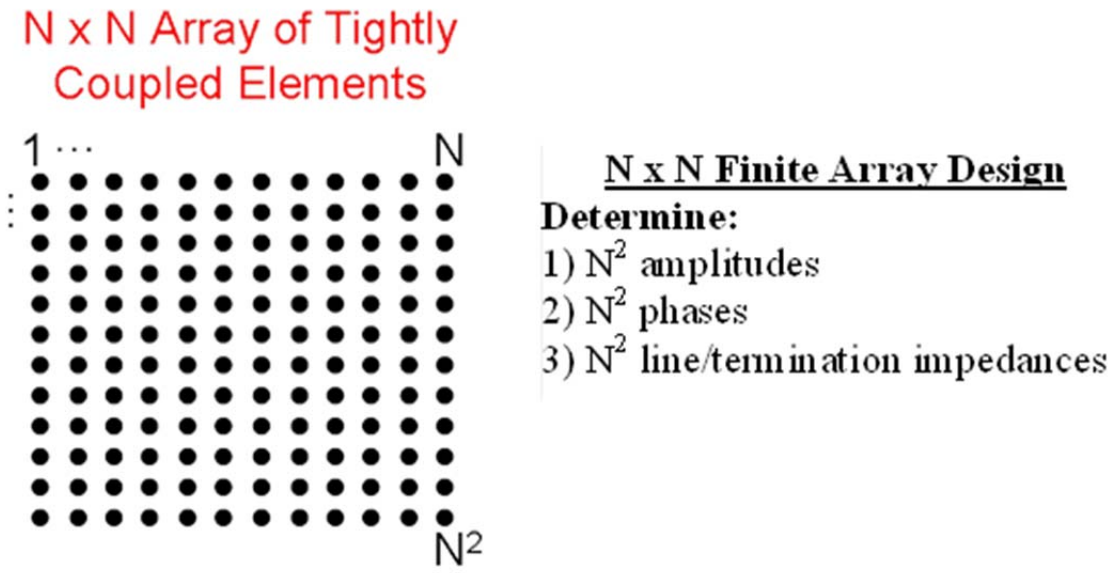

Figure 17 -Schematic Representation of an N x N Array of Tightly Coupled Elements.

However, a unique breakthrough technique is presented to easily work around the huge computational demands of a formal automated optimization based on the theory of characteristic modes [43]. Therefore, the analysis of TCDAs with characteristic mode theory comes naturally. In other words, the goal in the finite array design is to find the appropriate excitation profile, so that the distribution that the latter generates on the aperture of the antenna matches that of one its characteristic modes. The adoption of the theory in finite array design is straightforward and can be performed in steps:

Step 1: Obtain the $\{Z\}$ matrix ($\{R\} + j\{X\}$) of the finite array through a numerical simulation using a frequency sweep.

Step 2: Solve for the generalized eigenvalue problem $\{X\}\ [I] = \lambda\{R\}\ [I]$. We note that $\{X\}$ and $\{R\}$ are symmetric and real matrices (therefore Hermitian) and so the eignevalues λ and the eigenvectors $[I]$, are real.

Step 3: Define the mode significance parameter as $\alpha = 1 / (1 + |\lambda|)$. Note that when $\alpha \rightarrow 0$ then $\lambda \rightarrow 0$ and so $[V] = \{Z\}\ [I] \rightarrow \{R\}\ [I]$ and therefore the active impedance $[Z_a] \rightarrow [V]. / [I]$ will be almost purely real, thus allowing for a good matching.

From our experience when $\alpha > 0.5$, a good matching is guaranteed. Next, plot α as a function of frequency. A typical graph of the mode significance parameter α vs. frequency, for an 8 x 8 overlapping dipole array (over an infinite ground plane) is shown in Fig. 14. If the frequency discretization is small enough the characteristic modes can be easily tracked by inspecting the graph.

Step 4: For values of $\alpha > 0$ plot the corresponding eigenvectors. A couple of eigenvector distributions (at different frequencies) are plotted over the 8 x 8 aperture as seen in Fig. 15. Although both modes are real, notice that the mode at frequency f_2 has the same sign distribution over the aperture whereas the mode at f_1 changes sign. This suggests that the mode at f_2 will radiate towards the broadside of the array ($\theta = 0^o$) while the mode at f_1 will exhibit endfire radiation ($\theta = 90^o$).

Step 5: Use a suitable mode distribution, such as the mode distribution at f_2, as the excitation of the array for all frequencies. The broadband performance of the mode significance $\alpha > 0.5$ determines the array bandwidth.

The elegance of this method lies in the fact that the modes supported by the physical structure are used for exciting it. This means that N^2 amplitudes and N^2 phases are determined. Via simple math, we can calculate the characteristic impedance of the feeding line (or the value of the resistive termination) that needs to be connected to each port to achieve maximum impedance bandwidth. So the last N^2 unknowns are specified this way.

To demonstrate the efficacy of the method described above, we performed a simple test. We used an 8x8 array of overlapping dipoles (at distance 5.9'' above a PEC ground plane) and fed the elements with the classic, uniform excitation (all amplitudes equal to 1 and all phases equal to 0^o). Next, the elements are fed with the tapered excitation obtained by following the procedure described above. The tapered excitation achieves almost double the bandwidth from the finite array.

The illustration of the finite array design method by an 8x8 overlapping dipole antenna array is shown in Figure 18.

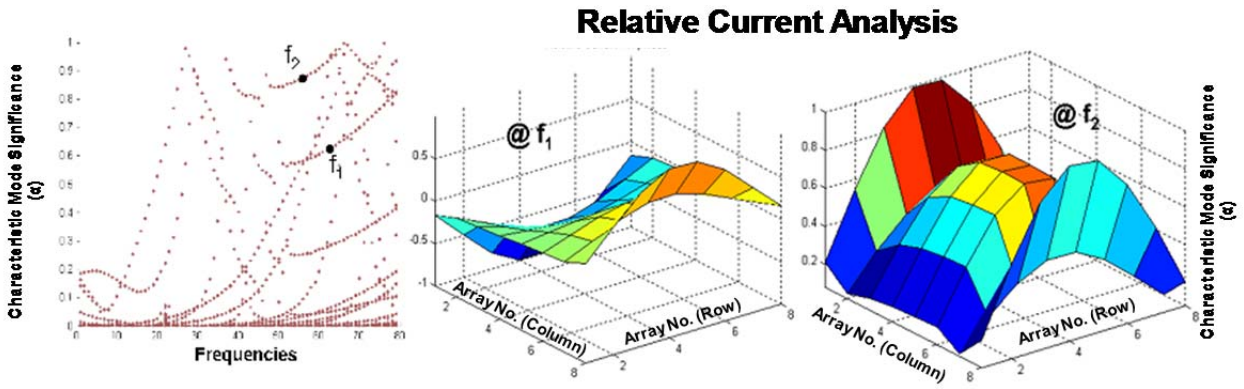

Figure 18 -Mode significance graph for an 8 x 8 array of overlapping dipoles.

3.1.5 8x8 Overlapping Dipole Array on Infinite GP

3.1.5.1 Impedance Bandwidth

Fig. 14 shows the 8x8 overlapping dipole array placed at 5.9'' above an infinite PEC ground plane. The coupling capacitance had to be tuned to achieve maximum bandwidth. The conclusion is that an overlapping section of 30mm would yield a relatively large bandwidth.

The characteristic mode significance curves in Fig. 19 have shifted to lower frequencies as compared to the corresponding graph in Fig. 20. As seen, the scaling of the array elements yielded a significant miniaturization factor. The discrepancy at around 470MHz comes from the finite size resonance due to the aperture size (2' ~ λ @ 500 MHz). It also shows the amplitude taper of the excited feeds (phase is 0^o for all) for the active elements as well as their line termination values. Although the FOPEN specifications are not yet met, especially at the higher end, we proceed to calculate the array gains, radiation patterns and cross-pol levels at certain frequencies, as shown in Fig. 20

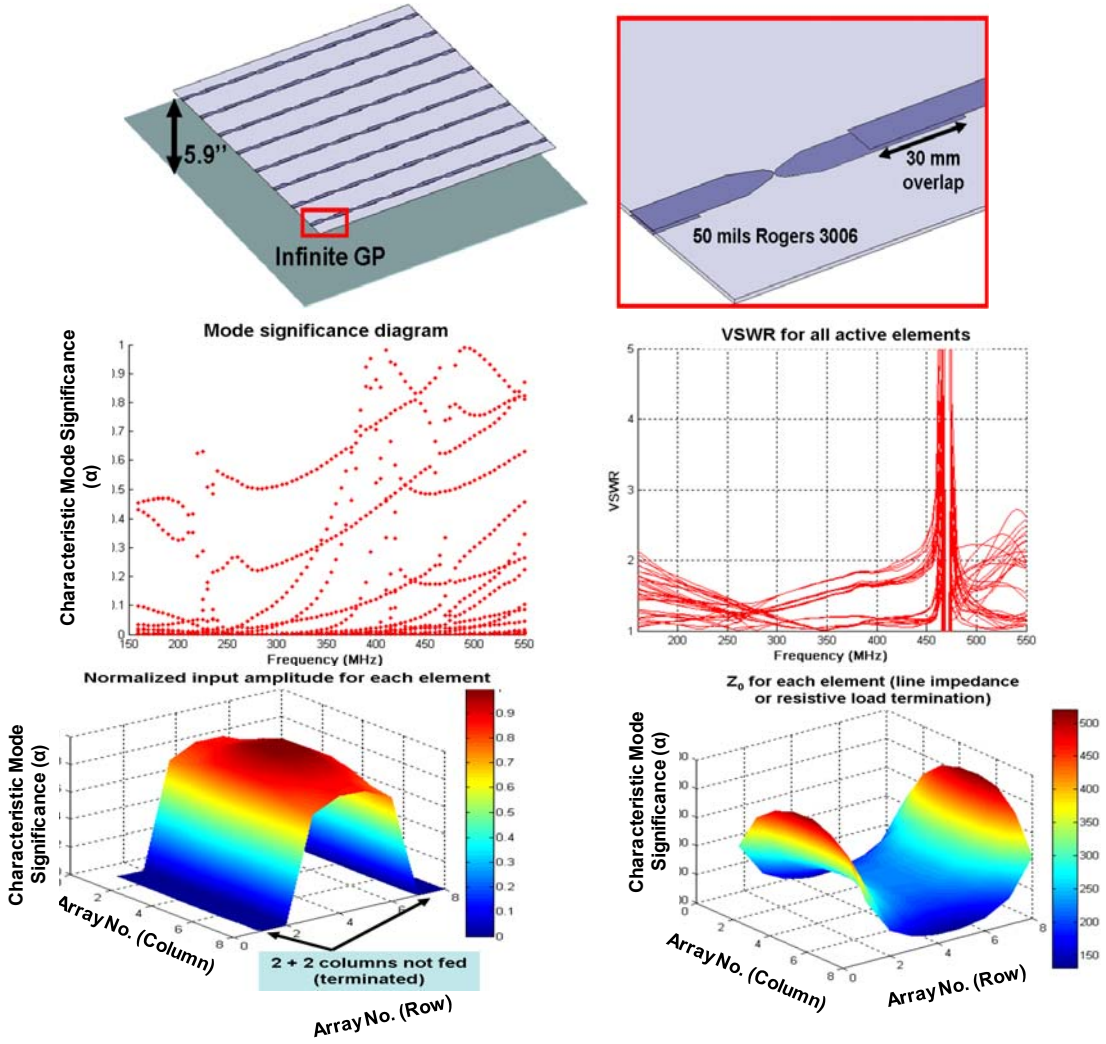

Figure 19 -8 x 8 Overlapping Dipole Array at 5.9'' Above an Infinite Ground Plane.

3.1.5.2 Gains, Radiation patterns and Cross-pol levels

Fig. 15 shows the Gain, Radiation Patterns in the two principal planes ($\varphi = 0^o$, 90^o) and cross polarization levels of the array designed (with an infinite ground plane). Here, antenna gain is defined as the IEEE Gain, which is the directivity times the radiation efficiency ($G = D * e$). No mismatch loss is included but that should be negligible in the 160-430MHz band, where VSWR is < 2:1.

As seen, the aperture distribution calculated through the analysis we presented above yields high gain levels that meet the FOPEN specifications. In summary a gain $G > 8$ dBi is achieved over the entire band. We note again that the gain values shown in Fig. 20 include radiation efficiency (losses coming from resistive terminations). The 60^o, 3dB beamwidth and the >25dB isolation between co- and cross-pol gains all satisfy the FOPEN requirements.

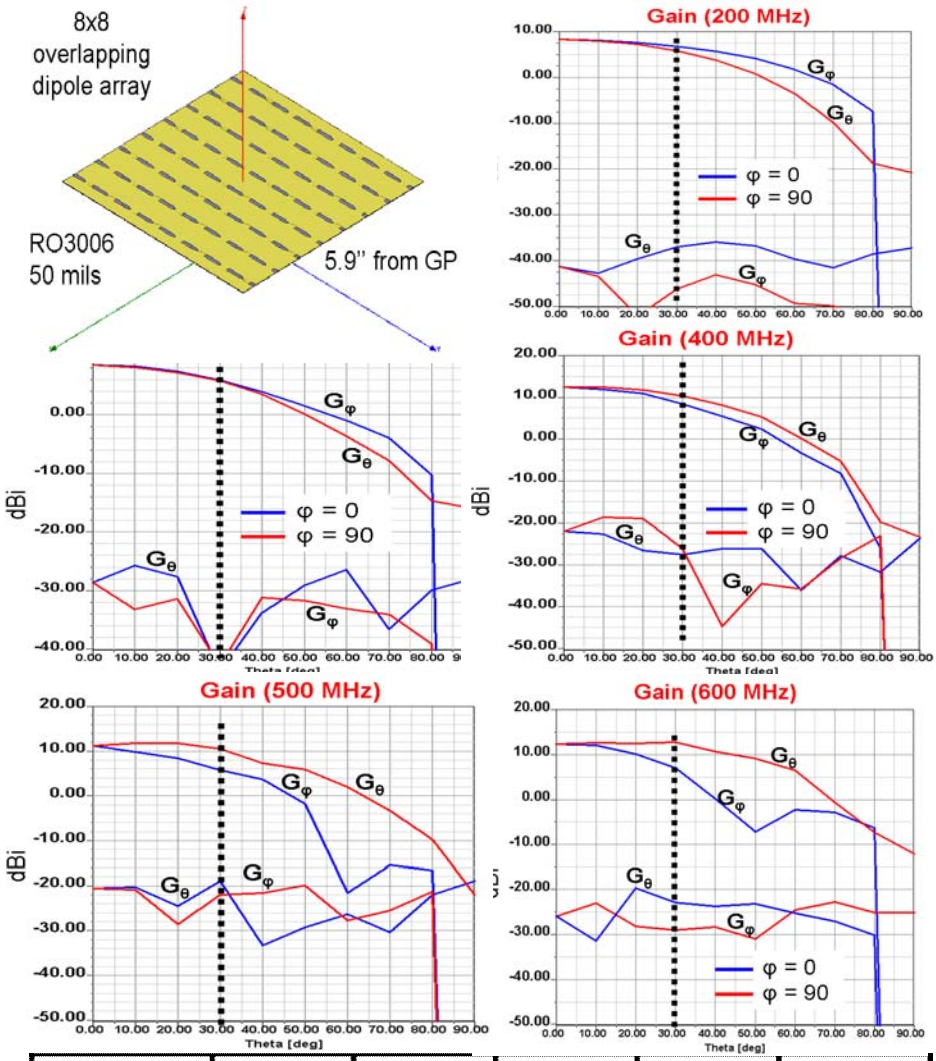

Frequency	200 MHz	300 MHz	400 MHz	500 MHz	600 MHz
Computed Efficiency (HFSS)	37%	65%	79%	88%	97%

Figure 20 -Gain, Radiation Patterns and Radiation Efficiency in Both Principal Planes

3.1.5.3 VSWR Comparison between Zmatrix and HFSS Full Wall Computation

Fig. 21 shows the VSWR of the post-processing Zmartix and HFSS full wave simulation for the configuration of 4x8 active elements embedded in 10x10 array and 8x8 array respectively. Both results show their VSWR results are similar and they are very closely matching from each other.

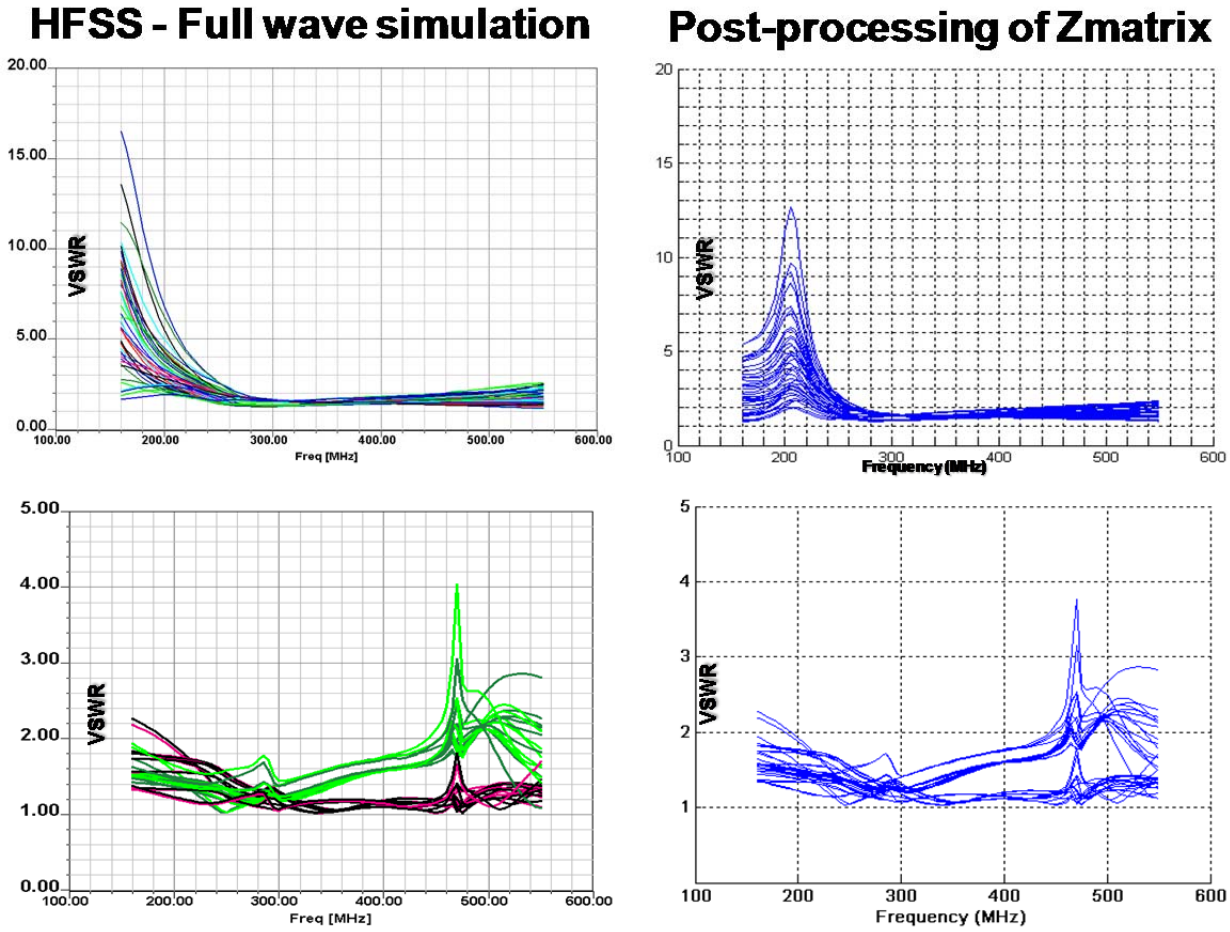

Figure 21 -Active VSWR (4x8 Active Elements Embedded in 8x8)

3.1.6 System Development

"FORESTOR" and TRACER are DARPA programs. FORESTOR operates UHF penetrating Radar over narrow frequency band from 400-450MHz. "TRACER" is follow to a very successful Army investment in FOPEN program. Three TRACER systems have been built and spares are in the process. FOPEN SAR system can be integrated on variety of platforms.

The key TRACER capabilities are fine-resolution less than 1meter at 210MHz. UHF bandwidth penetrating Radar is operated from 235-445MHz, fully polarimetric, huge gains in area coverage versus FOPEN (6-11km swath width for TRACER depending on mode), and easily images dismounts (stationary or removing). TRACER FOPEN SAR Radar will produce resolution 0.7-1.0 Meter. Any increase in upper of frequency and gain will increase system resolution. One of LMA Aero/OSU's objectives in this program is extending upper frequency exceeding 600MHz.

3.1.6.1 FOPEN Requirements

TRACER with the Meta-array will increase the overall FOPEN SAR Radar performances.

Based on the predicted RF performance, FOPEN meta-array will have UWB and good gain at the same time. The analytical prediction shows the upper frequency range can be raised from 450 to above 900 MHz. The projected resolution will be improved from 0.7-1.0 meter to less than 0.5 meter. The increased realized gain will increase RF energy in propagation through foliage.

The FOPEN meta-array requirement is summarized in Table 2.

Table 2 -FOPEN System Requirements

Parameter	Current (TRACER)	Future Objective
Bandwidth (MHz)	**235 - 445**	**235 - 600**
Polarization	**Dual Pol (VV & HH) (Single V & H-Pol Elements)**	**Dual Pol (VV & HH) (Single V & H-Pol Elements)**
Polarization isolation (dB)		**25**
Front-to-back ratio (sidelobes)		**10 dB (one-way) >90° off boresight**
Gain (dBi)	**7.5 (Mid Band)**	**5.0 to 7.0**
3-dB Beamwidth	**> 60°**	**> 40°**
VSWR		**2:1**
Scan capability	**Gimbaled**	**±30° Electronically Scanned**
Size	**24" x 24" x 12"**	**24" x 24" x (3"- 6")**
Power Handling	**0.5 kW Peak , 80 W Average (< 25% Duty Cycle, Nominal Pulse Width 35 μs)**	**1 kW Peak, 200 W Average (Nominal pulse Width 35 μs)**
Weight (lbs)	**10 (Aperture, Ground Plane, Balun)**	**10 (Aperture, Ground Plane, Balun)**

3.1.6.2 TRACER LRU

Figure 22 shows the key electronics associated with TRACER LRU which have been developed for army's program. The developed meta-array will replace the current UHF antenna in the TRACER LRU.

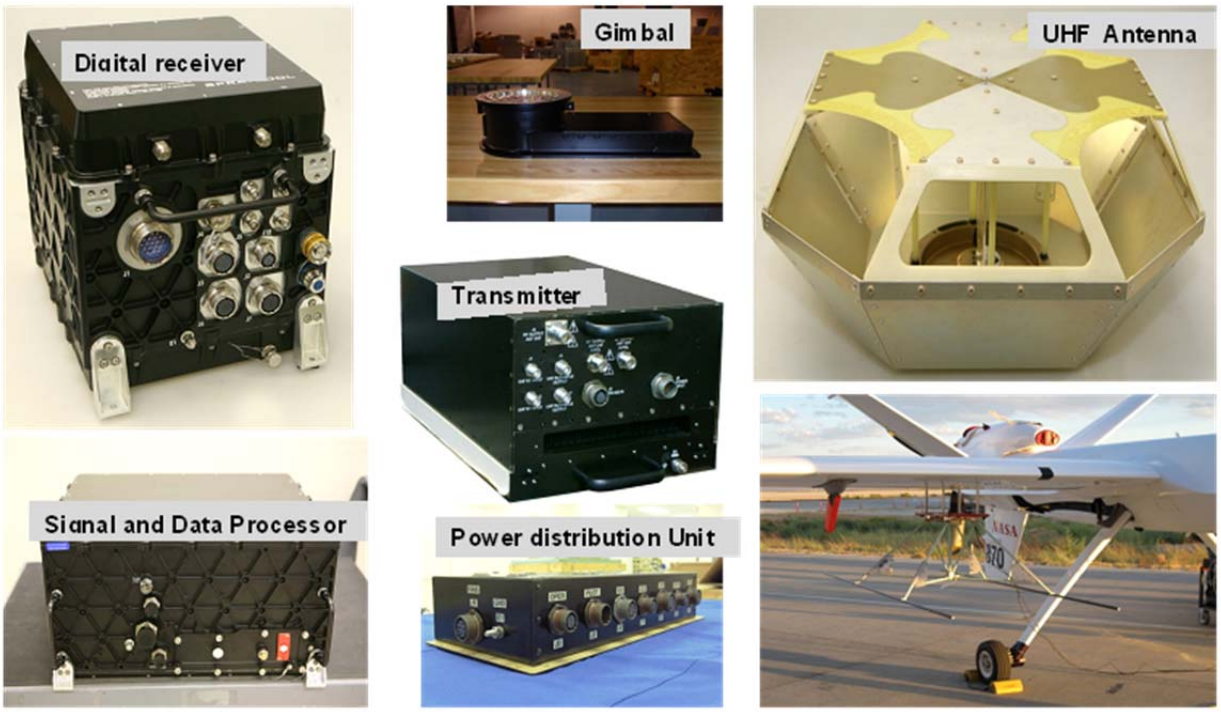

Figure 22 -TRACER LRU

3.2 Phase II -Prototype Development

3.2.1 Optimize 7 x7 Prototype Array RF Performance

In searching for the optimal prototype configuration, five different 7x7 element configurations were investigated to find a Meta-array possess the highest array efficiency. The results are presented in Figures 23 to 26. The predicted results indicate the array design with center active ports and terminated with shorts to the rest of the elements will have the highest radiation efficiency and the best RF.

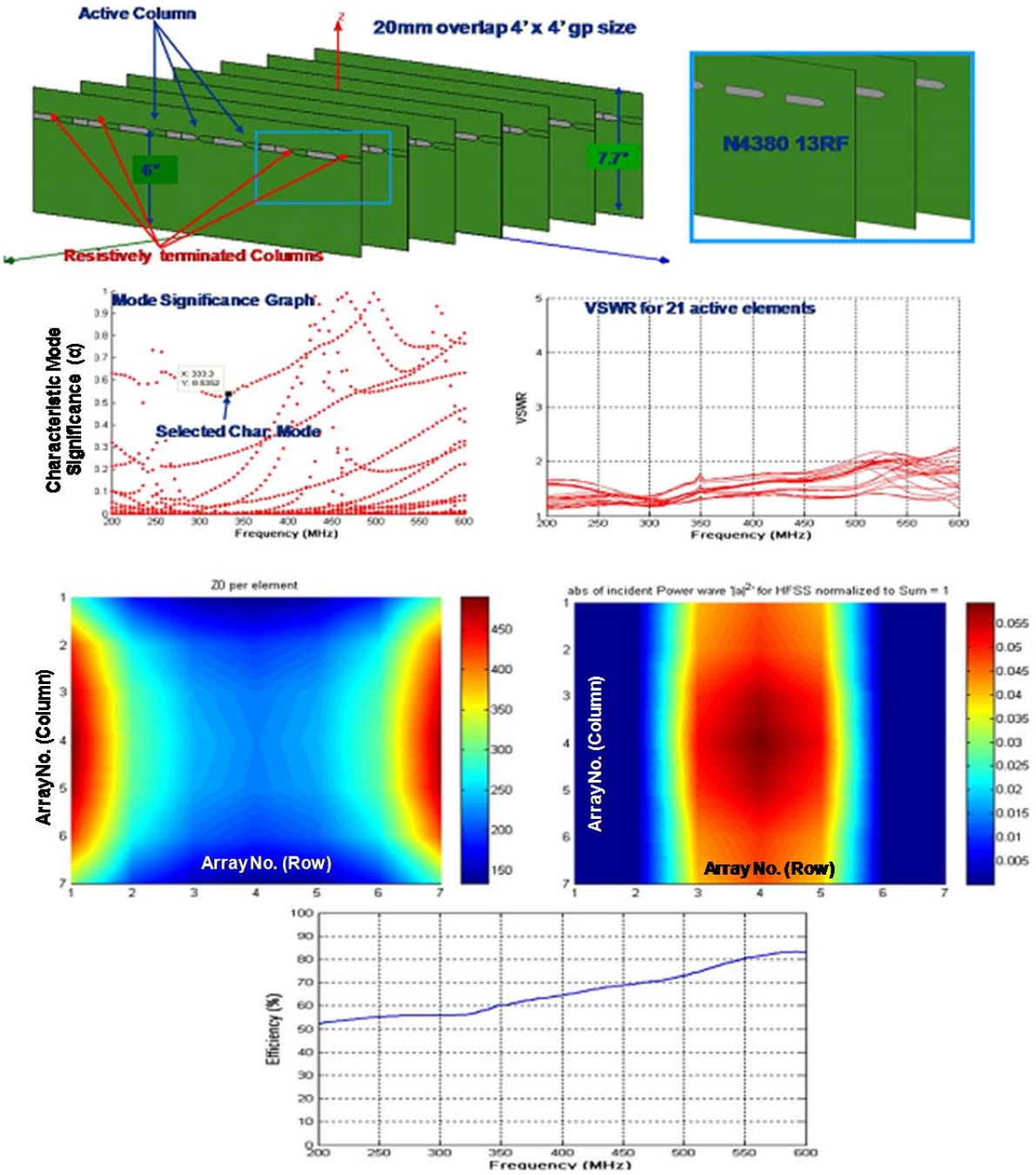

Figure 23 -7x7Array, 3 Center Rows Active Ports and Other Ports Are Resistively Terminated

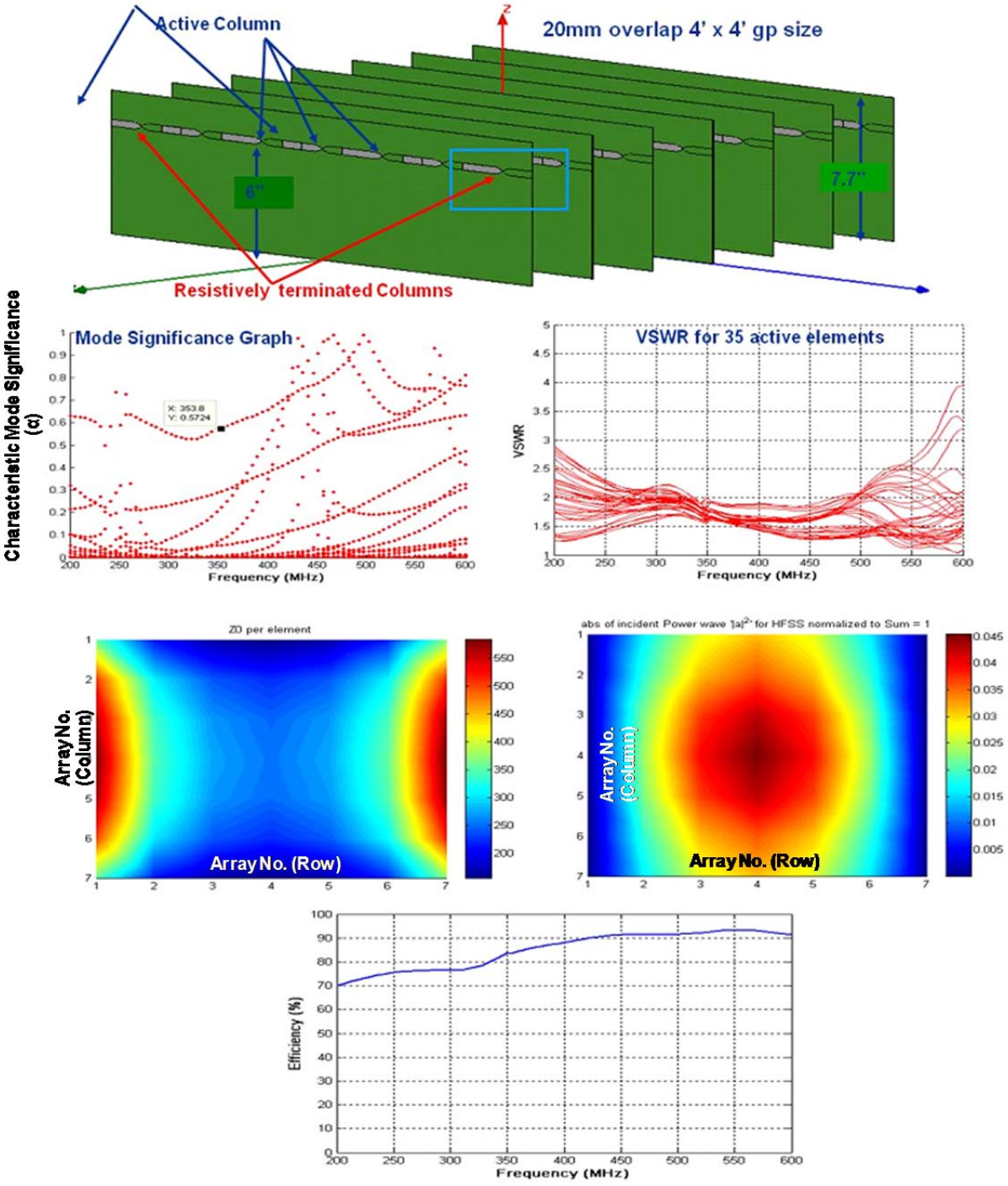

Figure 24 -7x7Array, 5 Center Rows Driven Ports, and Other Ports Are Resistively Terminated

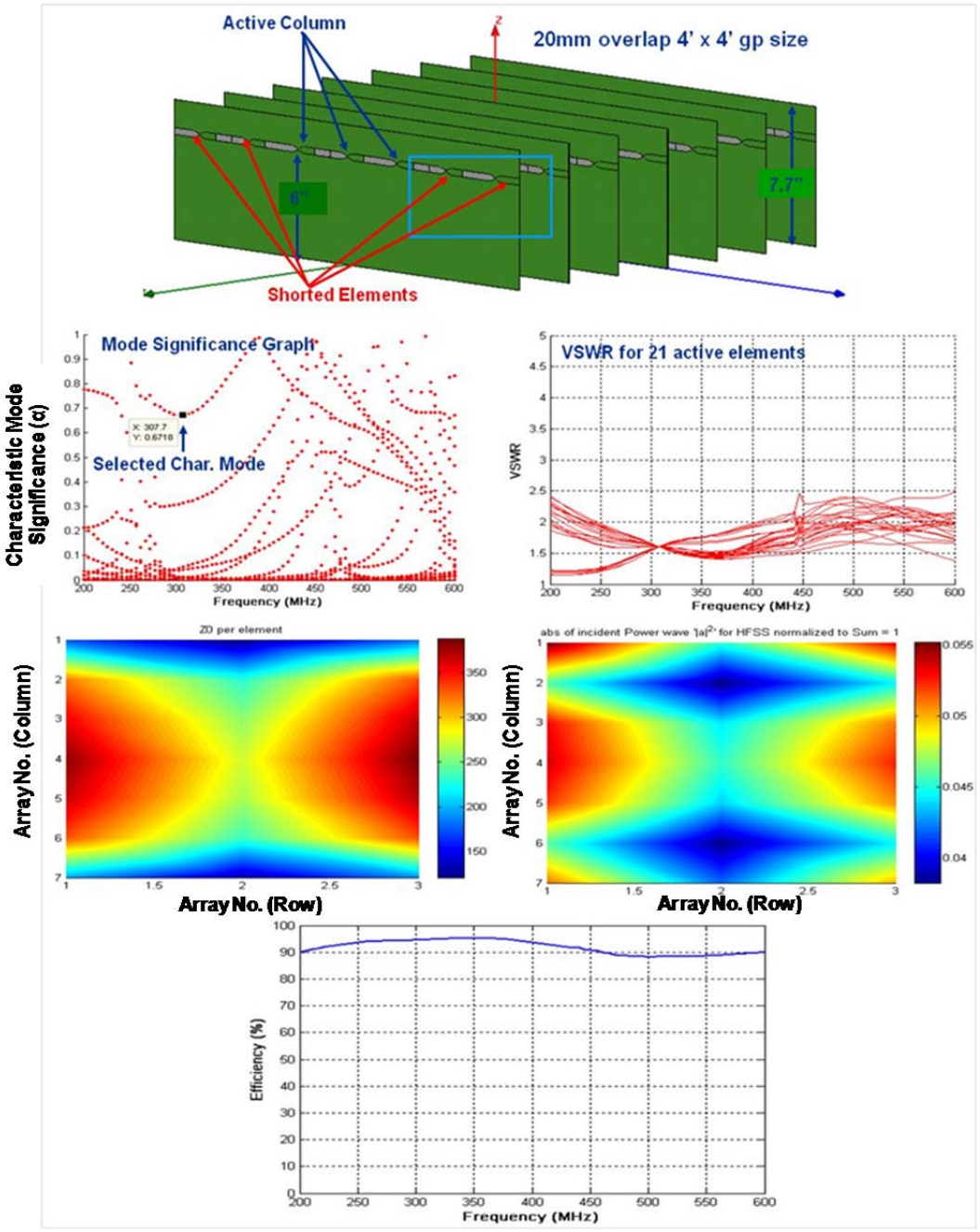

Figure 25 -7x7Array, 3 Center Rows Driven Ports, and Other Terminated with shorts

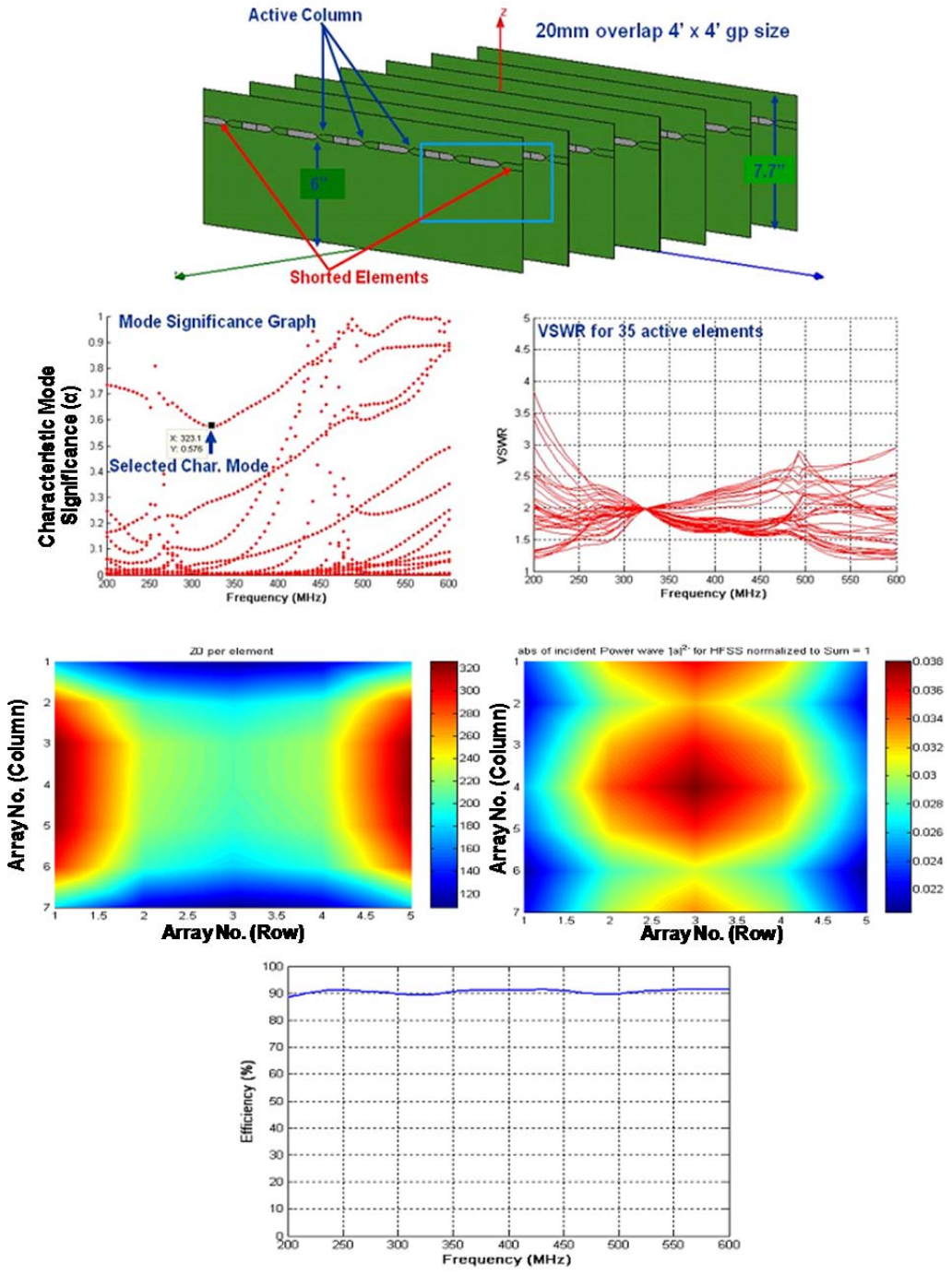

Figure 26 -7x7Array, 5 Center Rows Driven Ports, and Other Terminated with shorts

3.2.2 Optimize 8 x8 Prototype Array RF Performance

Five 8x8 element configurations were investigated to search for the optimal array efficiency and the best RF performance. Fig. 27 is the optimal design which has four center rows active ports and terminated with shorts to rest of elements.

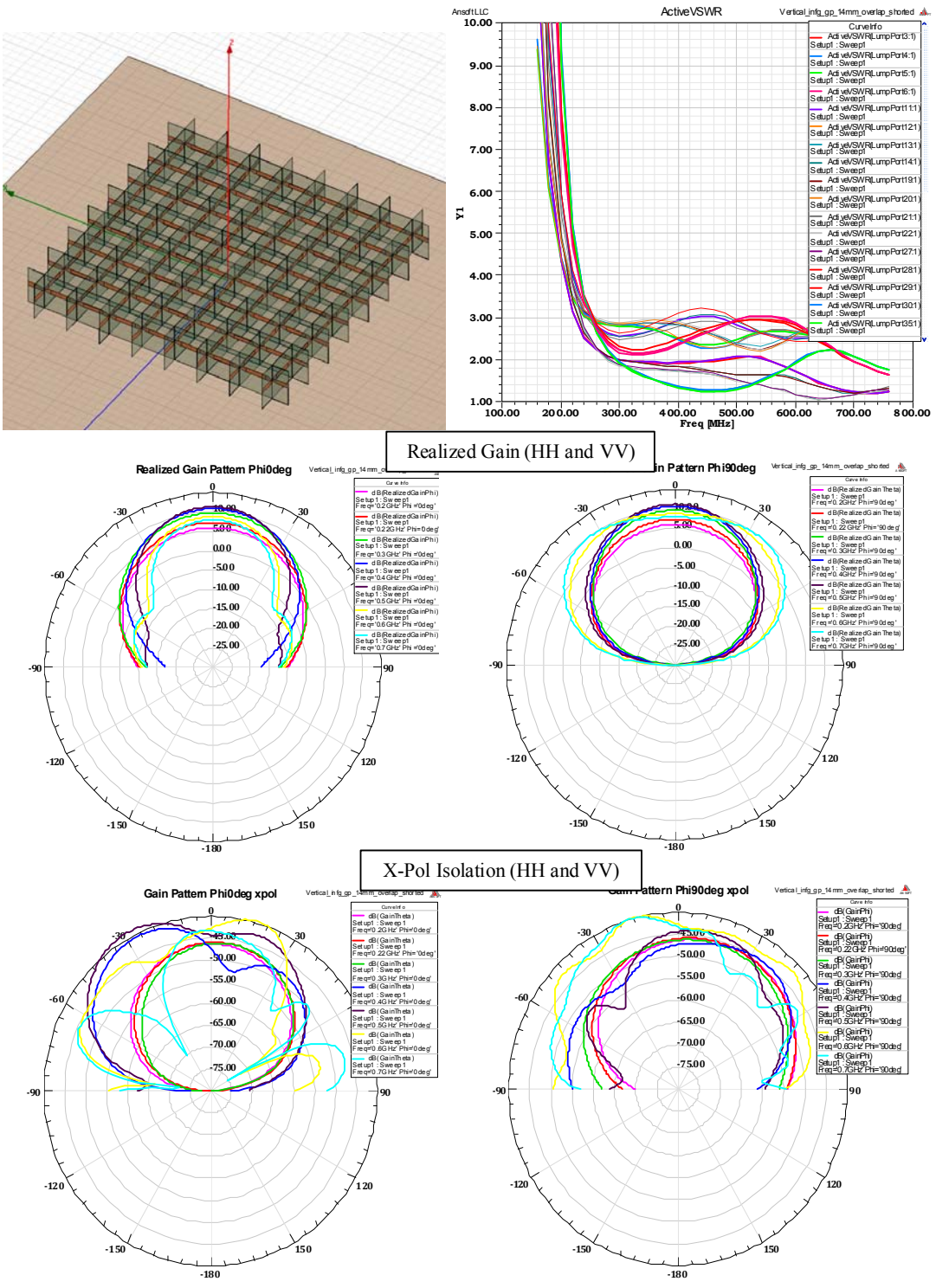

Figure 27 -Dual Pol.,8x8 Array, 4 Center Rows Active Ports, and Other Terminated with shorts

3.2.3 Prototype Development

3.2.3.1 Mechanical Assembly

Concurrent engineering and the best value approach are used to develop the prototypes. Fig. 28 shows the manufacturing methodology which is taken into the account for consideration in four major area. They are listed in the following,

1. **Mechanical Design**
    - Component design
    - Assembly technique
    - Structural and thermal performance
    - Installation for integration

2. **Manufacturing (Materials, Fabrication and Assembly)**
    - Design for low cost and COT
    - Ease of fabrication
    - High reliability
    - Ease of maintainability and repair

3. **Weight and Size**
    - Material and thickness

4. **Operating Environments**
    - Structural and thermal environmental conditions

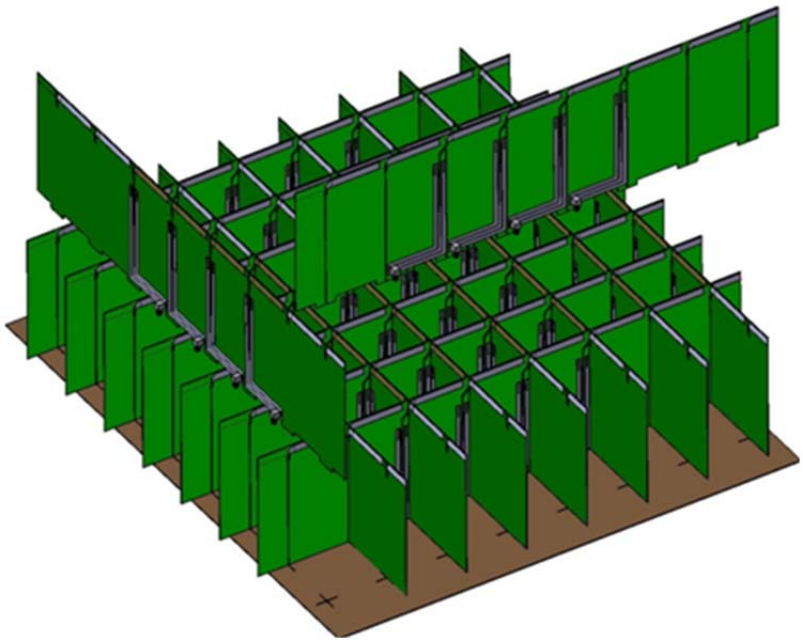

Figure 28 -8x8 Array, Mechanical and Manufacturing Approach

3.2.3.1.1 Prototype (#1, 7x7 Single-pol Array)

LMA worked closely with OSU during the prototype development process to supports to design, fabrication and testing. Fig. 29 shows the Prototype #1 under testing inside the ESL compact range.

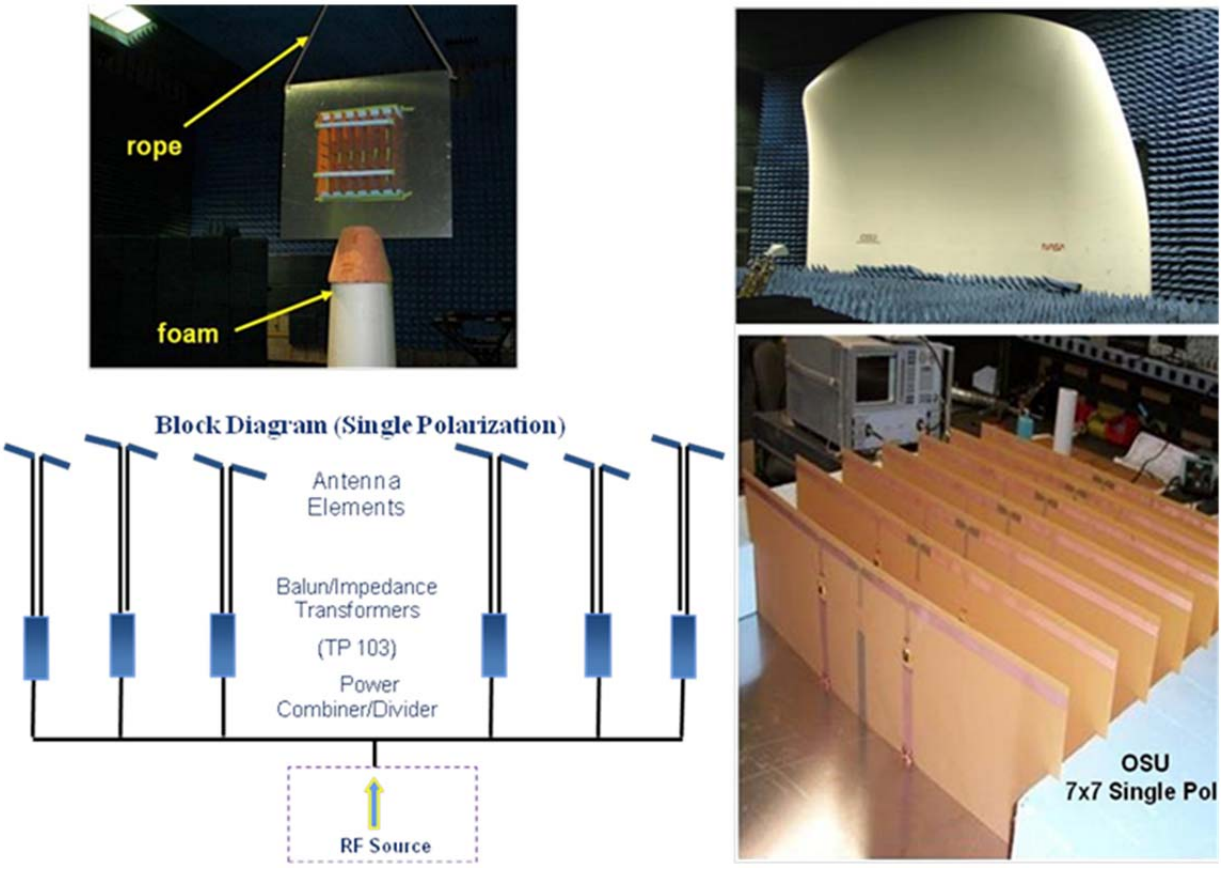

Figure 29 -Prototype #1 (7x7 Single-pol. Array)

3.2.3.1.2 Prototypes (#2, #3 and #4, 8x8 Array)

Figure 30 depicts the configurations of laboratory-scale Prototypes #2, #3 and #4 in egg-crate construction. Prototype #2 is a single polarized (single-pol) array. Prototype #3 and #4 are dual polarized (dual-pol) array.

Prototypes #2, #3 and 4th are designed, fabricated and tested at LMA. Figure 31 shows the detail design and the RF testing conducted at LM Rye Canyon Measurement Facility.

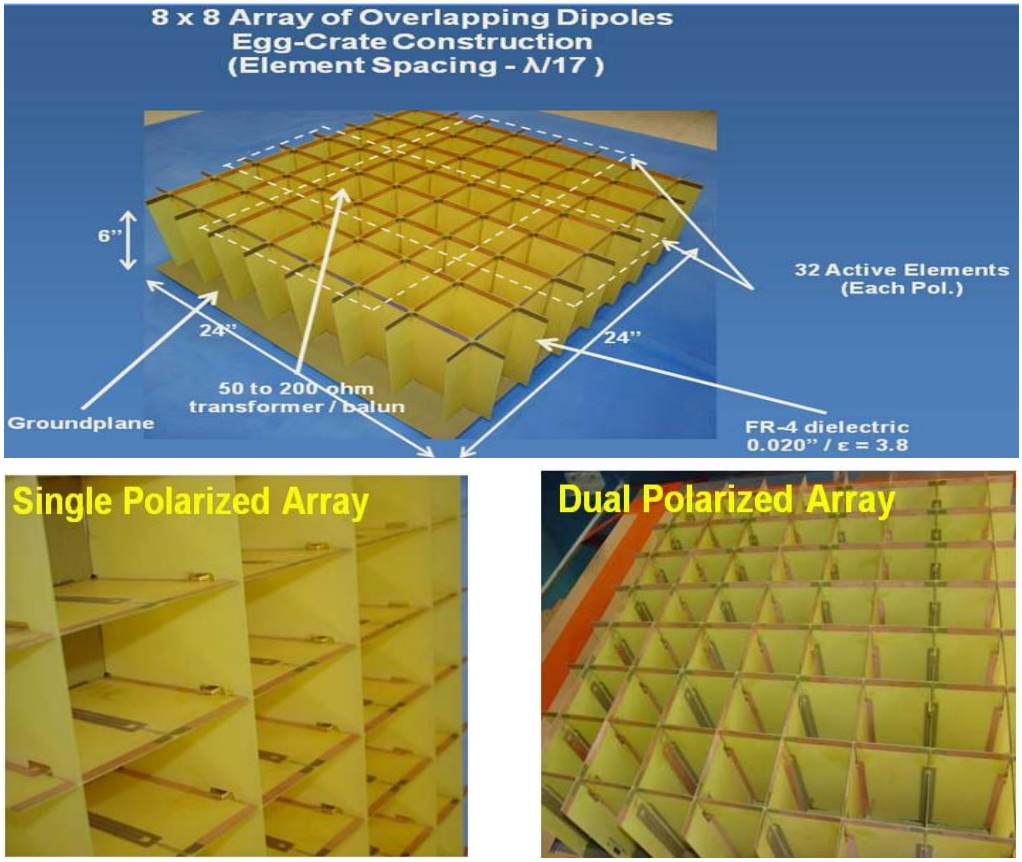

Figure 30 -LMA Prototypes Design and Configuration

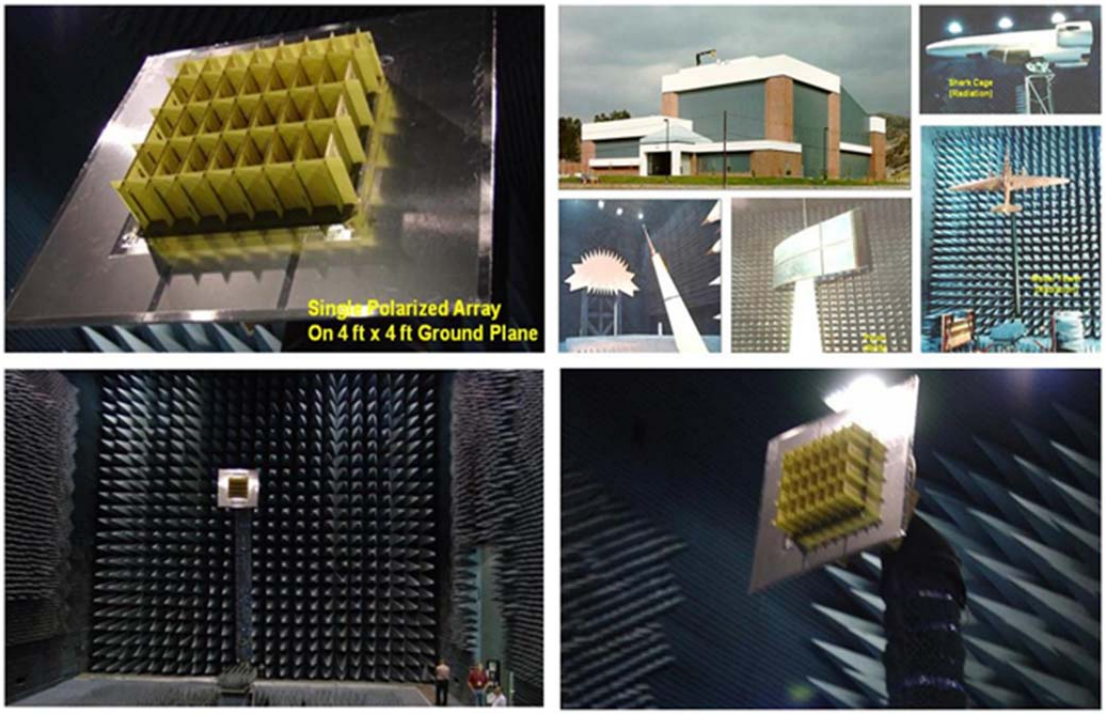

Figure 31 -LM Rye Canyon Measurement Facility

3.2.3.1.3 Prototype #2

Prototype #2 is a single-pol array having active elements in the center four columns fed by a 1 x 32, 50 ohms power distribution network. The 50 ohms impedances are transformed to 200 ohms via 4:1 commercial impedance transformer/balun lumped component. Figure 32 shows the measured VSWR, co-pol. radiation patterns and peak gain.

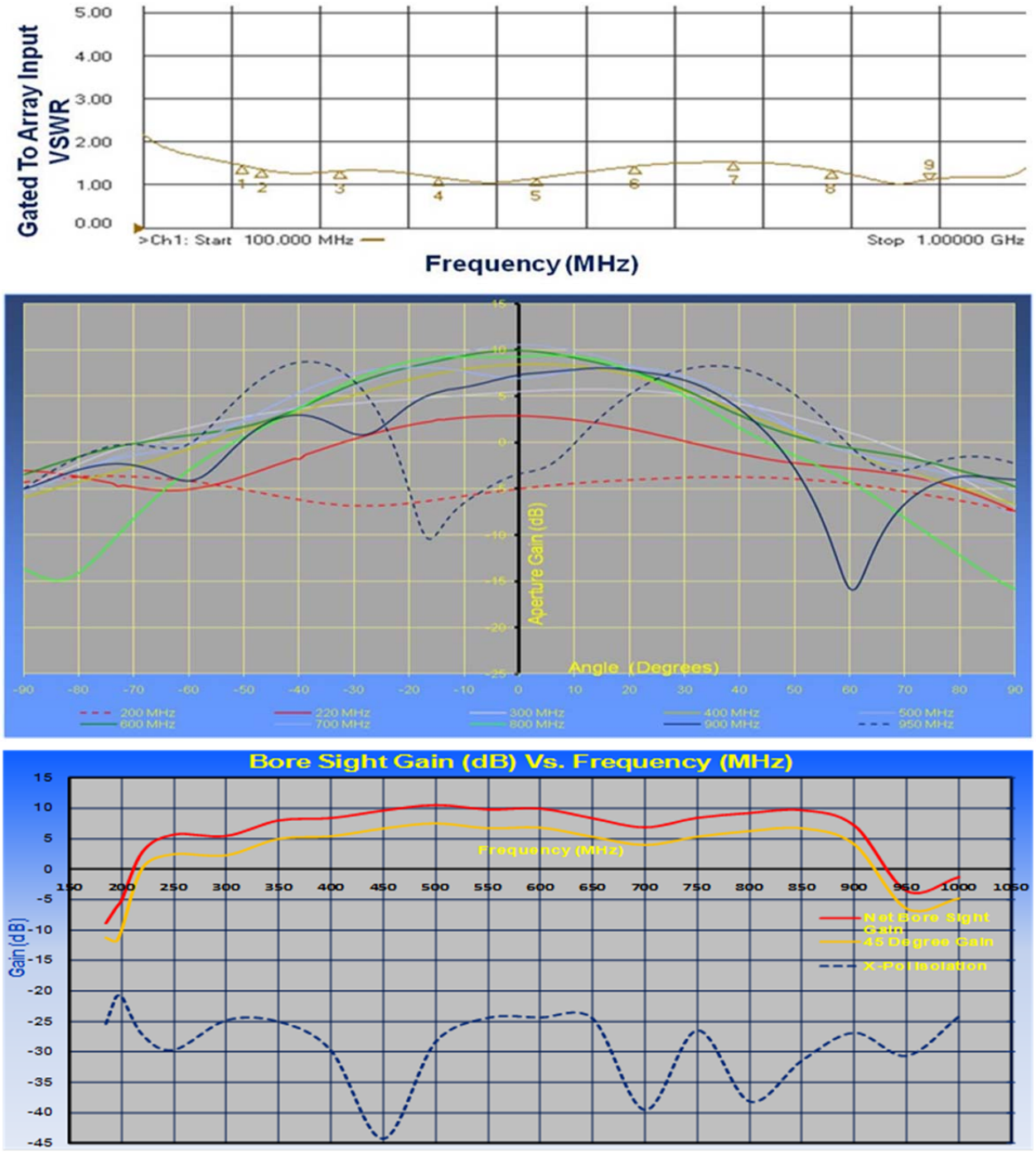

Figure 32 -Prototypes #2 Test Results (8x8 Single Pol.)

3.2.3.1.4 Prototype #3

Prototype #3 is a dual-pol array having center active elements of each polarization are fed by a 50Ω uniform power distribution network. Each 50 ohms active element impedance is transformed to 200 ohms via a 4:1 commercial impedance transformer/balun lumped component. The non active elements are terminated with shorts.

The measured VSWR, co-pol. radiation patterns (V-V and H-H) and peak gains test are summarized in Figure 33.

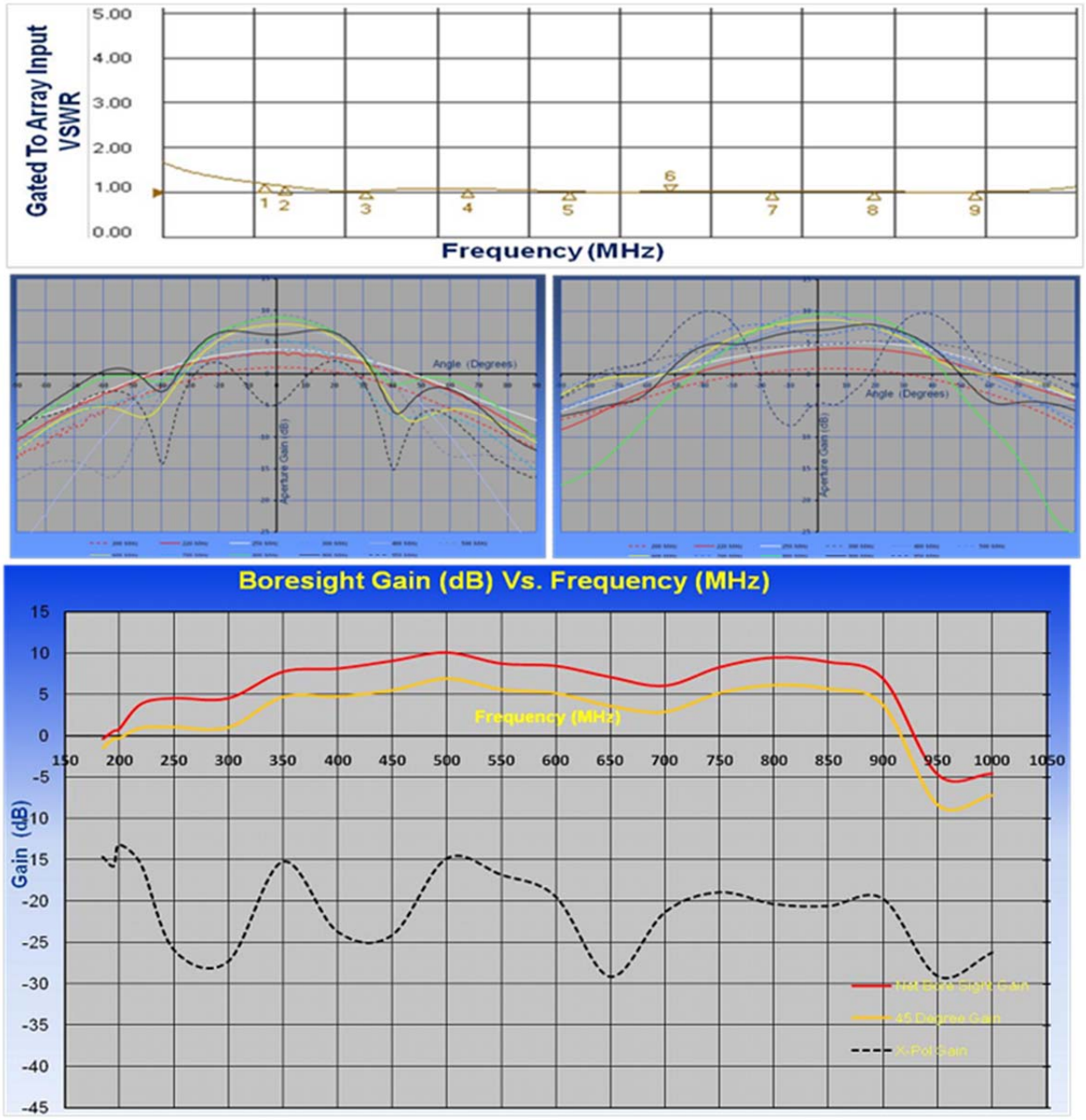

Figure 33 -Prototypes #3 Test Results (8x8 Dual-Pol)

3.2.3.1.5 Prototype #4

Prototypes #1, #2 and #3 use commercial ferrite-core impedance transformer/balun based component, and are only good for testing purposes as they can handle 1 to 3 W of RF input power. FOPEN operation requires transmitting 0.5-1kw peak power and 120cw; therefore low loss/high power customized impedance transformer/balun is needed. Our low loss and cost effective concept is input with a standard coaxial cable at unbalanced, 50Ω impedance and then transformed to balanced antenna element input with a pair of twin lead that have a characteristic impedance of 200Ω.

Our approach to the aforementioned transition is to go through a printed microstrip line and a printed coplanar strip (CPS) line [41]. The input is a 50Ω coaxial cable while the latter is transformed to the 200Ω twin lead pair. The difficulty to the relevant design is fitting the 4:1 impedance transformer/balun in the restricted real estate (max. 5.5") for both impedance transformation ratio and minimum frequency.

Figure 30 is the prototype #4 which has integrated DBE metamaterial co-planar waveguide with impedance transformer/balun on a standard printed circuit material. It fits elegantly within 6" spacing between the overlapping dipole and the ground-plane. Fig. 34 is the design, measurements and comparison with the corresponding simulations over frequency band 200-800MHz. Note that both the simulations and the measurements carried out termination by the twin-lead transmission line with a 200Ω chip resistor and back-back to each other.

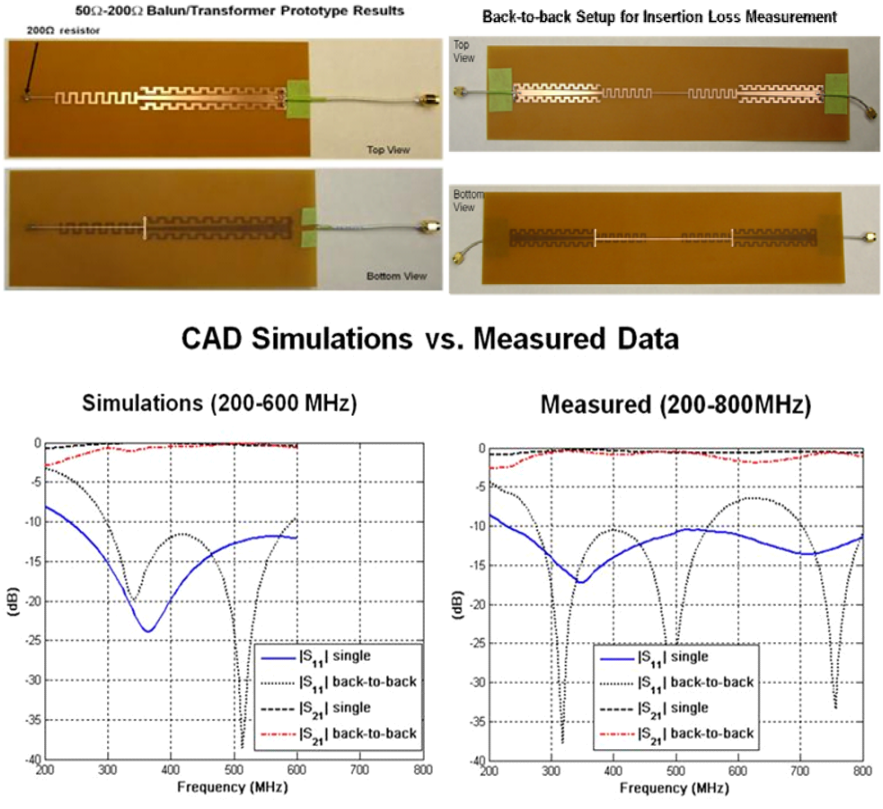

Figure 34 -Wideband 4:1 Impedance Transformer/Balun

3.2.3.1.6 RF Performance

Prototypes #4 has two independent power dividers. The selection of each polarization is by switching a SP2T RF switch with 28V TLL logics. The input RF power will transmit to the corresponding power divider, and then distributed to 32 active elements via the coaxial cables and impedance transformer/balun. Fig. 35 is the measured VSWR in each polarization. Fig. 36 is the measured peak gain and x-pol isolation in each polarization. The peak gain levels are offset by about 2 dB. The variation in peak gain level is the resultant due to mismatch of impedance transformer/balun. This can be eliminated or improved by controlling the manufacturing process and design tolerances.

Fig. 37 is the measured radiation patterns. The rapid changing of gain is close to x-pol position; therefore measuring accurate x-pol isolation is extremely difficult. Reasonable x-pol isolation accuracy requires very slow rotation rate and high angular resolution during the measurement.

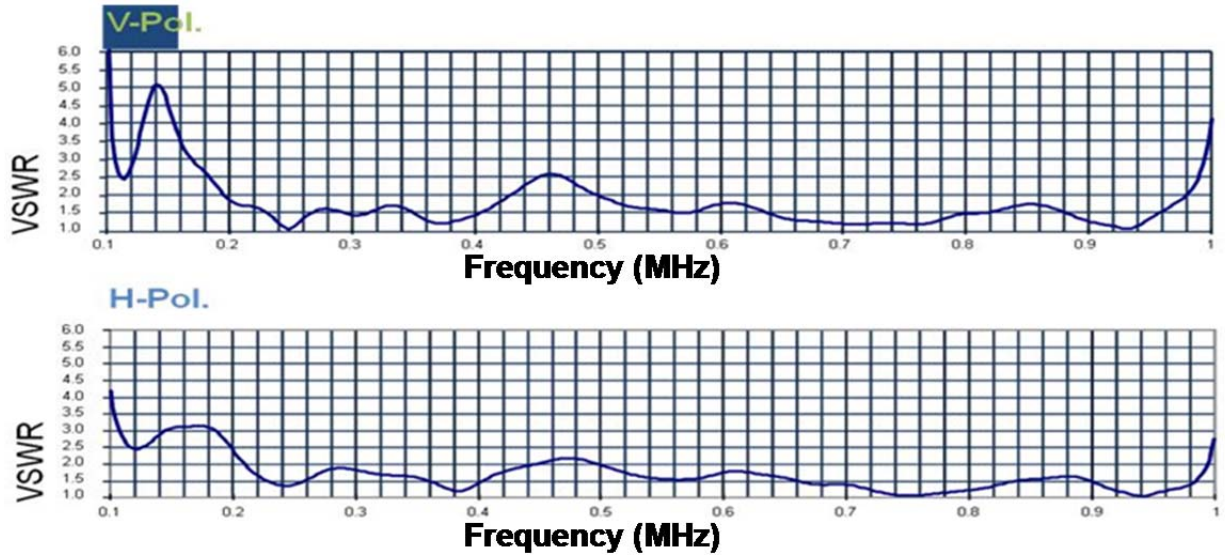

Figure 35 -Gated Active VSWR

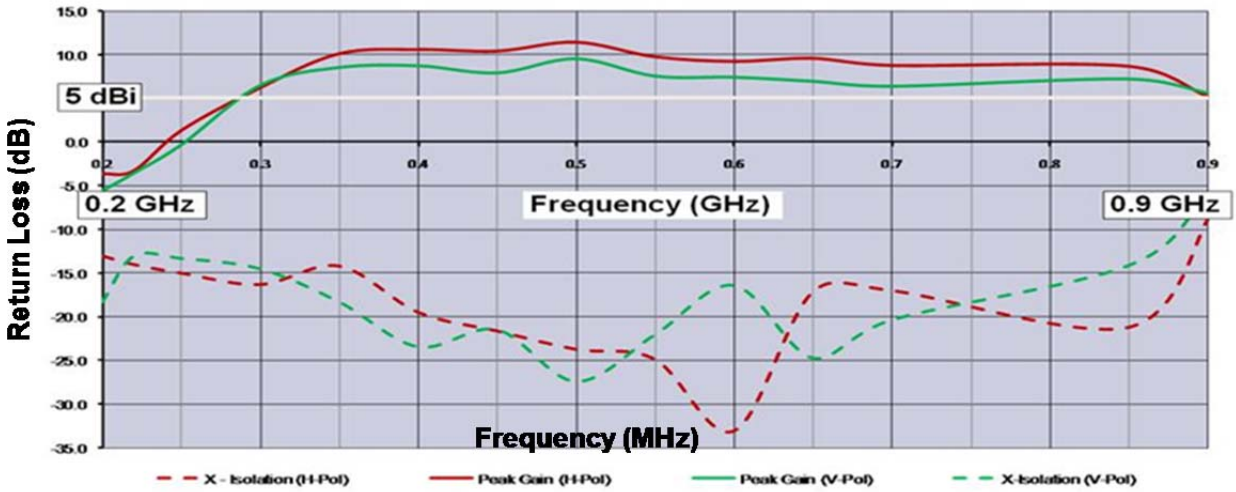

Figure 36 -Peak Gain and X-pol Isolation

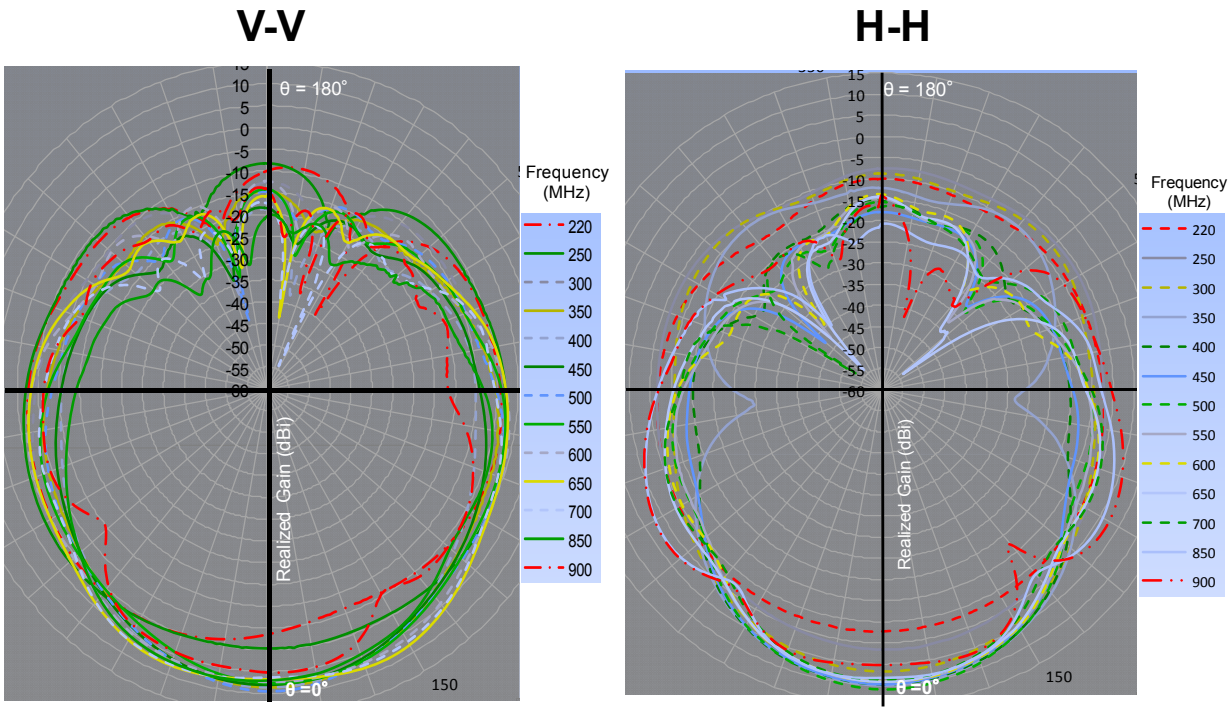

Figure 37 -Radiation Patterns (V-V and H-H)

3.2.3.1.7 Beam Scanning

FOPEN SAR Radar requires steering antenna beam during operation. Current TRACER system uses mechanical gimbals' rotation to steer the beam.

The FOPEN meta-array has the phase array features, and should be able to steer antenna beam by applying certain phase distribution to the active elements. LMA believes it is an advantage to future FOPEN system to incorporate electronic beam scanning as part of future requirement.

Fig. 38 shows how an array changing its $\Delta\phi$ distribution can result in beam scanning in θ^{o}. The beam steering in this section is a feasibility study to understand the electronic scanning of FOPEN meta-array. LMA/OSU applies HFSS full-wave model to prototype #4 for the understanding of phase distribution required to steer the meta-array antenna beam.

Figs. 39 and 40 show the predicted beam scanning patterns in 0°, 10º, 20° and 30º θ directions by altering different delta ϕ phase distributions. We have no attempt to optimize the beam scanning patterns at this time.

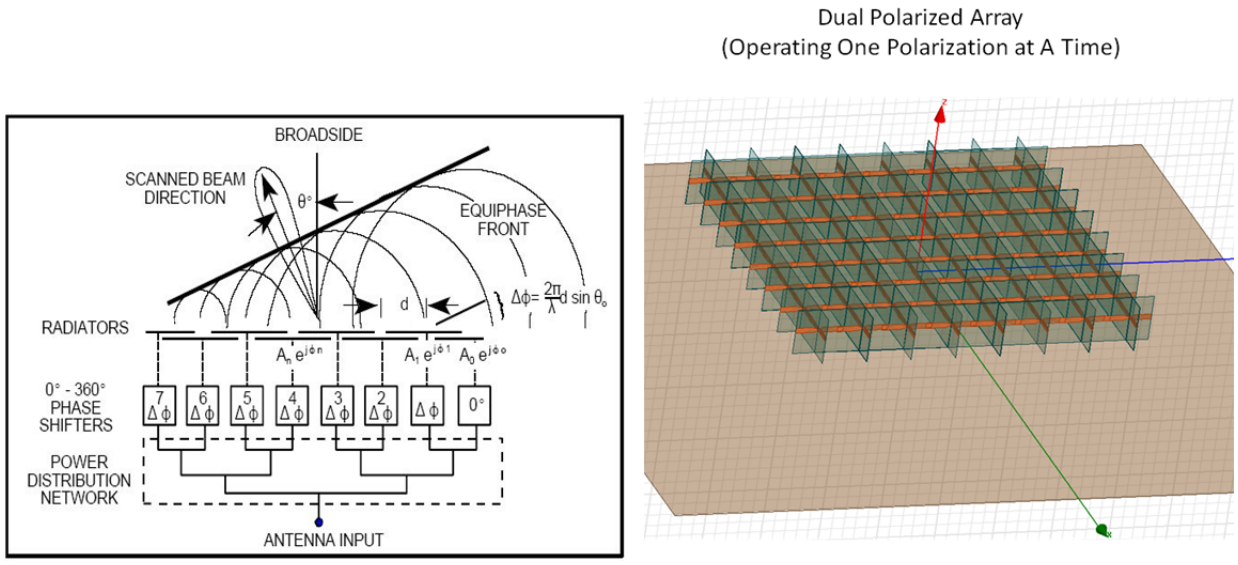

Figure 38 -Beam Scanning Concept and HFSS Simulation

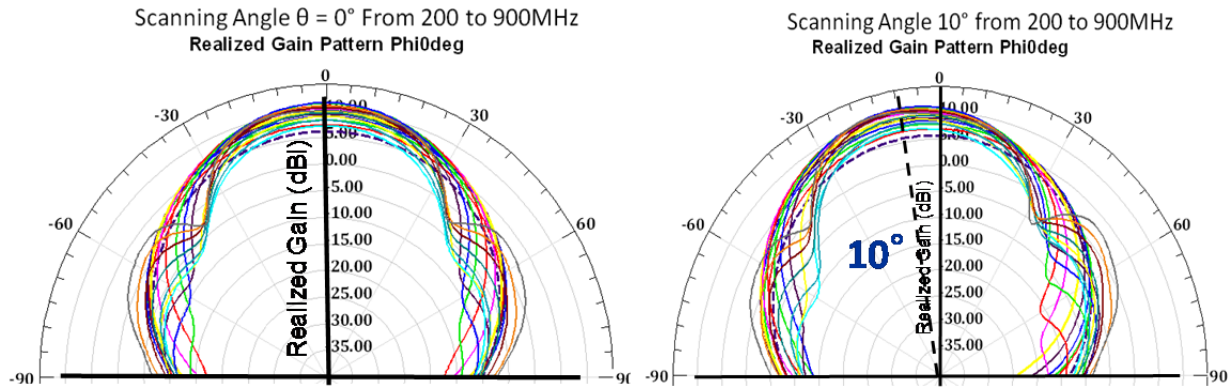

Figure 39 -Simulated Dual Pol. 8x8 Array in 0º and 10º Beam Scanning

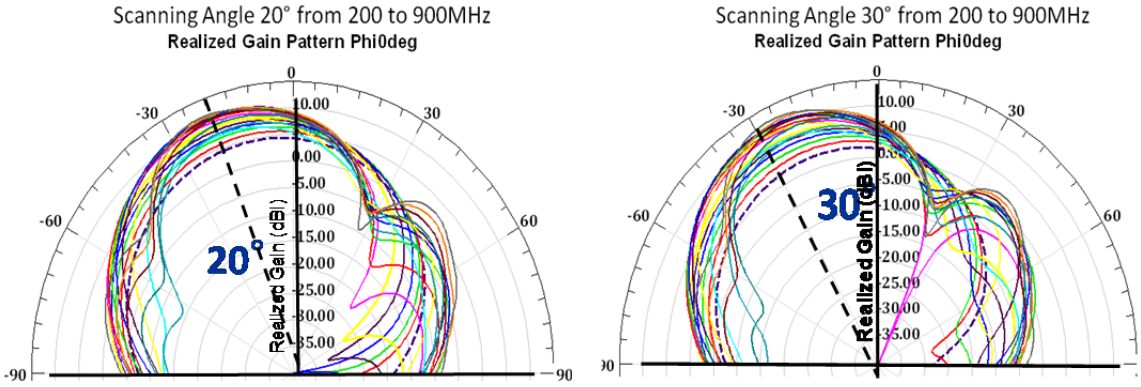

Figure 40 -Simulated Dual Pol. 8x8 Array in 20º and 30º Beam Scanning

3.2.3.1.8 Beam Steering Measurement

LMA has demonstrated the electronic beam steering concept by trimming the coaxial cable length to match a specified $\Delta\phi$ phase distribution to yield 10° θ beam scanning. Fig. 41 shows the installed phase trimmed coaxial cables in between the impedance transformer/balun and the 1x32 in phase uniform power divider.

Fig. 42 shows the measured the active VSWR and 10° θ beam scanning. The result shows a single phase distribution can result in broadband scanning without customized phase tuning to each frequency. The measured active VSWR distortion is very small under the 10° θ beam scanning.

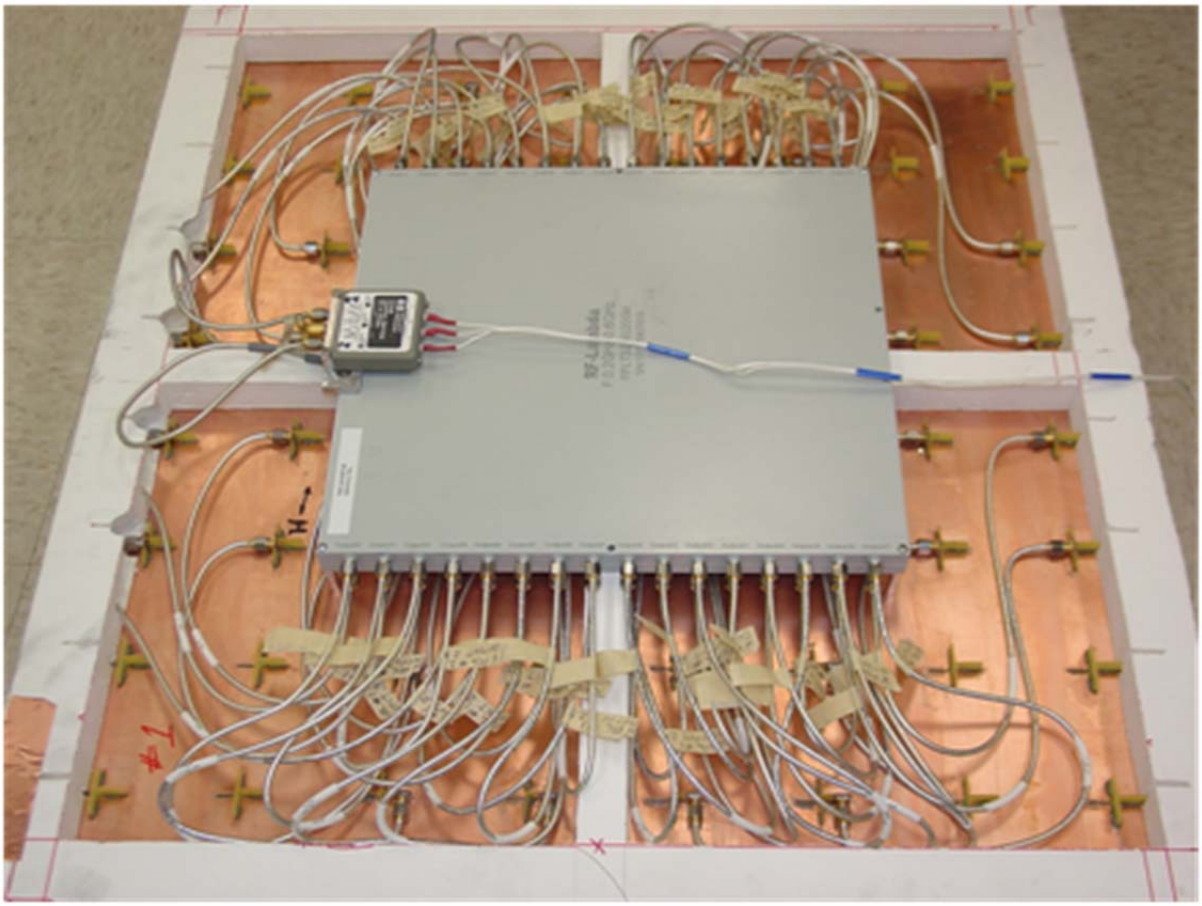

Figure 41 -Corporate Feeding Network

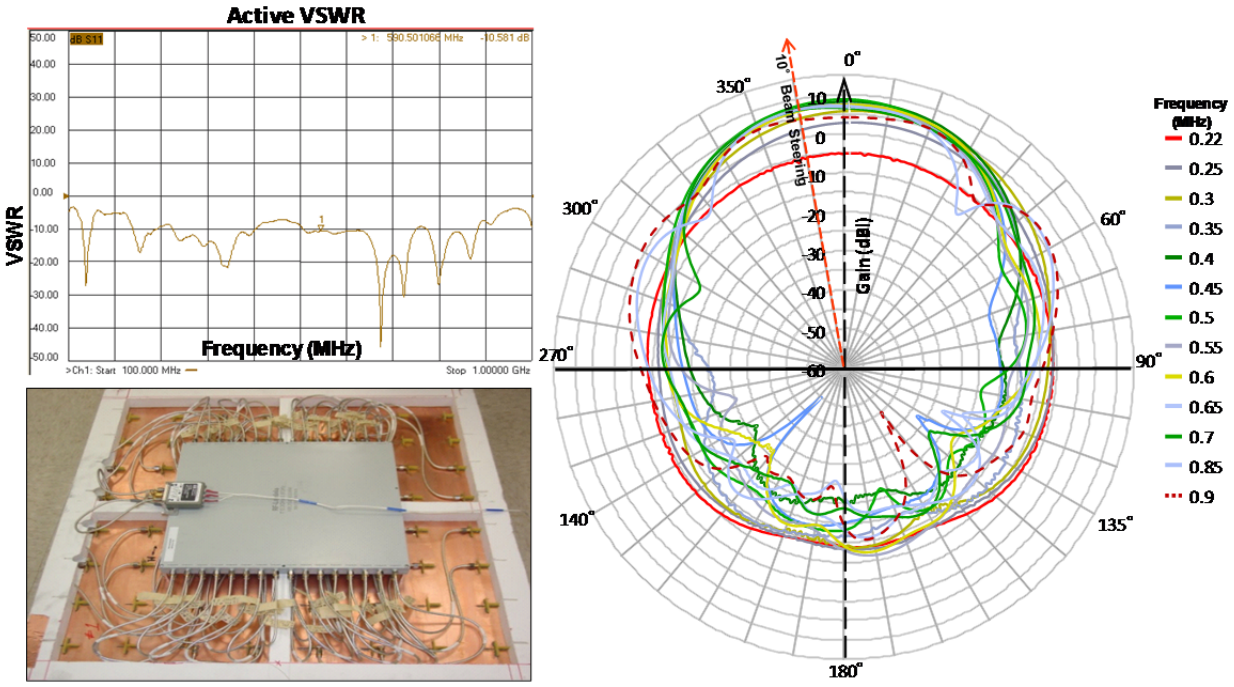

Figure 42 -Measured 10º Beam Scanning over Frequencies

3.3 Phase III - Integration

LM Aero has begun integration efforts since May 2011. Fig. 43 shows the integration concept of FOPEN meta-array onto C-130 Shadow Harvest sensor pod.

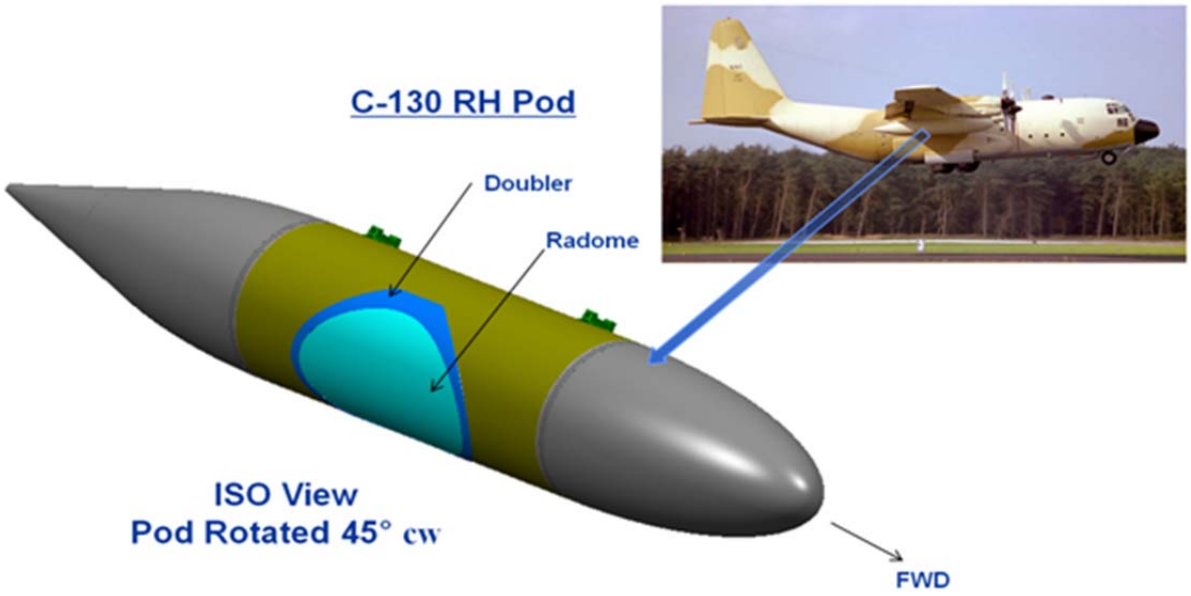

Figure 43 -Integrated Assembly on C-130 Shadow Harvest Sensor Pod

3.3.1 Integrated Assembly Concept

The C-130 Shadow Harvest sensor pod has a 45" diameter uniform tubular section. The center section provides sufficient depth and ground plane size to house the 8x8 dual-pol prototype. The cut away of center body is stiffened with structural supports made from a metal conical ring and a composite RF radome. The connecting coaxial cables, power dividers, switch, and electronics are installed below the supporting ring. Fig. 44 shows the details of integration.

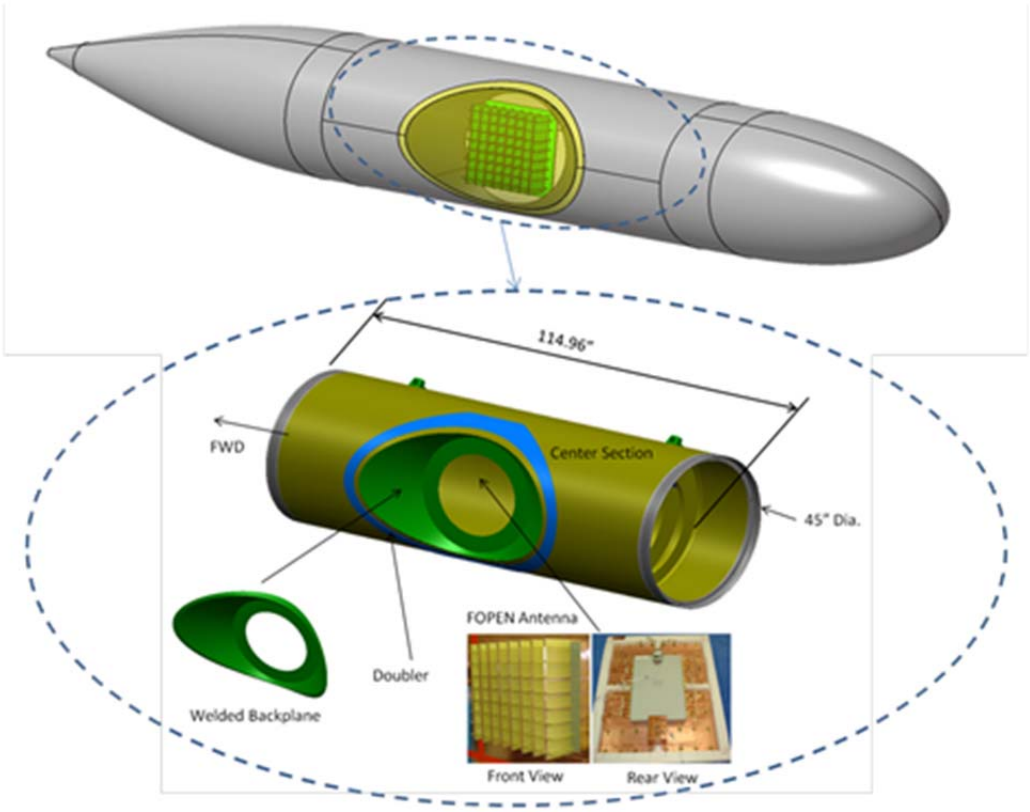

Figure 44 -Integrated Assembly Detail

3.3.2 Prediction and Optimization of Integrated Assembly

LM Aero has analysed the RF performances of FOPEN meta-array integrated onto a C-130 Shadow Harvest sensor pod. Fig. 45 shows the realized gain level is depending on the orientation of the E-field with respect to the sensor pod orientation. Figs. 46 and 47 show the radiation patterns in three different sensor pod orientations respect to E-field.

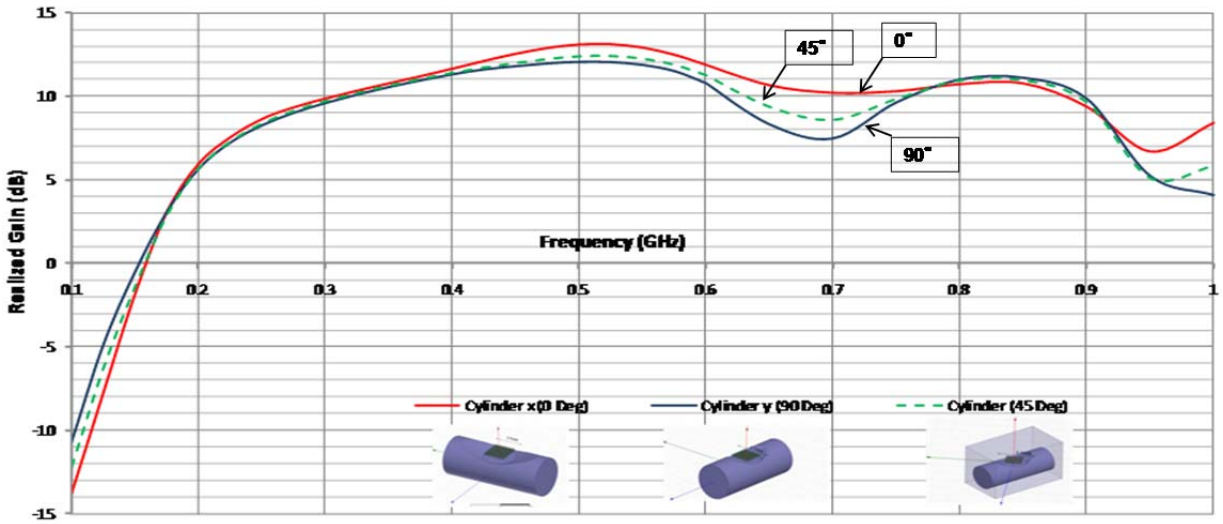

Figure 45 -Realized Peak Gain in Three different orientations respects to E-Field

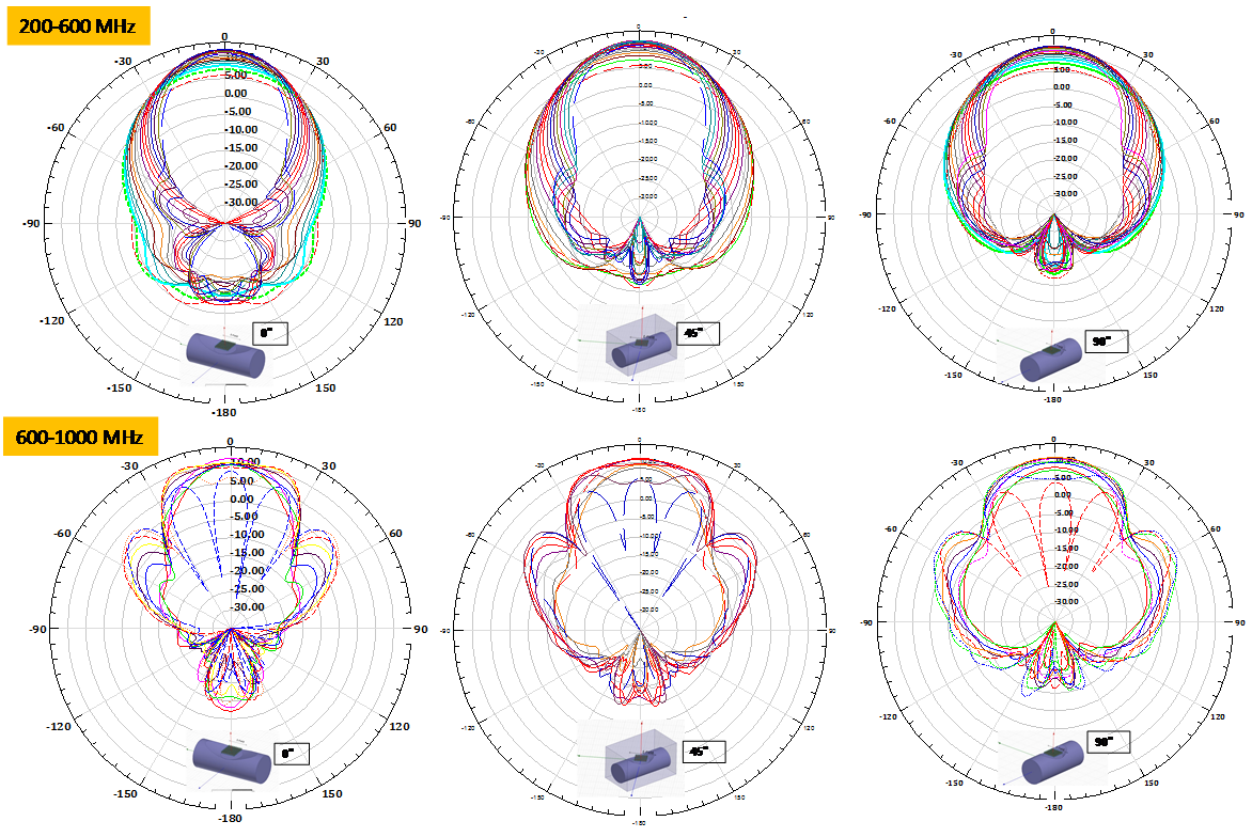

Figure 46 -Radiation Patterns in three different orientations with respect to E-field, Phi=0º

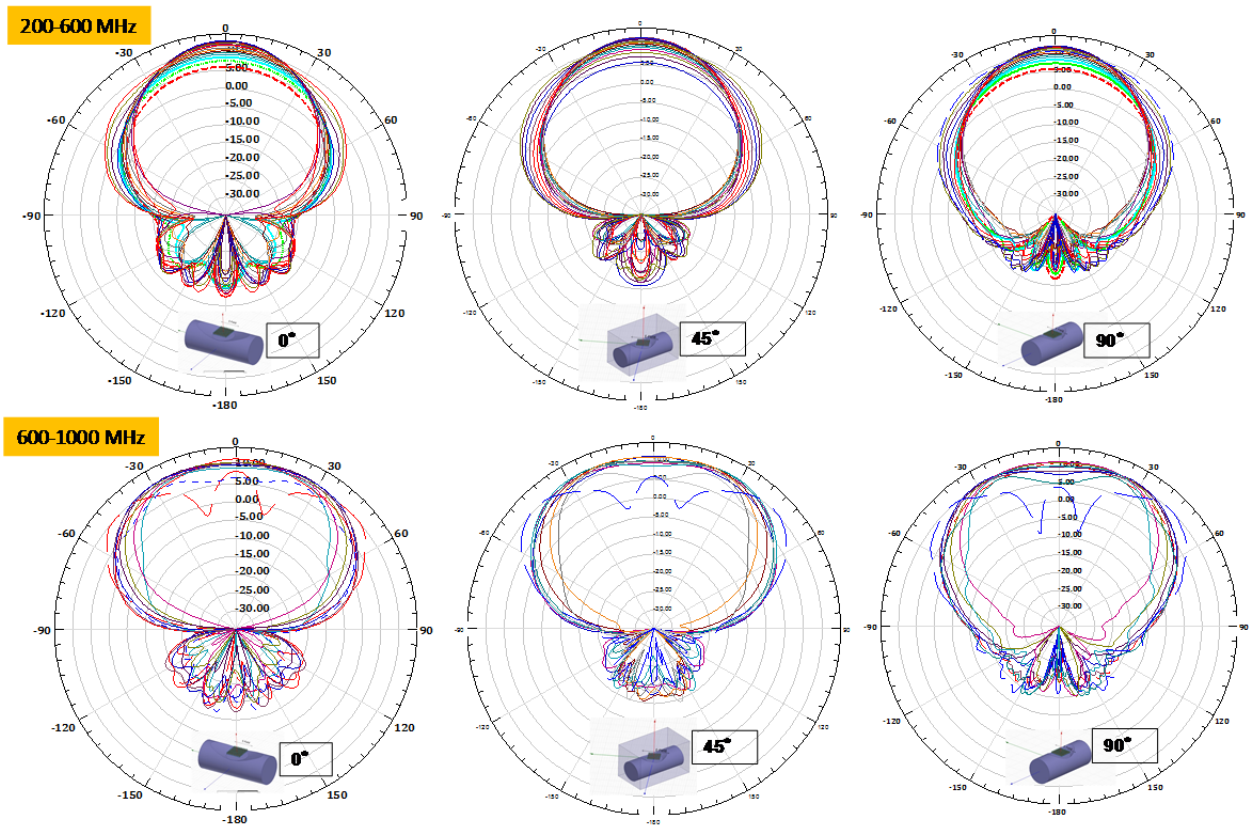

Figure 47 -Radiation Patterns in three different orientations with respect to E-field, Phi=90º

3.3.3 C130 Shadow Harvest Sensor Pod Replica

Fig. 48 shows the construction of C-130 sensor pod which weights more than 1000 lbs. The final integration assembly with FOPEN meta-array will exceed the maximum positioner load capacity for RF measurement. An alternative solution is fabricating a replica of C-130 sensor replica with lighter weight, identical physical dimensions and electrical properties for RF testing.

Figs. 49, 50, and 51 show the overall construction of the C-130 Shadow Harvest sensor pod replica, consists of three separable sections (nose, mid and tail) bolted together to form a 26 ft structure. The nose and tail are fabricated with E-Glass “C” sandwich construction and the mid section is a graphite composite construction reinforced with aluminium frame structure. The C-130 Sensor Pod replica is supported by a customized adapter plate with matching attachments to the positioner.

The C-130 Shadow Harvest sensor pod replica is designed by LMA and fabricated at a local subcontractor. Figure 52 shows one of the lamination tooling used for composite layup.

The centre tubular body has been coasted with silver paint to provide proper conductivity surface.

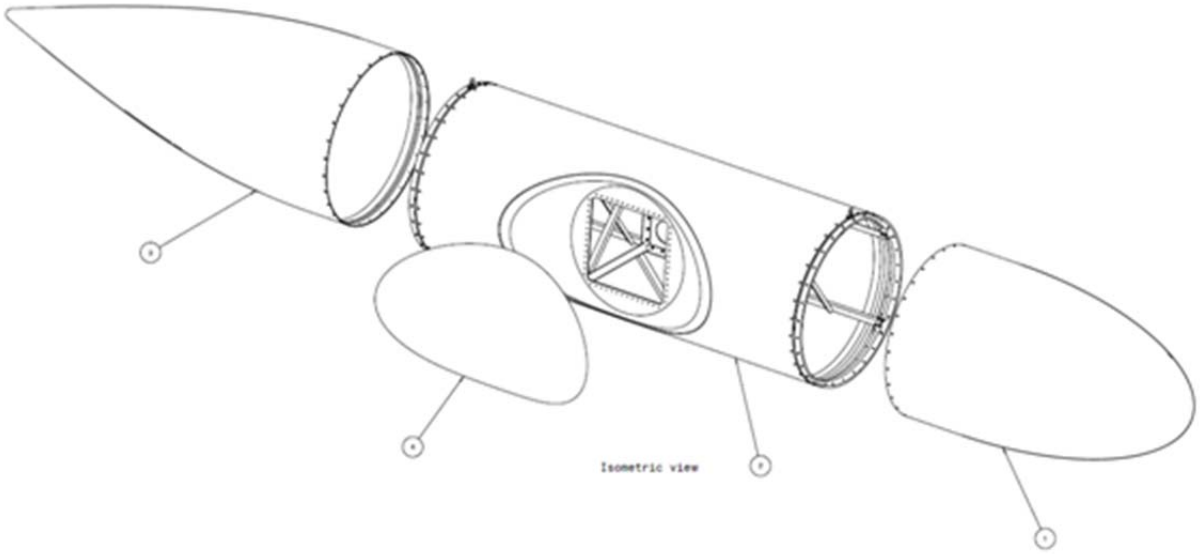

Figure 48 -C130 Sensor Pod Replica

(Nose and Tail Section with E-Glass and mid Section with Graphite)

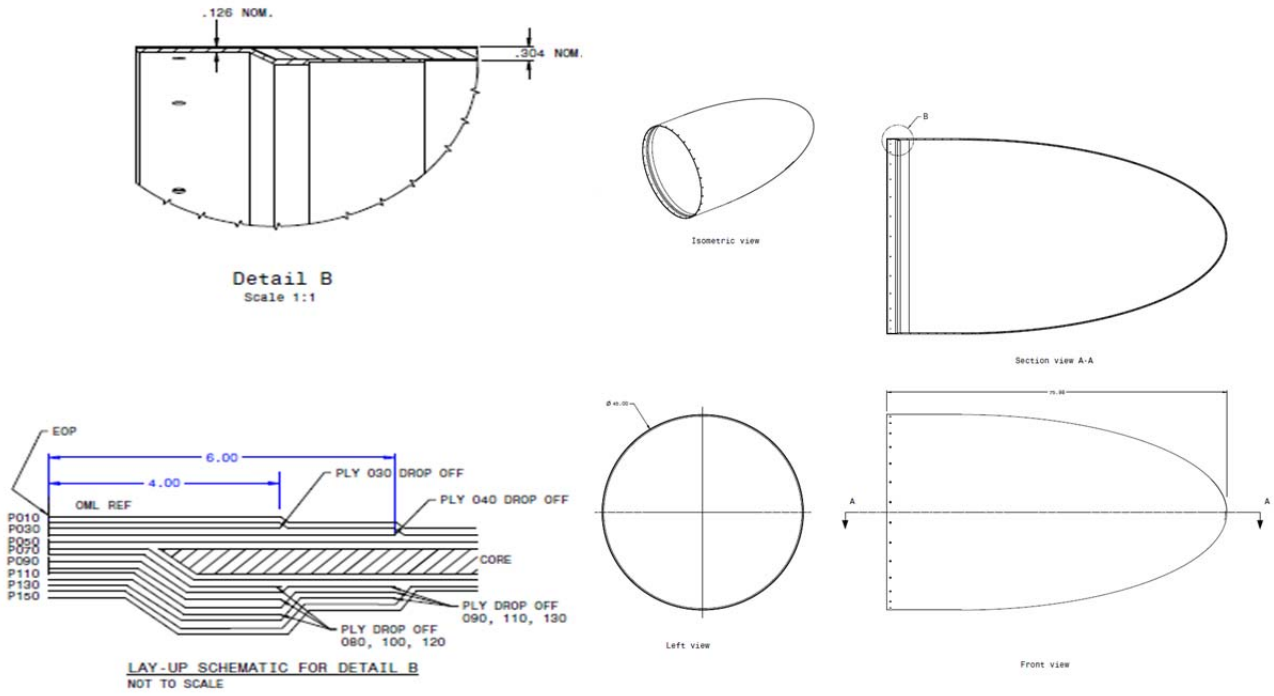

Figure 49 -C130 Sensor Pod Replica, Nose Section

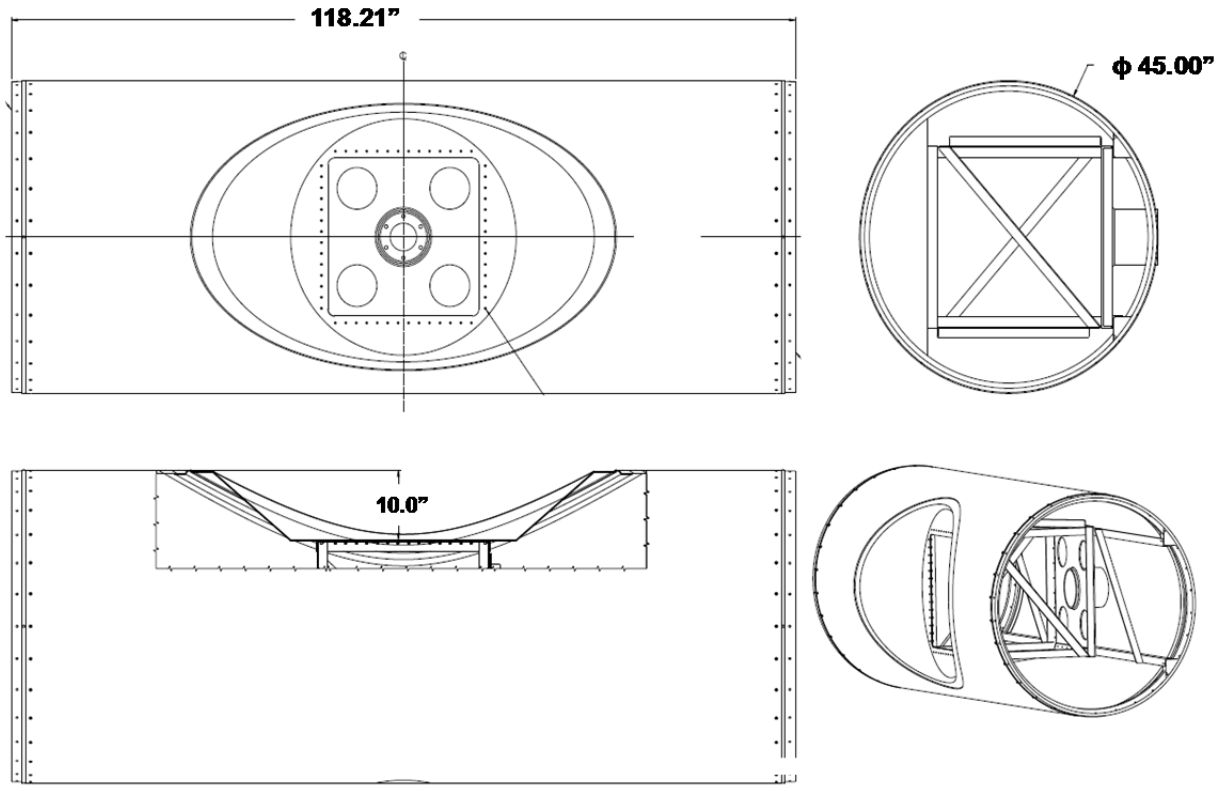

Figure 50 -C130 Sensor Pod Replica, Mid Section

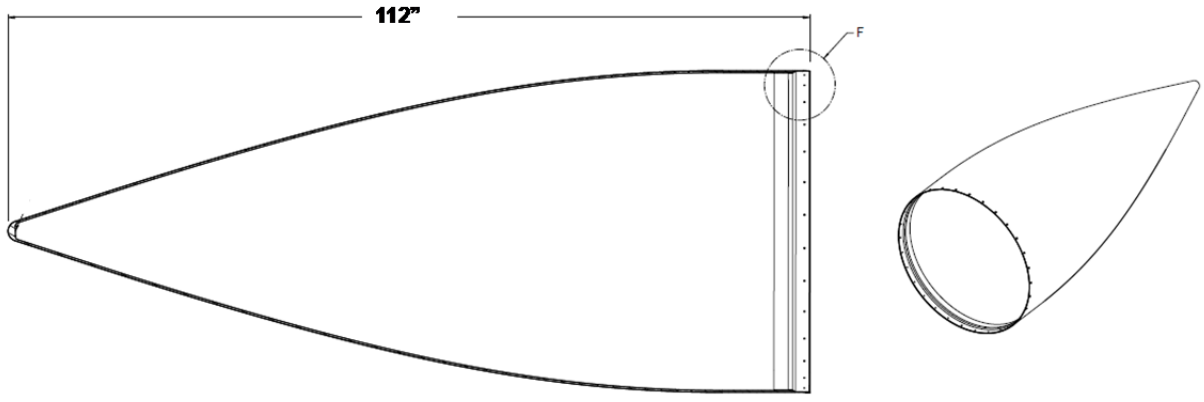

Figure 51 -C130 Sensor Pod Replica, Tail Section

Figure 52 -C130 Sensor Pod Replica, Fabrication Tooling

3.3.4 Structural Analysis

C-130 sensor pod replica has Graphite mid Section and E-Glass Nose and Tail Section. The structural analysis has been performed to ensure the deformation and safety under RF testing would not be affected. Fig. 53 shows the finite element structural model of C-130 sensor pod replica.

Fig. 54 depicts the stress level and deformation of C-130 sensor pod replica under loading condition during RF testing.

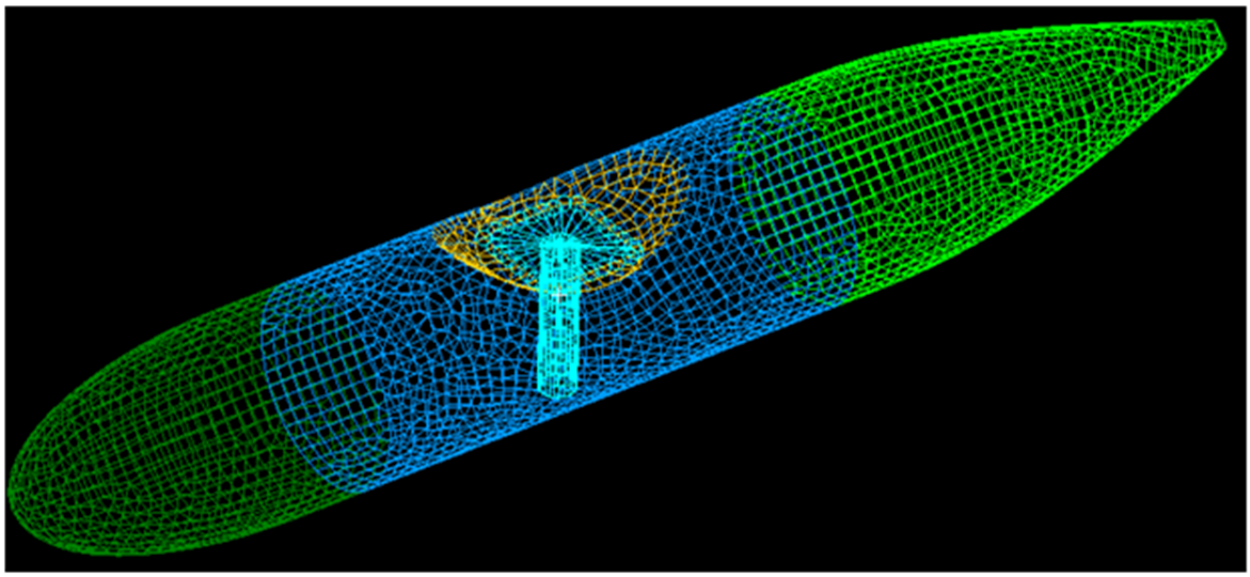

Figure 53 -C130 Sensor Pod Replica, Finite Element Structural

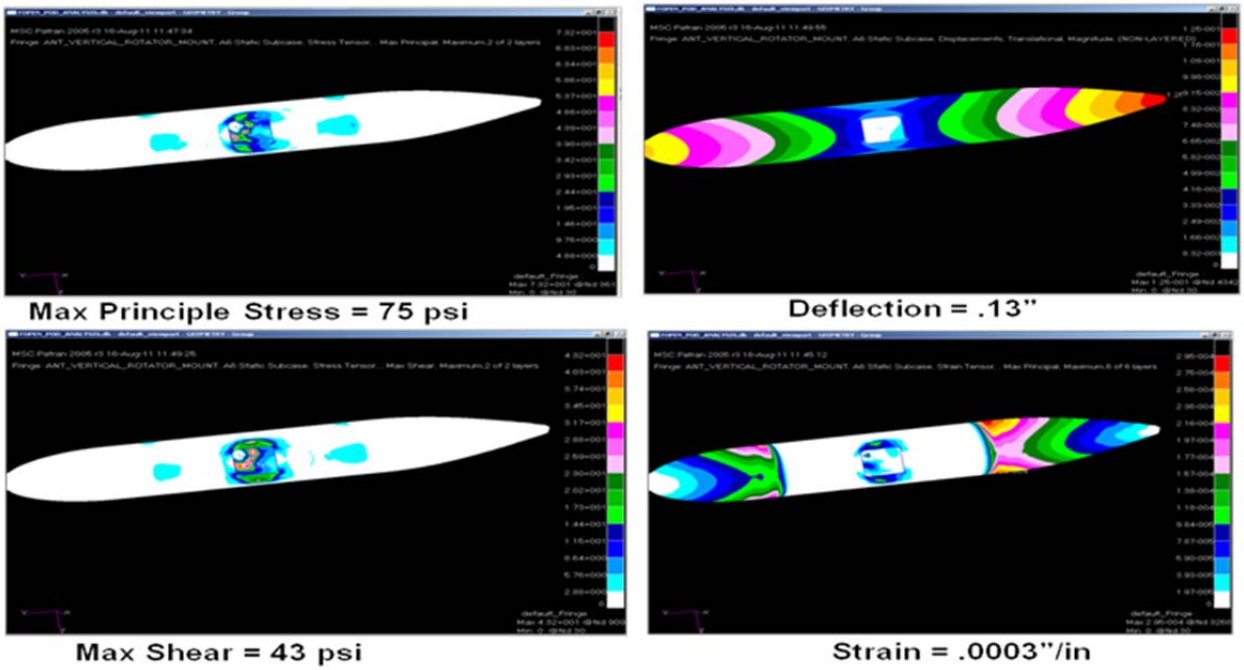

Figure 54 -C130 Sensor Pod Replica, Max Stress and Deformation

3.3.5 High Power Divider

FOPEN Meta-array needs two 1x32 sets of power distribution network/combiner for 1.0k watts peak and 12% duty cycle (120cw).

LM Aero adds on additional safety to ensure the success of high power test. The high power divider/combiner is designed to handling 1.5kw peak with 300Cw, pulse width-35µSec, prf-5kHz and 30% duty-cycle. Figure 55 shows the design of the custom built high power divider/combiner distribution network.

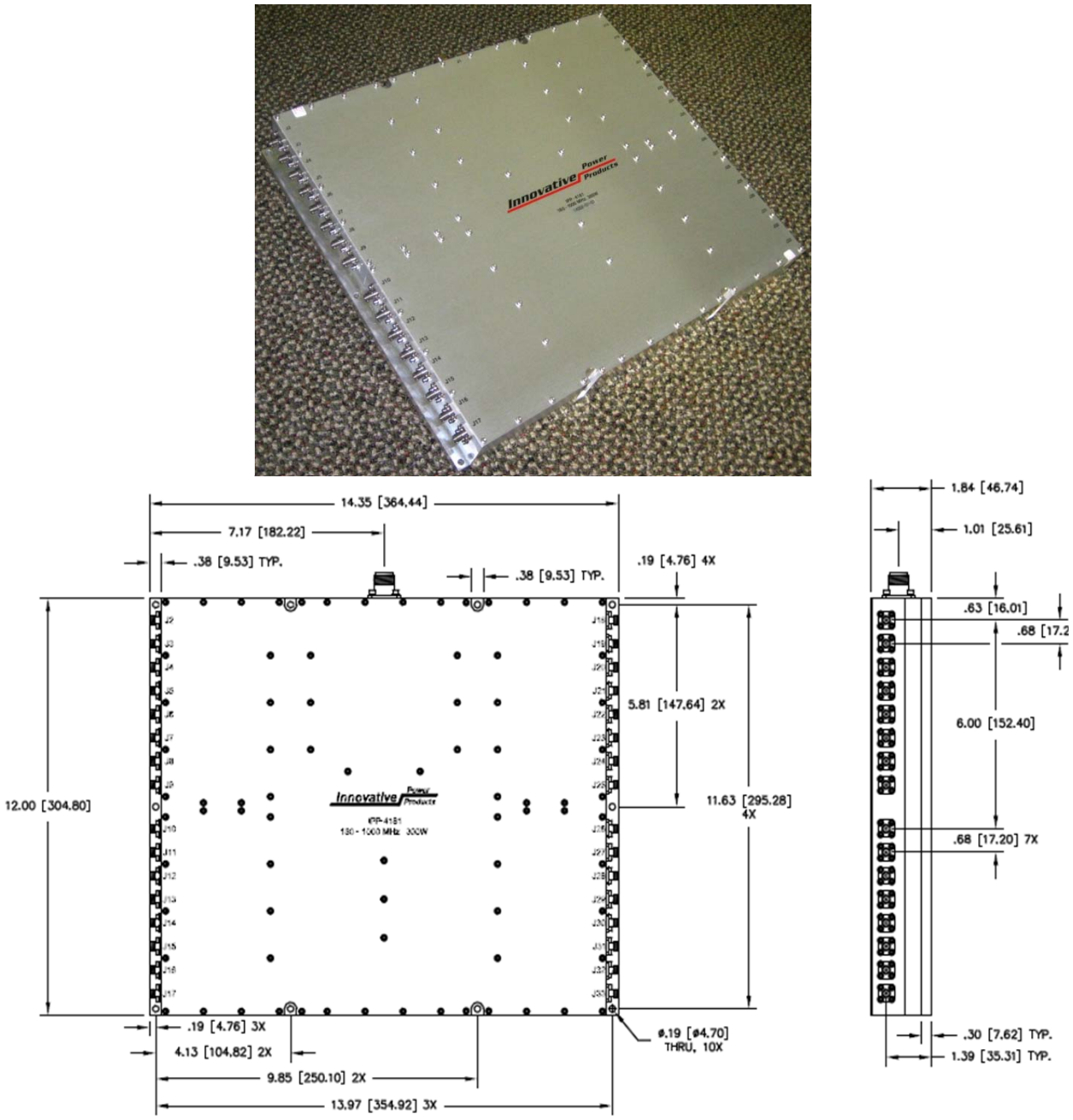

Figure 55 -High Power Divider/Combiner Design

3.3.6 Thermal Analysis

OSU has evaluated the thermal capability at the cross-over of 50-200 ohm balun feed lines. No power break down or excessive heating from RF power under the operating environment. Fig. 56 shows the estimated thermal result using a simplified thermal method.

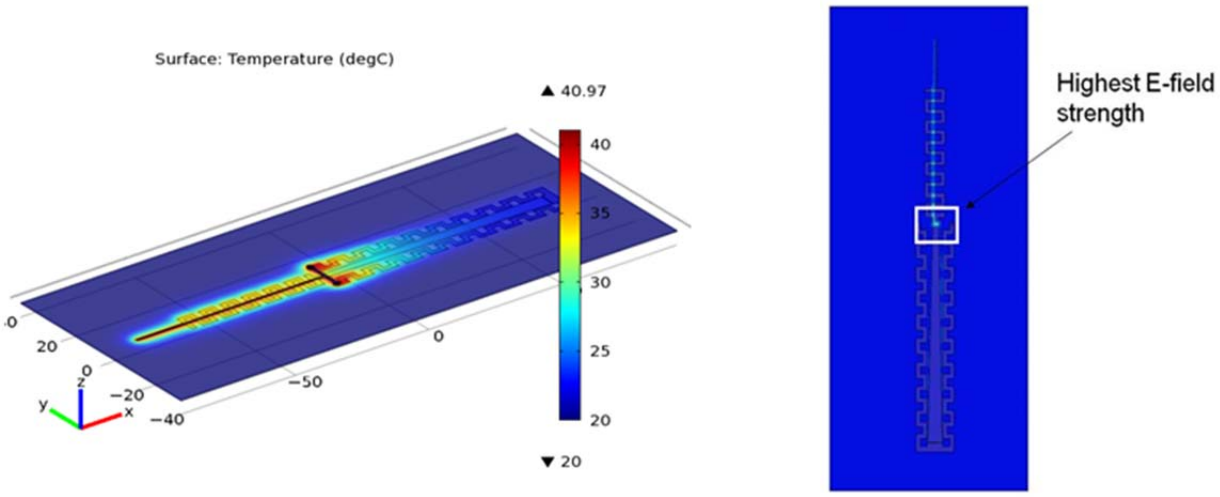

Figure 56 -Thermal Analysis, Transform/Balun Surface Temperature with 1 KW Input

Fig. 57 is the 8x8 dual-pol FOPEN meta-array thermal model taken into the account of all physical dimensions, dielectric material properties (dielectric constant, loss tangent and conductivity), metallic ground plane, manufacturing process, fabrication method, impedance transformer/balun, radiated electric/magnetic fields and excited mode shape in the environmental conditions. Fig. 58 shows the predicted temperature distribution. The resultant temperature indicates no power break down and degradation due to excessive heating under high power operation.

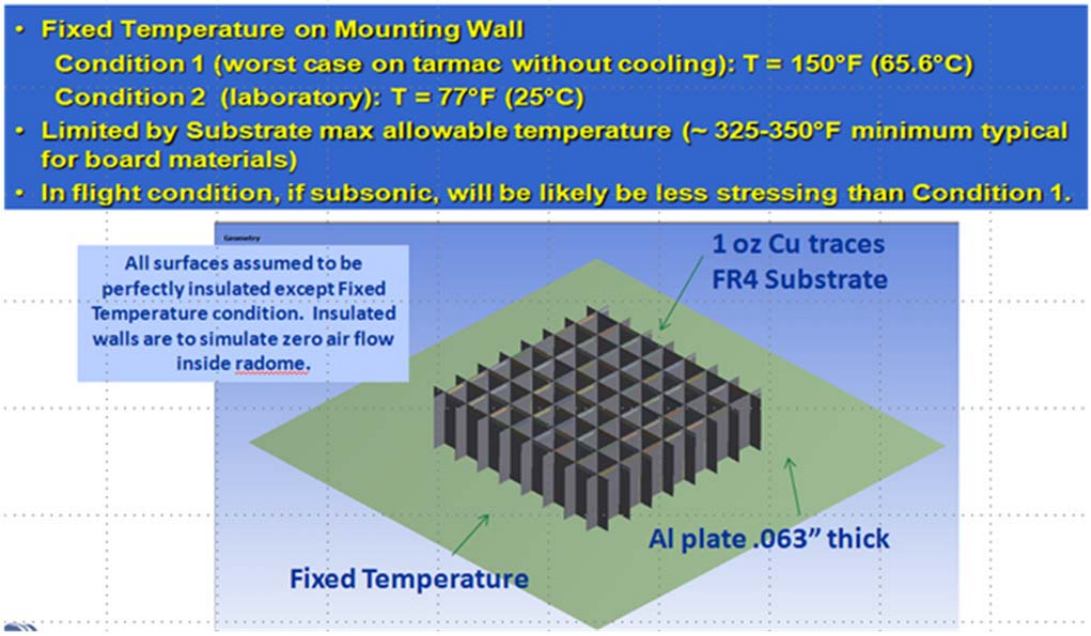

Figure 57 -Thermal Analysis, Thermal model

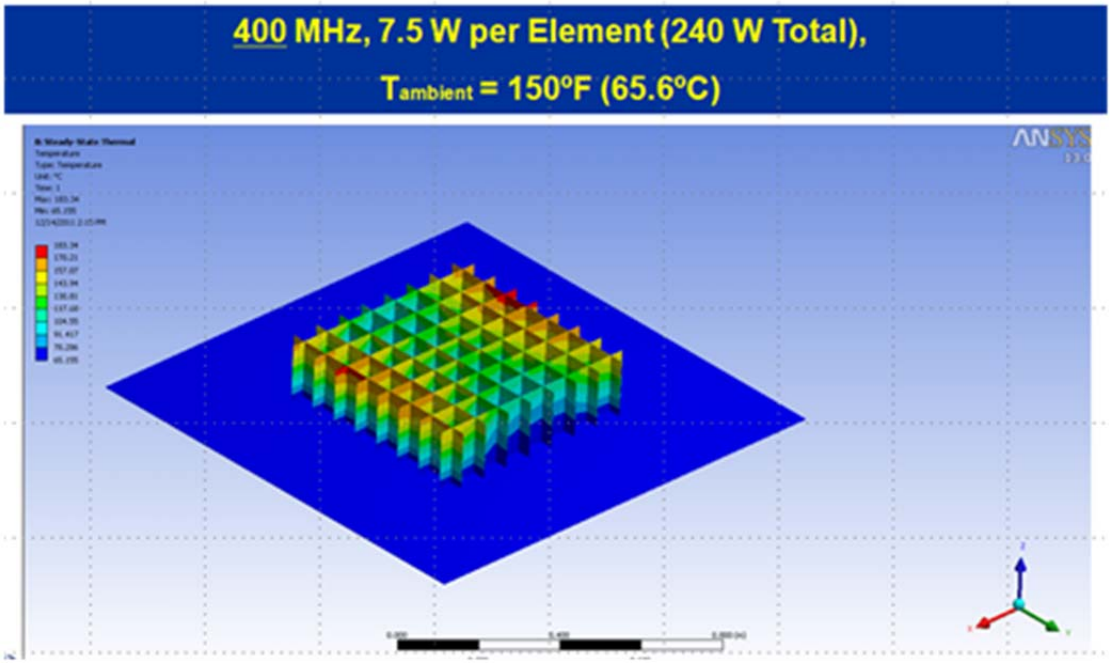

Figure 58 -Thermal Analysis, Predicted Temperature Distribution

3.3.7 High Power Testing

Prototype #4 (8x8 dual-pol) is connected to the high power divider/combiner, and tested inside an anechoic chamber. Prototype #4 is successfully passed 30 minutes in each power level of Table 3. No physical distortion, power break down or electrical malfunction at the completion of the high power test.

This high power test is conducted at CKC Laboratories, Fremont, Ca. Fig. 59 shows the high power test setup inside an anechoic chamber at CKC Laboratories.

Table 3 -High Power Test Level

Test	Pulse Width	PRF	Duty Cycle
A	6 uSec	3kHz	1.8%
B	35 uSec	3kHz	10.5%
C	6 uSec	5kHz	3%
D	35 uSec	5kHz	7.5%
E	12 uSec	3kHz	3.6%
F	70 uSec	3kHz	21%
G	12 uSec	5kHz	6%
H	70 uSec	5kHz	35%

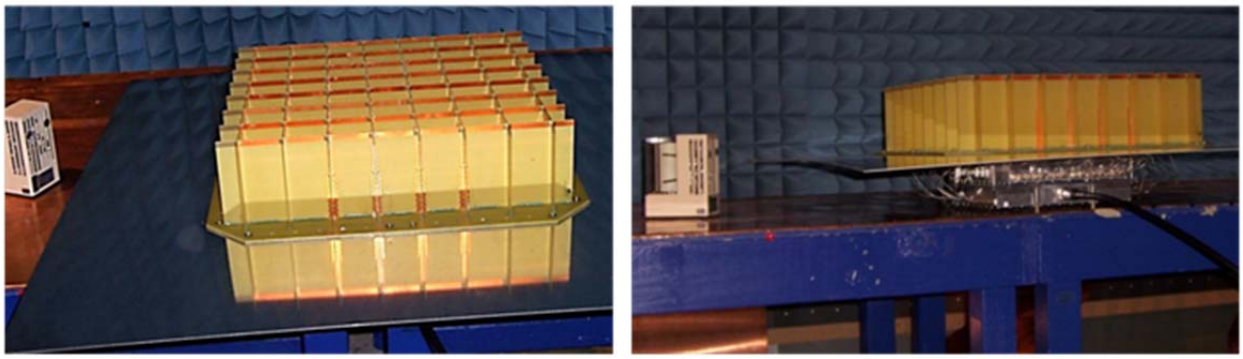

Figure 59 -FOPEN Meta-Array under High Power Testing at CKC Laboratories, Inc.

3.3.8 Integrated Assembly

Figure 60 shows the installation steps. The FOPEN meta-array is integrated onto the C-130 Shadow Harvest sensor pod replica at LMA, Palmdale, Ca, and then transported to Rye Canyon Measurement Facility for RF testing. Figure 61 shows the preparation of RF testing inside a Rye Canyon anechoic chamber.

Figure 60 -FOPEN Meta-Array Integrated Assembly

Figure 61 -Test Preparation

3.3.8.1 VSWR Measurement

The VSWR of each polarization is measured and summarized in Fig 62.

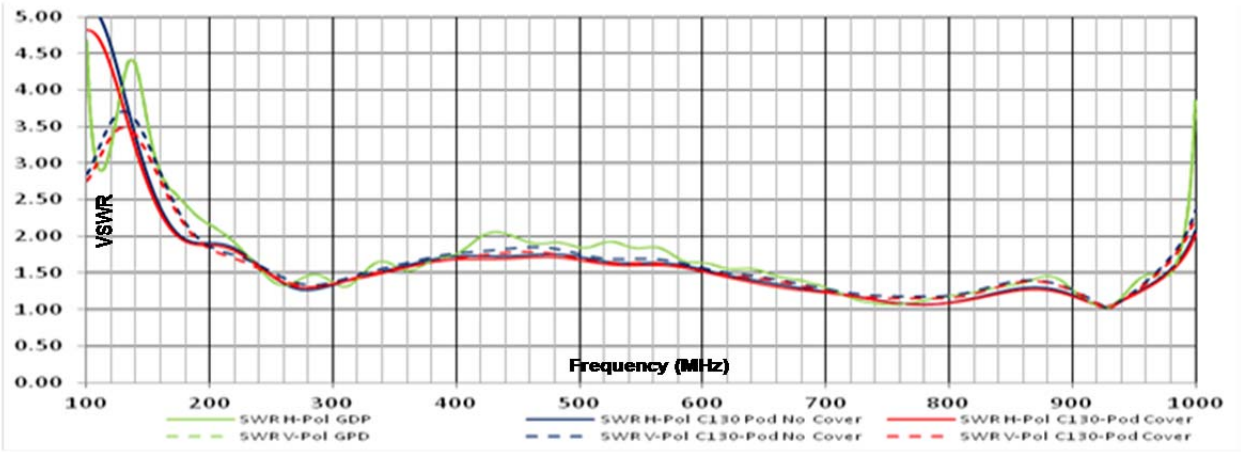

Figure 62 -Measured VSWR

The measured results are consistence to the prediction. Fig. 62 shows the VSWR results are almost on top of each other. This is a good indication to C-130 sensor pod replica is an excellent conductive body. The conical cavity and radome have minor effect to the impedance matching of integrated assembly. The FOPEN meta-array integrated assembly has ultra wide VSWR bandwidth approaching 5.5:1 (180-990MHz).

3.3.8.2 Pattern Measurement

Fig. 63 is the test setup and the coordinate system to the measured radiation patterns.

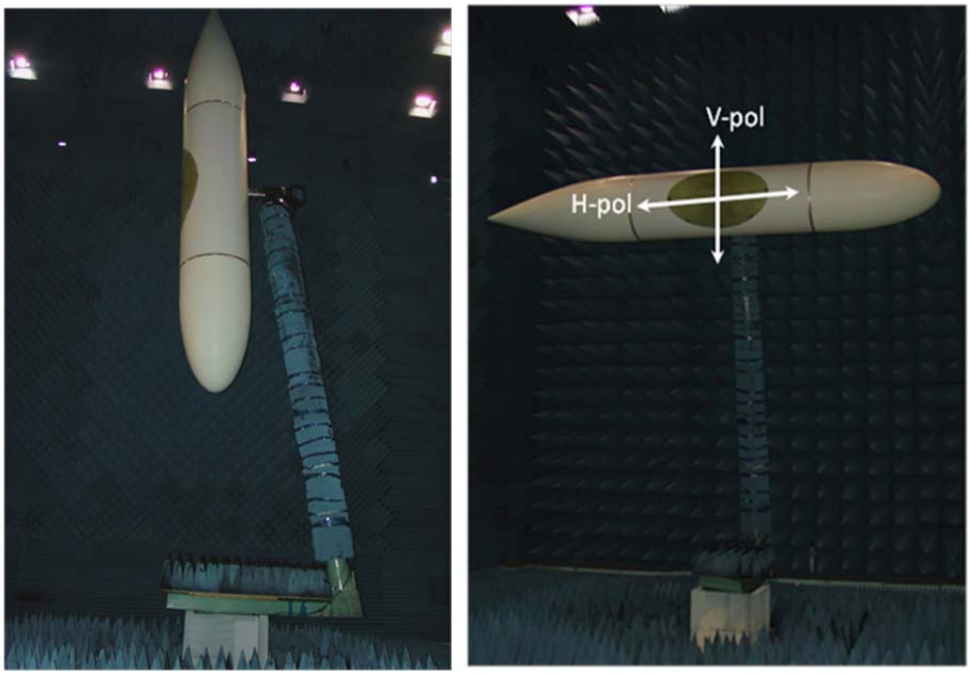

Figure 63 -FOPEN Meta-Array Integrated Assembly (Testing at Rye Canyon Measurement Facility)

The measured radiation patterns from 220-900MHz in each polarization are summarized in Fig. 64. The Peak gain shown in Fig 60 is extracted results from Fig. 65.

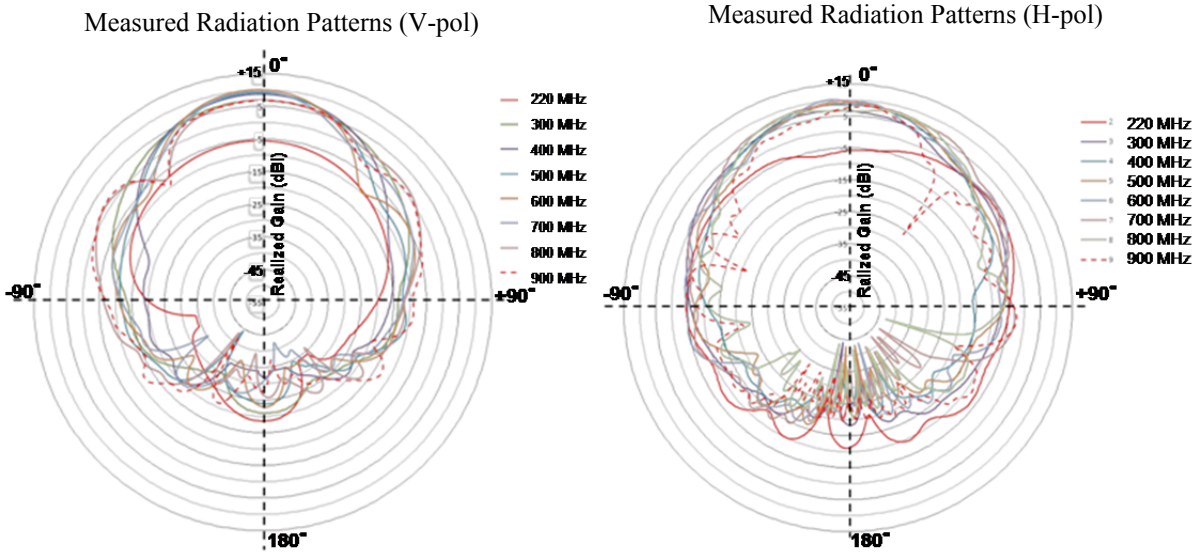

Figure 64 -Measured Radiation Patterns On C-130 Sensor Pod Replica

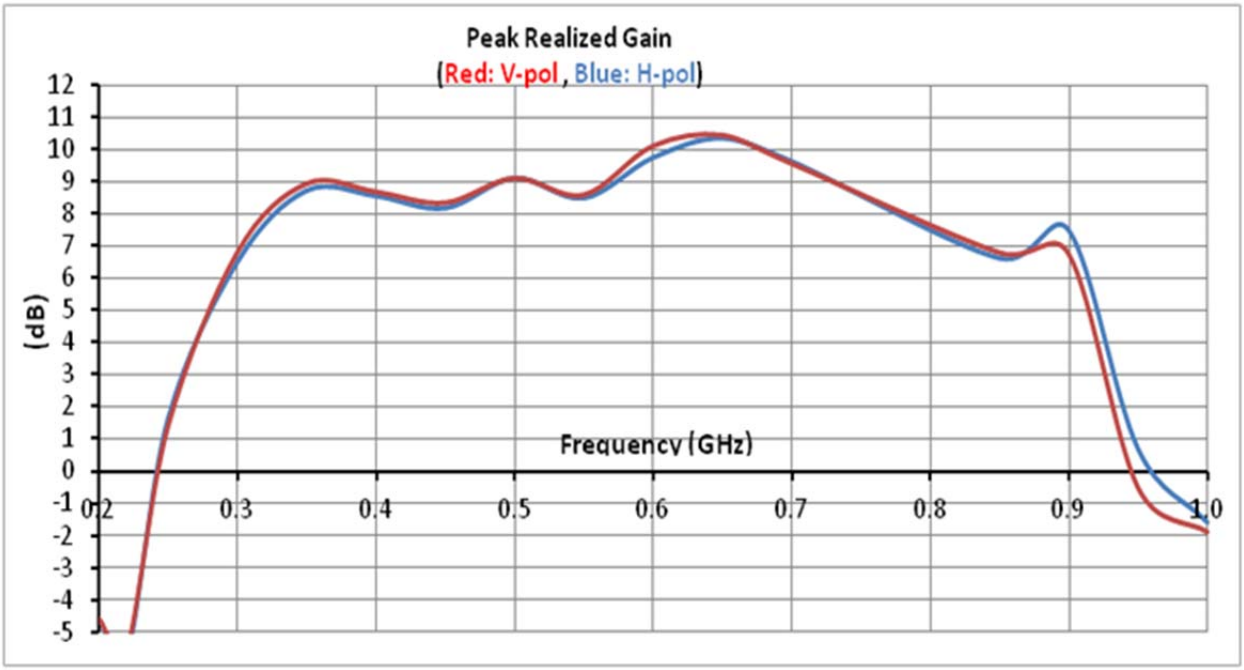

Figure 65 -Realized Peak Gain On C-130 Sensor Pod Replica

3.3.8.3 Beam Steering

Three different phase distributions have been applied to the FOPEN meta-array integrated assembly. It is accomplished by installing a coaxial cable set trimmed to a specified Δϕ phase distribution. LMA has purchased three (3) coaxial cable sets corresponding to 10° 20° or 30° Δϕ ± 0.25° phase distribution. The 20° and 30° cable sets are scaled from the 10° Δϕ phase distribution at 200MHz.

The beam steering measurement is conducted in four (4) separate runs. The first run has a uniform phase distribution, and the subsequent runs has increased phase distribution to create beam steering from 0° to 30° θ with 10° increments. At the completion of each pattern run, the old phase matched cable set is removed and replaced with a new phase matched for a different steering angle.

Fig. 66 is the measured radiation patterns for three different beam steering angles (10°, 20°and 30°) at 200MH. The measured beam scanning does not match with the theoretical prediction. Those cable sets suppose to produce 10°, 20°and 30° beam scanning, but instead of yielding beam scanning angle of 60°. We have made no attempt to optimize the phase Δϕ phase distribution to improve the measured results due to the cost and the schedule constrain. Further study is needed for a better understanding of predicting Δϕ phase distribution.

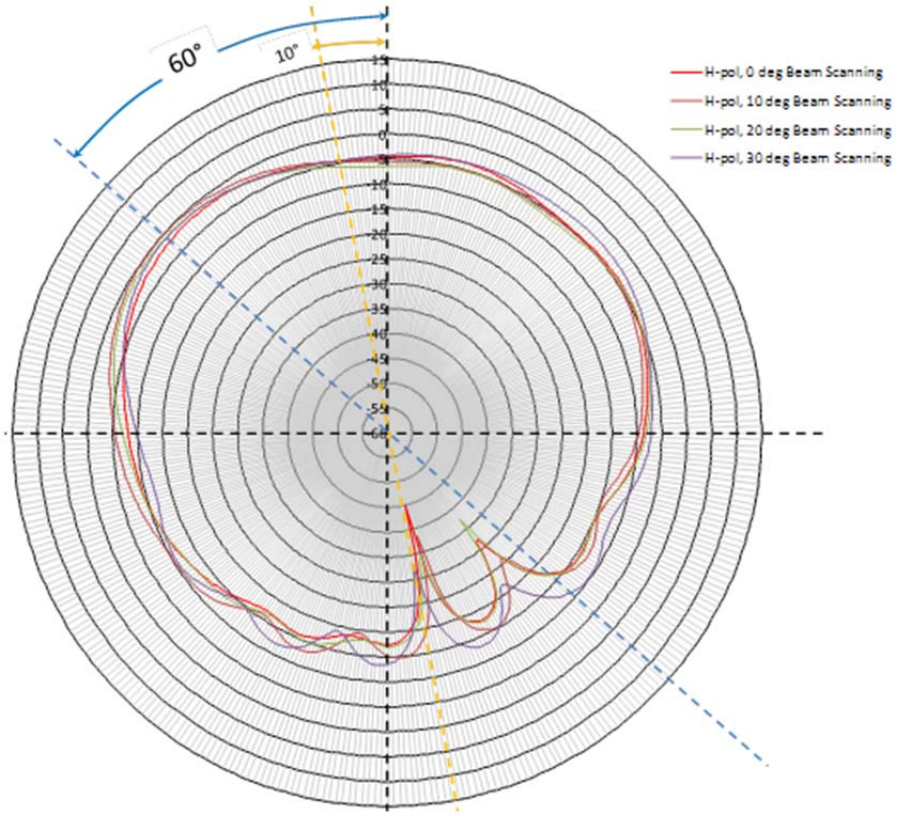

Figure 66 -H-pol, Radiation Patterns at 200 MHz

Fig. 67 is the measured active VSWR on the FOPEN meta-array with different phase matched cable sets for 10°, 20° and 30° θ beam steering. The results show very small active VSWR distortion over three θ beam steering angles.

Figs. 68, 69 and 70 are the measured radiation patterns from 220-900MHz with phase cable sets 10°, 20° and 30°, respectively.

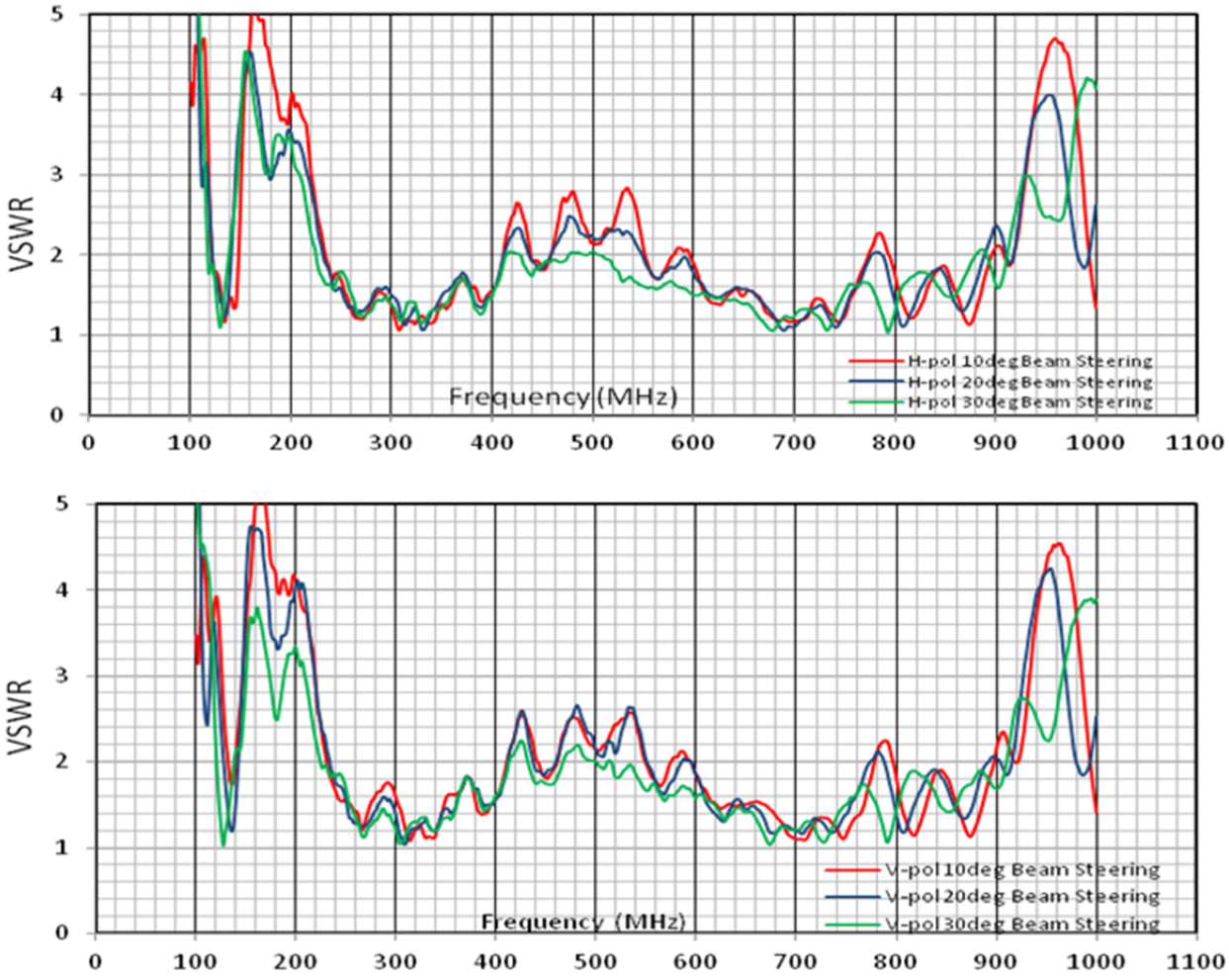

Figure 67 -Active VSWR at Three Different Scanning Angles (10º, 20º and 30º)

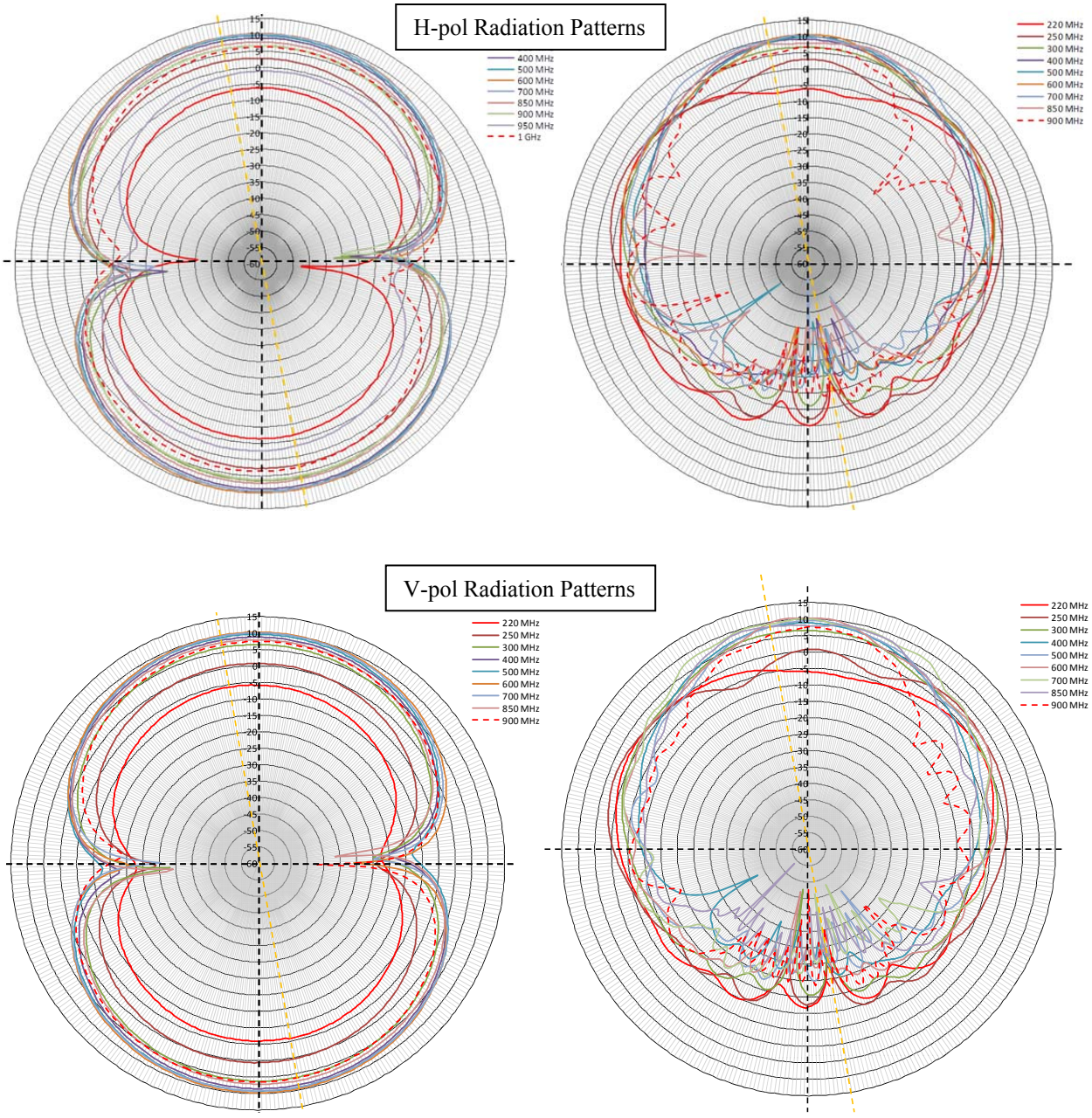

Figure 68 -Radiation Patterns at 10º Beam Steering

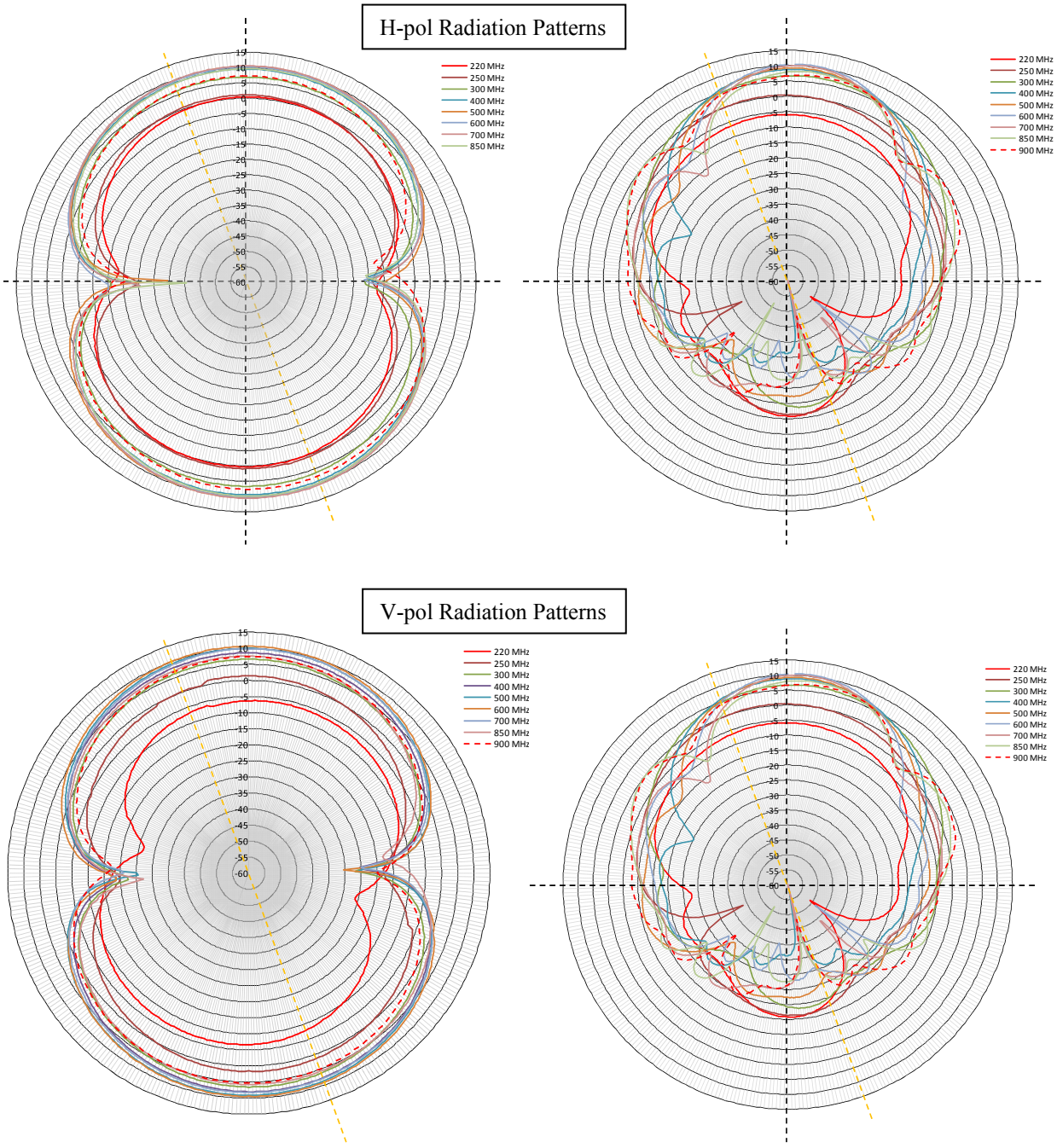

Figure 69 -Radiation Patterns at 20º Beam Steering

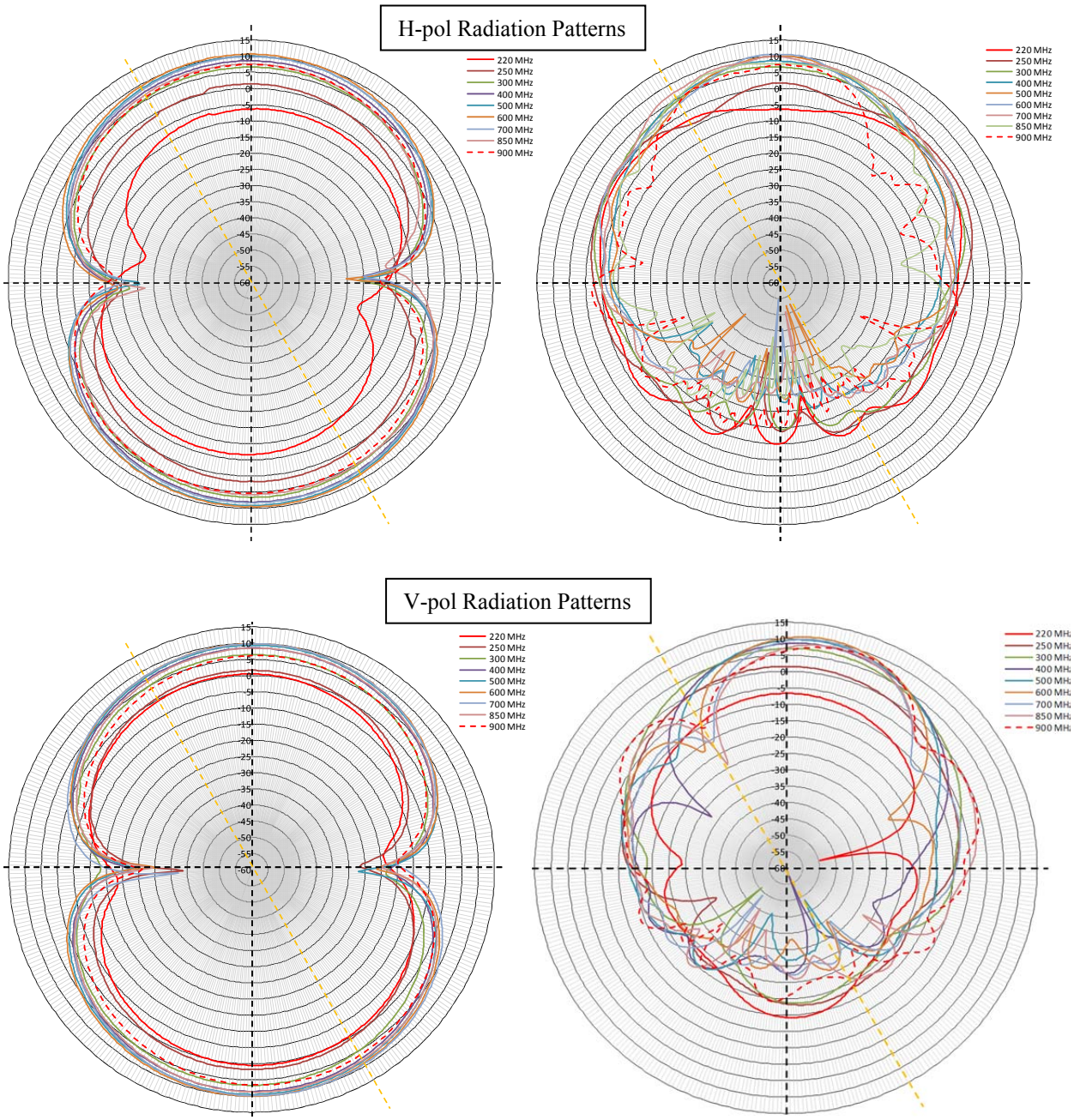

Figure 70 -Radiation Patterns at 30º Beam Steering

4. RESULTS AND DISCUSSION

In Phase I, AFRL Metamaterials RF, FOPEN Applications Program, LMA/OSU has developed a theoretical approach, analytical methods and simulation to design a metamaterial array (meta-array) for FOPEN application.

The predicted results show the FOPEN meta-array has UWB (220-900MHz), 80-92% radiating efficiency, 24”x24”x6”(height) aperture size and weights 5.6 lbs. The proposed meta-array to Phase II (prototype development) can enhance or enable antenna performance beyond current SOA, and is larger than 2x miniature factors of SOA Aperture.

LMCSS has developed the current and future FOPEN system requirements by extracting the knowledge learned from LM TRACER program.

The predicted results indicate the meta-array will meet the current and future FOPEN system requirements.

In Phase II, LMA/OSU team has performed studies to optimize meta-array configurations. Consequently, LMA/OSU team has fabricated and tested four laboratory-scale prototypes to verify the prediction.

The measured results are presented and summarized in Paragraphs 3.2.2.1.1 to 3.2.3.1.3. The 8x8 dual-pol FOPEN meta-array is performing beyond the current SOA antenna, and exceeding the current and future FOPEN system requirements.

In Phase III, LMA has integrated the Phase II develop 8x8 dual-pol prototype onto C-130 Shadow Harvest sensor pod replica successfully. The active VSWR, radiation patterns, and beam steering are measured on the FOPEN meta-array integrated assembly. The measured results are summarized and presented in Paragraphs 3.3.8.1 to 3.3.8.3.

The measured active VSWR shows meta-array has UWB (180-1000MHz) performance. The measured radiation patterns show realized gains in between 5-12 dBi over the frequency band 250-900MHz. The measured beam steering angles show the FOPEN meta-array integrated system has wide angle beam steering greater than 60º and minor impact to active VSWR.

5. CONCLUSIONS

LMA/OSU team has successfully completed the objectives, budget and schedule of Phase I, Phase II and Phase III of AFRL FOPEN for RF Metamaterial, FOPEN Application program.

The predicted and measured results have demonstrated the developed FOPEN meta-array integrated assembly is a class of metamaterial antenna technology which will offer equivalent pattern (gain, beam width, sidelobes, cross-polarization), VSWR bandwidth and beam steering to a SOA with 2x reduction in aperture size.

6. REFERENCES

STATEMENT OF WORK

1. Air Force Research Laboratory — FOR BAA-09-01-PKS STROEB II Call 2 Metamaterials for RF Applications Wright-Patterson AFB, OH 45433-7801, ADP NT 09-0625, May 2009
2. LM Commercial Space Systems — FOR BAA-09-01-PKS STROEB II Call 2 Metamaterials for RF Applications, April 2009
3. Ohio State University — In Support of BAA-09-01-PKS STROEB II Call 2 Metamaterials for RF Applications, April 2009

APPENDIX – PUBLICATIONS AND PRESENTATION

[1] R. Porath, "Theory of Miniaturized Shorting-Post Microstrip Antennas," IEEE Transactions on Antennas and Propagation, vol. 48, No. 1, pp. 41 – 47, Jan. 2000.

[2] J. H. Lu, and K. L. Wong, "Slot-Loaded Meandered Rectangular Microstrip Antenna with Compact Dual Frequency Operation," Electronics Letters, vol. 34, pp 1048 – 1050, May 1998.

[3] D. H. Schaubert, D. M. Pozar, and A. Adrian, "Effect of Microstrip Antenna Substrate Thickness and Permittivity," IEEE Transactions on Antennas and Propagation, vol. 37, no. 6, pp. 677 – 682, Jun. 1989.

[4] IEEE Transactions on Antennas and Propagation, Special Issue on Metamaterials, vol. 51, 2003.

[5] D.Polder, "On the theory of ferromagnetic resonance." Phil.Mag. 40:99–115, January 1949.

[6] G. Tyras, "The permeability matrix for a ferrite medium magnetized at an arbitrary direction and its eigenvalues," IRE Transactions on Microwave Theory and Techniques, vol. 7, no. 1, pp. 176–177, January 1959.

[7] H. Gundel, H. Riege, E.J.N. Wilson, J. Handerek, and K. Zioutas, "Fast polarization changes in ferroelectrics and their application in accelerators," Nucl. Instrum. Methods Phys. Res. A, vol. 280, pp. 1–6, 1989.

[8] X. Zuo, H. How, S. A. Oliver, and C. Vittoria, "Development of high frequency ferrite phase-shifter," IEEE Transactions on Magnetics, vol. 37, no. 4, pp. 2395–2397, July 2001.

[9] R. A. Shelby, D. R. Smith, and S. Schultz, "Experimental verification of a negative index of refraction", Science, vol. 292, pp. 77–79, 2001.

[10] J. B. Pendry, A. J. Holden, D. J. Robbins, and W. J. Stewart, "Magnetism from conductors and enhanced nonlinear phenomena", IEEE Transactions on Microwave Theory and Techniques, vol. 47, no. 11, pp. 2075 – 2084, 1999.

[11] A. Grbic and G. V. Eleftheriades, "Overcoming the diffraction limit with a planar left handed transmission line lens," Physical Review Letters, vol. 92, no. 11, pp. 117403 1 – 117403 4, Mar. 2004.

[12] M. A. Antoniades and G. V. Eleftheriades, "Compact linear lead/lag metamaterial phase shifters for broadband applications," IEEE Antennas and Wireless Propagation Letters., vol. 2, no. 7, pp. 103–106, Jul. 2003.

[13] G. V. Eleftheriades and K. G. Balmain, Negative–Refraction Metamaterial. New York, USA: IEEE Press - John Wiley & Sons, 2005.

[14] C. Caloz and T. Itoh, Electromagnetic Metamaterials: Transmission Line Theory and Microwave Applications, Wiley-IEEE Press, 2005.

[15] E. Yablonovich. "Inhibited spontaneous emission in solid-state physics and electronics," Physical Review Letters, 58:2059, 1987.

[16] J. Joannopoulos, R. Meade, and J. Winn, Photonic Crystals – Molding the Flow of Light, Princeton, NJ: Princeton Univ. Press, 1995.

[17] B. Temelkuran, M. Bayindir, E. Ozbay, R. Biswas, M. M. Sigalas, G. Tuttle, and K. M. Ho, "Photonic crystal based resonant antenna with a very high directivity," Journal of Applied Physics, vol. 87, no. 1, pp.603–605, Jan. 2000.

[18] R. Biswas, E. Ozbay, B. Temelkuran, M. Bayindir, M. M. Sigalas, and K. M. Ho. "Exceptionally directional sources with photonic–bandgap crystals," Journal of the Optical Society of America B, 18(11):1684–1689, November 2001.

[19] R. F. J. Broas, D. F. Sievenpiper, and E. Yablonovitch, "A high-impedance ground plane applied to a cellphone handset geometry," IEEE Transactions on Microwave Theory and Techniques, vol. 49, no. 7, pp. 1262–1265, July 2001.

[20] F. Yang and Y. Rahmat-Samii, "A low profile circularly polarized curl antenna over an electromagnetic bandgap (EBG) surface," Microwave and Optical Technology Letters, vol. 31, no. 4, pp. 264 – 267, Nov. 2001.

[21] R. W. Ziolkowski and A. D. Kipple, "Application of double negative materials to increase the power radiated by electrically small antennas," IEEE Transactions on Antennas and Propagation, vol. 51, no. 10, pp. 2626–2640, October 2003.

[22] A. Erentok, P. L. Luljak, and R. W. Ziolkowski, "Characterization of a volumetric metamaterial realization of an artificial magnetic conductor for antenna applications," IEEE Transactions on Antennas and Propagation, vol. 53, no. 1, pp. 160–172, January 2005.

[23] G. Kiziltas, D. Psychoudakis, J. L. Volakis, and N. Kikuchi, "Topology design optimization of dielectric substrates for bandwidth improvement of a patch antenna," IEEE Transactions on Antennas and Propagation., vol. 51, no. 10, pp. 2732–2743, Oct. 2003.

[24] D. Psychoudakis, J. L. Volakis, Z. N. Wing, S. K. Pillai and J. H. Halloran, "Enhancing UHF Antenna Functionality through Dielectric Inclusions and Texturization," IEEE Transactions on Antennas and Propagation, vol.54, no.2, pp. 317- 329, Feb. 2006

[25] R. Ziolkowski and A. Erentok, "Metamaterial-Based Efficient Electrically Small Antennas," IEEE Transactions on Antennas and Propagation, vol. 54, no. 7, pp. 2113 – 2129, July 2006.

[26] A. Sanada, M. Kimura, I. Awai, C. Caloz, T. Itoh, "A Planar Zeroth-Order Resonator Antenna Using a Left-Handed Transmission Line," 34th European Microwave Conference - Amsterdam, 2004.

[27] K. M. K. H. Leong, C-J. Lee, and T. Itoh, "Compact Metamaterial Based Antennas for MIMO Applications," International Workshop on Antenna Technology (IWAT), pp. 87 – 90, March 2007.

[28] F. Qureshi, M. A. Antoniades, and G. V. Eleftheriades, "A Compact and Low-Profile Metamaterial Ring Antenna with Vertical Polarization," IEEE Antennas and Wireless Propagation Letters, vol. 4, 2005.

[29] G. Mumcu, K. Sertel, and J. L. Volakis, "Miniature Antennas and Arrays Embedded within Magnetic Photonic Crystals," IEEE Antennas and Wireless Propagation Letters, vol. 5, no. 1, pp. 168 – 171, Dec. 2006.

[30] G. Mumcu, K. Sertel, J.L. Volakis, I. Vitebskiy, and A. Figotin, "RF Propagation in Finite Thickness Unidirectional Magnetic Photonic Crystals," IEEE Antennas and Propagation Trans., Vol. 53, no. 12, pp. 4026-4034, Dec. 2005.

[31] S. Yarga, K. Sertel, and J. L. Volakis, "Degenerate Band Edge crystals for Directive Antennas," IEEE Trans. on Antennas and Propag, vol. 56, pp. 119-126, Jan 2008.

[32] A. Figotin and I. Vitebsky, "Gigantic transmission band-edge resonance in periodic stacks of anisotropic layers," Physical Review E, 72-036619, pp. 1–12, Sep. 2005.

[33] A. Figotin and I. Vitebsky, "Nonreciprocal magnetic photonic crystals," Physical Review E, 63:066609, pp. 1–20, May 2001.

[34] A. Figotin and I. Vitebsky, "Electromagnetic unidirectionality in magnetic photonic crystals," Physical Review B, 67:165210, pp. 1–20, April 2003.

[35] M. B. Stephanson, K. Sertel and J. L. Volakis, "Frozen modes in Coupled Microstrip Lines Printed on Ferromagnetic Substrates", IEEE Microwave Wireless Compon.Lett., vol. 18, pp. 305-307, May 2008.

[36] C. Locker, K. Sertel, and J. L. Volakis, "Emulation of Propagation in Layered Anisotropic Media with Equivalent Coupled Microstrip Lines," IEEE Microwave Wireless Compon.Lett., vol. 16, no.12, pp.642-644, pp. 305-307, Dec. 2006.

[37] G. Mumcu, K. Sertel, and J. L. Volakis, "Miniature Antenna Using Printed Coupled Lines Emulating Degenerate Band Edge Crystals," IEEE Transactions on Antennas and Propagation, vol. 57, no. 6, pp. 1618 – 1624, June 2009.

[38] H.A. Wheeler, "The radiation resistance of an antenna in an infinite array or waveguide," Proc. IRE, vol. 36, pp. 478-488, April 1948.

[39] H. A. Wheeler, "Simple Relations Derived from a Phased-Array Antenna Made of an Infinite Current Sheet," IEEE Trans. Antennas and Prop. Vol. 13, pp. 506-514, July 1965.

[40] Munk, B. A.: 'Finite Antenna Arrays and FSS', IEEE Press/Wiley-Interscience, 2003, ch. 6, pp. 181–213.

[41] Simons, R.N., Dib, N.I., Katehi, L.P.B., "Coplanar Stripline to Microstrip Transition," IET Electronics Letters, Vol. 31, Issue 20, pp. 1725-1726, September 1995.

[42] Balanis, C.A., Antenna Theory: Analysis and Design, 2nd Edition, Wiley & Sons.

[43] Harrington, R.F., Mautz, J.R., "Theory of Characteristic Modes for Conduction Bodies," IEEE Trans. Antennas and Prop. Vol. 19, no. 5, pp. 622-628, September 1971.

[44] Paraschos, G.N., Kindt, R., Schaubert, D.H., Vouvakis, M.N., "Radiation and coupling studies of finite-size dual polarized vivaldi arrays using a domain decomposition FEM,", APS 2008